2018

Geochronologic Constraints On The Timing Of Metamorphism And Exhumation Of The Tillotson Peak Complex In Northern Vermont

Cheyne Aiken
University of Vermont

GEOCHRONOLOGIC CONSTRAINTS ON THE TIMING OF METAMORPHISM AND EXHUMATION OF THE TILLOTSON PEAK COMPLEX IN NORTHERN VERMONT

A Thesis Presented

by

Cheyne L. Aiken

to

The Faculty of the Graduate College

of

The University of Vermont

In Partial Fulfillment of the Requirements
for the Degree of Master of Science
Specializing in Geology

October, 2018

Defense Date: June 19, 2018
Thesis Examination Committee:

Laura E. Webb, Ph.D., Advisor
Donald S. Ross, Ph.D., Chairperson
Keith Klepeis, Ph.D.
Cynthia J. Forehand, Ph.D, Dean of the Graduate College

ABSTRACT

The Tillotson Peak Complex (TPC) in northern Vermont records high-pressure (HP) subduction zone metamorphism that occurred during the Ordovician Taconic Orogeny, and subsequent retrograde metamorphism and deformation that occurred during the Silurian Salinic Orogeny. Previous studies have documented a polymetamorphic history, with peak metamorphic pressures possibly up to 2.5 GPa and temperatures of 550°C. Prior to this research, constraints on the timing of metamorphism in the TPC were limited to a single Middle Ordovician $^{40}Ar/^{39}Ar$ total fusion age for glaucophane. This study integrates $^{40}Ar/^{39}Ar$ step heating analyses of multiple mineral phases and U-Pb dating of titanite with field and microstructural observations to further constrain the subduction–exhumation history of the TPC.

Microstructural and petrologic analyses in thin section on samples of felsic gneiss, pelitic schist, amphibolite, and blueschist suggest deformation during varied P-T conditions. The earliest and highest-pressure metamorphic event documented in the TPC samples is associated with inclusions in garnet and white mica in S_1 quartz microlithons. Inclusions of paragonite, titanite, and omphacite in garnets, locally defining S_1, suggest that some blueschist may have formed in the retrograde path in association with the S_2 foliation. A greenschist-facies metamorphic overprint in most samples is also associated with S_2, primarily defined by epidote, white mica, and chlorite. E-W trending F_2 intrafolial folds are commonly rootless in outcrop, locally defined by blueschist–eclogite-facies fold noses. Kinematic indicators relative to S_2 and L_2 stretching lineations give a predominantly top-to-the-E shear sense. S_3 crenulation cleavage development is related to folding about E-W trending F_3 folds that define the map pattern of the Tillotson Peak Complex. Locally developed S_4 crenulations are axial planar to the NW-trending Gilmore Antiform. Additionally, D_4 deformation and metamorphism is recorded by microfractures in garnet and epidote, as well as chlorite pseudomorphs after garnet.

$^{40}Ar/^{39}Ar$ step heating of multiple phases and U-Pb dating of titanite yielded ages corresponding with the Taconian to the Salinic orogenies. Ages of ~485–480 Ma are attributed to prograde–peak metamorphism (M_1) and S_1 development. Ages that span ~471–456 Ma are interpreted to document retrograde M_2 metamorphism through greenschist to locally blueschist-facies metamorphic conditions during exhumation and S_2 development. Correlation of D_3 microstructures in these samples with map-scale folds suggest that E–W trending folds developed in the range of ~455–445 Ma, recorded by minimum apparent ages in the field area, and locally as plateau ages along the margin of the TPC. Younger ages ~435–405 Ma are observed locally in apparent age gradients, and are interpreted to reflect metamorphic overprinting that resulted in the chlorite pseudomorphs after garnet and the growth of actinolite, which may be related to the timing of folding about the Gilmore Antiform. Results presented here suggest the impact of Acadian retrograde metamorphism and deformation on rocks of the TPC may be less significant than previous work suggests.

ACKNOWLEDGEMENTS

The work presented in this paper would not have been possible without the guidance, support, and knowledge of many individuals that have been a critical aspect in all stages of this research. Most importantly, Laura Webb, you have been more than understanding and offered more constructive criticism than I could have ever asked for. I cannot thank you enough for your patience when deadlines were approaching, as well as the advice you always had to offer. Additionally, I would like to thank my committee members, Don Ross and Keith Klepeis, for their feedback throughout this long process. Dan Jones without your knowledge and assistance in the lab, this research would have not been possible. I would like to thank Dr. Andrew Kylander-Clark for his willingness to examine titanite from our samples as a part of a pilot study. Jody Smith your availability and wisdom when it came to utilize the SEM was a great benefit to this research. Finally, this research would not have been possible were it not for financial support from the Burlington Gem and Mineral Club and the Vermont Geological Society to fund analyses, and the Ronald Suiter Prize from the University of Vermont to fund travel for presenting at conferences.

To Jon Kim, Joe Gonzalez, Susanne Baldwin, Evan Tam, Hannah Blatchford, John Mark Brigham, Beth Pidgeon, and anyone else that came out during field season: your input helped to formulate the interpretations established in this research. For that, I thank all of you. To my fellow graduate students, my friends, and coworkers: you made my time here memorable. Whether it be a quick hike, input on research, grabbing a beer together, or taking the time to listen to my complaints, you have my sincerest appreciation.

TABLE OF CONTENTS

ACKNOWLEDGEMENTS ..... **ii**
LIST OF FIGURES ..... **vi**
LIST OF TABLES ..... **vii**
CHAPTER 1: COMPREHENSIVE LITERATURE REVIEW **1**

1.1 Introduction 1
1.2 The Formation and Exhumation of High- to Ultrahigh-Pressure rocks 3
1.2.1 Introduction: 3
1.2.2 Formation of High-Pressure to Ultrahigh-Pressure Terranes: 4
1.2.3 Exhumation Mechanisms: 5
1.2.4 Geochronology: 10
1.2.5 Understanding Deformation Mechanisms with Microstructures 12

1.3 Geologic Setting of the Tillotson Peak Complex 14
1.3.1 Regional Geology 14
1.3.2 Tectonic Model for the Taconic Orogeny 15
1.3.3 Tectonic model for the Salinic Orogeny 17
1.3.4 Tectonic model for the Acadian Orogeny 18
1.3.5 Geology of the TPC 19
1.3.6 Geology of the Belvidere Mountain Complex and ophiolites in Quebec 22
1.3.7 Structural Geology 23

1.4 Geochronologic Constraints for Metamorphism in northern Vermont and southern Quebec 25
1.4.1 Metamorphism During the Early Taconic Orogeny 26
1.4.2 Metamorphism During the Late Taconic Orogeny 26
1.4.3 Metamorphism during the Salinic Orogeny 27
1.4.4 Acadian Overprinting on the rocks of the Northern Appalachians 28
1.4.5 Recent Studies in the TPC 29

CHAPTER 2: METHODS **50**

2.1 Introduction 50

2.2 Microstructural Analysis: 50
2.3 Compositional Analysis of K-rich and High-Pressure Phases 51
2.4 $^{40}Ar/^{39}Ar$ Dating of Actinolite, Glaucophane, Tourmaline, and White Mica 52
2.5 U-Pb Geochronology 54

CHAPTER 3: RESULTS 55

3.1 Introduction 55
3.2 16TP03A 56
3.3 16TP04B 58
3.4 16TP05BA 59
3.5 16TP05D 60
3.6 16TP08B 61
3.7 16TP15A/B 63
3.8 16TP15D 64
3.9 16TP16A 65
3.10 16TP17B 66
3.11 16TP19A 67
3.12 16TP21A 68
3.13 16TP22A 69
3.14 16TP24A/B 70
3.15 16TP26A 71
3.16 16TP27A 72
3.17 Kinematic Indicators in Additional Samples 72

CHAPTER 4: DISCUSSION 94

4.1 Introduction 94
4.2 Early (D_1) Deformation 95
4.2.1 Microstructures Related to Early (D_1) Deformation 95
4.2.2 Timing of Early Deformation (D_1) 95

4.3 D_2 Deformation 96
4.3.1 Microstructures Related to D_2 Deformation 96
4.3.2 Timing of D_2 and Exhumation of the TPC 97

4.4 D_3 Deformation 100
4.4.1 Microstructures Related to D_3 Deformation 100
4.4.2 Timing of D_3 Deformation and the Formation of East–West Trending F3 Folds 100
4.4.3 Microstructures Related to D_4 Deformation 101

4.4.4 Timing of D_4- Folding about the Gilmore Antiform and Static Retrograde Overprinting 101

4.5 Summary of Timing of Deformation in the TPC 102
4.6 Limited evidence for Acadian overprinting of the TPC 103
4.7 Tectonic Implications 103
4.8 Future Work 106

CHAPTER 5: CONCLUSIONS 109
COMPREHENSIVE BIBLIOGRAPHY 112
APPENDIX A: $^{40}AR/^{39}AR$ AND U-Pb ANALYTICAL RESULTS 125
APPENDIX B: SAMPLES AND STRUCTURES EXAMINED WITHIN THE TPC 143

LIST OF FIGURES

Comprehensive Literature Review

Figure 1-1: Simplified tectonic map of New England and southern Quebec **30**
Figure 1-3: Photomicrograph of UHP eclogite from Papua New Guinea **31**
Figure 1-4: Blueschist and eclogite in Eclogite Brook, TPC **32**
Figure 1-5: Metamorphic facies diagram **33**
Figure 1-6: Geologic Map of the TPC **34**
Figure 1-7: Microplate rotation model for exhumation **36**
Figure 1-8: Eduction model for exhumation **37**
Figure 1-9: Channel flow model for exhumation **38**
Figure 1-10: Tectonic wedging model for exhumation **39**
Figure 1-11: Theoretical $^{40}Ar/^{39}Ar$ age spectra **40**
Figure 1-12: Dynamic recrystallization of quartz **41**
Figure 1-13: Tectonic evolution of the Laurentian margin **42**
Figure 1-14: P-T-D path of rocks of the TPC and Belvidere Complex **44**
Figure 1-15: Geologic map of the TPC and Belvidere Complex with sample sites from additional geochronologic research **45**
Figure 1-16: $^{40}Ar/^{39}Ar$ age spectra from additional research in the area **47**
Figure 1-17: Summary of Taconic through Acadian metamorphism and deformation in northern Vermont and southern Quebec **49**

Results

Figure 3-1: Geologic map of the TPC with sample locations from this study **73**
Figure 3-2: Photomicrographs from selected samples **75–77**
Figure 3-3: F_2/F_3 folding in the TPC **79**
Figure 3-4: Structural data from Lockwood and Eclogite Brook **80**
Figure 3-5: SEM images from selected samples **81**
Figure 3-6: $^{40}Ar/^{39}Ar$ age spectra from white mica and glaucophane analyses **82–84**
Figure 3-7: $^{40}Ar/^{39}Ar$ age spectra from actinolite and tourmaline analyses **86**
Figure 3-8: Terra-Wasserburg Concordia diagram for titanite analysis **88**

Discussion

Figure 3-8: Terra-Wasserburg Concordia diagram for titanite analysis **108**

LIST OF TABLES

Table 3-1: Correlation of structures from the TPC area from previous research and this study. **89**
Table 3-2: Individual structural elements in thin section correlated with the four foliation generations interpreted for the evolution of the TPC. **90**
Table 3-3: Modal mineralogy based on observations made in thin section **92**
Table 3-4: Summary of $^{40}Ar/^{39}Ar$ data for samples examined in this research. **93**

CHAPTER 1: COMPREHENSIVE LITERATURE REVIEW

1.1 Introduction

High- to ultrahigh-pressure rocks give insights into tectonic processes occurring within continental subduction zones and at mantle depths, but the methods by which they are exhumed are disputed (Warren *et al.,* 2008; Kylander-Clark *et al.,* 2012; Zheng and Zhao, 2017). These rocks are the most important witnesses of the tectonothermal process that happen during the convergence between tectonic plates (Zhang *et al.,* 2007). Therefore, the timing and kinematics of high- to ultrahigh-pressure metamorphism and exhumation are critical elements for the development of tectonic models for collisional orogens, as well as for understanding subduction and exhumation processes, which impact the cycling of material between the crust and mantle (Augland *et al.,* 2010). Subduction zone related metamorphism was first recognized by the occurrence of glaucophane-bearing schist and related metamorphic rocks, where they are often also associated with ophiolites and other rocks of oceanic affinity (Dewey and Bird, 1970; Ernst, 1971; Zheng and Zhao, 2017).

The presence of glaucophane-bearing schist in the rocks of the Tillotson Peak Complex (TPC) in northern Vermont has been recognized since the research of Laird and Albee (1975). Early research interpreted the rocks of the TPC to have peak P-T conditions near the boundary of blueschist–eclogite-facies conditions during the Ordovician (Laird and Albee, 1981). More recently, research has estimated that peak conditions of blueschist and eclogite may have approached ultrahigh-pressure conditions (Honsberger, 2015; Gonzalez *et al.,* 2018).

The complex polyphase history that has impacted these rocks in the TPC since its formation gives insight to how these units were exhumed. Detailed structural and geochronologic data have been collected in southern Quebec and northern Vermont to understand the formation of low- to medium- grade Ordovician and Devonian -aged rocks (Figure 1-1). However, geochronologic constraints on the timing and deformation of high-pressure rocks, such as the TPC, are limited. Tectonic models for both southern Quebec and northern Vermont do not address in detail the exhumation of high- to ultrahigh-pressure rocks. Additionally, studies in Vermont on the timing of deformation and metamorphism along the Proto-North American margin rarely touch upon the impact of the Salinic Orogeny on the rocks of the region.

This study aims to correlate previous structural, petrologic, and geochronologic data from the TPC, northern Vermont, and southern Quebec with new research on the high-pressure rocks of the TPC to examine the P-T-t-D path of the TPC. Early research on the TPC yielded a single total fusion $^{40}Ar/^{39}Ar$ age from glaucophane (Laird *et al.*, 1984). Recent studies (Pidgeon, 2017; Gonzalez *et al.*, 2018; Tam *et al.*, 2018) have produced additional total fusion and step-heated $^{40}Ar/^{39}Ar$ ages from white mica in the TPC and the area proximal to it. In this study, step-heated $^{40}Ar/^{39}Ar$ and *in-situ* U-Pb dating are used to analyze a variety of minerals from the metamorphic rocks of the TPC. $^{40}Ar/^{39}Ar$ plateau ages, as well as age gradients and minimum ages in spectra, from this study and will be integrated with previous studies and new field and microstructural observations to estimate the timing of peak metamorphism, exhumation, and deformation of high-pressure rocks of the TPC. Correlating structures from the field to $^{40}Ar/^{39}Ar$ age

spectra will give a greater understanding on the impact of Taconic, Salinic, and Acadian orogenesis on rocks of northern Vermont. A further understanding on the timing of exhumation and deformation of high-pressure rocks in the TPC will likely yield questions to be addressed in future tectonic models.

1.2 The Formation and Exhumation of High- to Ultrahigh-Pressure rocks

1.2.1 Introduction:

High- to ultrahigh-pressure terranes are commonly identified by the presence of blueschist–eclogite-facies metamorphic rocks. Blueschist and eclogite are metamorphosed basaltic rocks that are characterized by their high concentrations of glaucophane and ompachite and garnet, respectively (Ota and Kaneko, 2010). Ultrahigh-pressure metamorphism is identified by the presence of coesite and microdiamond (Figure 1-2; Smith, 1984; Chopin, 1984; Liou *et al.*, 2004) in micron scale inclusions within mechanically strong minerals such as garnet omphacite, and zircon (e.g., Gillet *et al.*, 1984; Baldwin *et al.*, 2008). These index minerals are infrequently preserved other than in isolated boudins and lenses of ultrahigh-pressure material within host rocks such as schists or quartzofeldspathic gneiss (cf. Figure 1-3; Liou *et al.*, 2004).

Studies that examine the formation and exhumation processes of high-P, low-T metamorphic rocks yield important information about processes occurring deep within convergent margins (Agard *et al.*, 2009; Ernst, 2010). Prior to the discovery of coesite in crustal rocks (Smith, 1984; Chopin, 1984), there was a consensus that continental crust

did not subduct to depths >100km. The processes that bury these rocks to depth are fairly well understood, while there remains much to learn about the mechanisms by which they are exhumed (Hacker and Gerya, 2013; Agard *et al.,* 2009).

Ultrahigh-pressure terranes have recently been divided into two categories: small terranes that subducted and exhumed quickly, and terranes that are large, which are subducted and exhumed slowly (Kylander-Clark *et al.,* 2012). Ultrahigh-pressure bodies that are exclusively mafic tend to fall into the category of small terranes, while larger are frequently quartzofeldspathic in composition (Hacker and Gerya, 2013). Within the TPC, the composition of blueschist-facies rocks suggests a mid-ocean ridge basalt affinity (Laird *et al.,* 2001). Categorizing the TPC as an isolated body within the northern Appalachians identifies it as a small terrane, relative to others that are hundreds of km^2 in size (Hacker and Gerya, 2013).

1.2.2 Formation of High-Pressure to Ultrahigh-Pressure Terranes:

High- to ultrahigh-pressure rocks are stable only under high-P, low-T conditions, requiring formation during subduction related tectonics (Ota and Kaneko, 2010). The P–T conditions of the blueschist-facies is bounded on the low-P, low-T side by greenschist-facies, the low-P, high-T side by epidote–amphibolite-facies, and the high-P and high-T sides by eclogite-facies, respectively (Figure 1-4; Ota and Kaneko, 2010, Ernst, 2001). Ultrahigh-pressure metamorphism of continental crust occurs at P-T conditions ranging from ~700–950°C and >2.7–5.0 GPa (Ernst *et al.,* 2001; Liou *et al.,* 2004).

P-T conditions of formation of high-pressure rocks can vary over a broad range of high-P, low-T conditions (Ernst, 2001; Ota and Kaneko, 2010), however ultrahigh-pressure conditions are specific to the formation of coesite, a high-pressure polymorph of quartz, at >2.7 GPa, 700–950°C, and micro diamond (Liou *et al.*, 1994; Ernst, 2001). Hacker *et al.* (2011) and Hacker (2006) suggest that ultrahigh-pressure terranes rarely have peak metamorphic temperatures greater than 800°C; for in their model such temperatures would lead to melting, and a subsequently result in insufficient buoyancy for material to rise from the mantle. However, Auzanneau *et al.* (2006) suggest that at temperatures between 800–900°C partial melting may play a role in the exhumation of subducted material.

Hacker and Gerya (2013) discuss six separate tectonic settings by which continental crust can reach mantle depths: i) continental margin subduction, ii) microcontinent subduction, iii) sediment subduction, iv) intracontinental subduction, v) subduction erosion, and vi) foundering of a crustal root. In this study, we focus primarily on continental margin subduction as the method by which the protoliths of the TPC reached mantle depths. This is due to Taconian tectonic models, derived from regional structure, kinematics, and geochronology that suggest an eastward dipping subduction zone (relative to present coordinates) was present off the coast of Laurentia (Kim *et al.*, 2003; Thompson and Thompson, 2003).

1.2.3 Exhumation Mechanisms:

The presence of eclogite and blueschist preserved in the TPC has implications for regional tectonic models, as refined models must include a mechanism by which high-

pressure (≤ 2.5 GPa; Honsberger, 2015; Gonzalez *et al.,* 2018) rocks were exhumed from depths as great as ~70 km (Honsberger, 2015). The preliminary interpretations, from prior research, for this exhumation include; exhumation *via* back-thrusting and normal faulting (Tremblay and Pinet, 2016, and references therein), the emplacement of a tectonic wedge into low-grade metamorphic rocks and resultant normal faulting (Lamon, 2001), as disconnected blocks in a serpentine channel (Thompson and Thompson, 2003), and exhumation in a buoyant, low-viscosity channel above the subducting slab (Honsberger, 2015). In Honsberger's model (Honsberger, 2015), exhumation of the TPC from mantle depths to shallow crustal levels occurred in approximately 10 Myr.

While it is generally accepted that most ultrahigh-pressure terranes represent subducted continental margins (or fragments thereof), the mechanisms by which exhumation occurs is debated and varies globally (Warren *et al.,* 2008, Kylander *et al.,* 2012; Hacker and Gerya, 2013). To avoid retrograde overprinting on high-pressure structures, terranes must be exhumed at or greater than plate tectonic rates from mantle depths (Hacker and Gerya, 2013). Warren *et al.* (2008) states, with evidence from multiple terranes, that this rate is rapid from mantle to lower crustal levels followed by slower exhumation to the surface. The forces that drive exhumation consist of tectonic forces transmitted by plate motion and local body forces derived from the buoyancy of subducted rocks (Hacker and Gerya, 2013). This is explained with the understanding that at P-T conditions of ≤ 5 GPa, ≤ 800–900°C, continental crust is positively buoyant relative to the mantle (Massonne *et al.,* 2007). It is commonly inferred that the rapid rate of exhumation from mantle depths to lower crustal levels (Warren *et al.,* 2008) is driven

primarily by buoyancy contrast related to the density difference between the mantle and subducted material (Ernst, 2001; Liou *et al.,* 2004) after the subduction force has been removed or overcome. Exhumation is then a result of either or both the removal of overburden that accounted for high pressure, or by the transportation of these rocks through the overburden (Platt, 1993). Once near the surface (< 10 km), erosion can account for the remainder of exhumation and exposure of ultrahigh-pressure terranes (Burov *et al.,* 2014). The mechanisms that are examined in this paper as exhumation mechanism candidates for the TPC are *via* subduction zone reversal, channel flow, and tectonic wedging and back-thrusting.

Subduction Zone Reversal

Subduction zone reversal as a method of exhumation for high-pressure rocks is being examined in the TPC because of the presence of E–W trending macroscopic folds (Figure 1-5; Bothner and Laird, 1987) that trend approximately parallel to stretching lineations noted across the Green Mountain Anticlinorium (Thompson and Thompson, 2003). This is similar to lineation parallel high-strain folds related to exhumation in ultrahigh-pressure terranes elsewhere (Hacker *et al.,* 2000; Little *et al.,* 2007). Microplate rotation, and subsequent eduction are both mechanisms of exhumation related to subduction zone reversal (Hacker *et al.,* 2013).

The microplate rotation model for exhumation relies on the reversal of subduction polarity, as a result of plate rotation (Hacker *et al.,* 2013). In this model, the subduction plane is reactivated as a normal-sense shear zone (Figure 1-6; Webb *et al.,* 2008). Microplate formation in a complex tectonic margin with oblique convergence leads to the

rotation of microplates and the reversal of subduction polarity (Baldwin *et al.,* 2004). Exhumation by microplate rotation is estimated to occur at a rate of upwards of 12–40 mm per year (Baldwin *et al.,* 2004), with less refined determinations of > 2 mm per year (Hacker *et al.,* 2000).

Eduction, as described by Hacker *et al.* (2013), is a mechanism where continental lithosphere is exhumed as a result of polarity reversal, and the internal strain of subducted rocks is minimal. As continental crust is subducted into the mantle, slab pull exceeds slab strength and decoupling occurs (Figure 1-7; Anderson *et al.,* 1991; Duertz and Gerya, 2013). The removal of slab pull from the system results in rapid eduction (Anderson *et al.,* 1991) that is a function of the buoyancy of subducted continental lithosphere relative to the mantle (Warren *et al.,* 2008). The depth of slab break off relies on the rate of plate convergence; faster convergence results in break off at shallower depths than slower convergence rates (40–400 km; Duertz *et al.,* 2012). Continued exhumation through the crust is facilitated by the activation of a normal-sense shear zone near the former subduction interface (Schneider *et al.,* 2006; Duertz *et al.,* 2012).

Channel Flow Model

The exhumation of the high-pressure rocks of the TPC by means of a lubricated channel has been previously discussed by Honsberger (2015) and Thompson and Thompson (2003). Exhumation by means of channel flow or corner flow, relies on continued convergence and a subduction zone that contains buoyant material to bring ultrahigh-pressure rocks from mantle depths (Figure 1-8; Guillot *et al.,* 2000; Horodysky *et al.,* 2009). Exhumation of oceanic and continental material from within the channel

results from the continuous introduction of new material into the channel, which is lubricated by low-density, low-viscosity materials at depths (Li *et al.*, 2016). Gerya *et al.* (2002) proposed that a driving force for this type of exhumation was the addition of water into the subduction zone and the serpentinization of mantle material, creating a low-viscosity channel where high- to ultrahigh-pressure material would be exhumed. As material is continuously added to the channel, return-flow forces blocks that have been subducted back to shallow depths (Federico *et al.*, 2007).

Tectonic Wedging and Back-thrusting

The possibility of exhumation as a result of thrusting and later normal faulting in the northern Appalachians has been discussed by Lamon (2001) and Tremblay and Pinet (2016). Lamon (2001) details a wedge of medium- to high-pressure metamorphic rocks that were emplaced in a "wedge" into low-pressure rocks, that was facilitated by the activation of Prospect Rock Fault as a roof thrust, with a yet identified basal thrust (Figure 1-9). In their research, a top-to-the-E shear sense and metamorphic gradient that increased from west to east, were cited as evidence for movement along the Prospect Rock Fault. The final exhumation of high-grade metamorphic rocks (TPC) is inferred to be related to pre-Acadian normal faulting that removed overburden (Lamon, 2001). Tremblay and Pinet (2016) interpreted that the exhumation of ophiolites, as well as blueschist and eclogite of the TPC, was a result of transportation to the SE during Salinic back-thrusting, and subsequent Salinic normal faulting (such as the Burgess Branch Fault Zone; Gonzalez *et al.*, 2018) that resulted in the removal of overburden and transportation to the surface.

1.2.4 Geochronology:

To further understand the timing of metamorphism, exhumation, and deformation of the metamorphic rocks of the TPC, this study relies on the step-heated $^{40}Ar/^{39}Ar$ dating technique to obtain ages from samples collected in the field (McDougall and Harrison, 1999). $^{40}Ar/^{39}Ar$ geochronology evolved from the K/Ar dating scheme. Potassium is commonly found in many rock-forming minerals, and the half-life of radiogenic ^{40}K is ~1250 Ma (Kossert and Günther, 2004). The $^{40}Ar/^{39}Ar$ dating technique relies on the irradiation of samples with fast neutrons to transform a proportion of the ^{39}K atoms to ^{39}Ar, and the subsequent analyses of gaseous Ar isotopic ratios in a mass spectrometer to calculate an age spectra (Harrison and Zietler, 2005). To have a detailed understanding of the timing of distinct deformation events, it is imperative to target minerals that provide structural and metamorphic context.

Step-heated $^{40}Ar/^{39}Ar$ geochronology utilizes incremental heating of samples, which results in "steps" in the age spectra that represent apparent ages, that may be related to aspects of the sample history such as the initial crystallization of the mineral or later deformation (e.g., Fleck *et al.,* 1977). In high-pressure settings, apparent age spectra may provide constraints on the exhumation and cooling history of samples (cf. Ratschbacher *et al.,* 2000). The spectra that is examined has the total % of ^{39}Ar released on the X-axis, the apparent age on the Y-axis, and is plotted in a way where ages correlate to boxes, with their thickness representing the error (Figure 1-10). Plateau ages in age spectra are defined as a flat release pattern in the spectra that encompasses >50% of the total ^{39}Ar released in the experiment (McDougall and Harrison, 1999), and are

inferred to be related to the original crystallization age of the mineral or the time of cooling through a temperature at which ^{40}Ar diffusion out of mineral effectively ceases. For samples that do not yield a plateau, it is possible to measure an integrated total gas age—the equivalent of a K/Ar or total fusion age. Total fusion analyses require the heating of the sample in a single step, and the measurement of the ratios of all isotopes in the sample (Harrison and Zietler, 2005). Total fusion analyses and integrated ages from step-heated analyses may be inaccurate representations of metamorphic ages in polyphase orogens, because they mask age gradients that may result from slow cooling, reheating, or partial resetting due to deformation (McDougall and Harrison, 1999).

When examining an $^{40}Ar/^{39}Ar$ age spectra, an idealized version of the spectra for a crystal that cools rapidly, and is undisturbed after initial crystallization, is expected to look nearly flat with a plateau that encompasses most if not the whole spectra (Figure 1-10; McDougall and Harrison, 1999). In addition, McDougall and Harrison (1999) discuss two additional potential spectra results that are easily distinguishable; one where there has been a geologically recent event that disturbs the mineral, and an additional where the mineral was disturbed long ago (Figure 1-10).

Simply put, any K-bearing mineral or rock can be used for K-Ar or $^{40}Ar/^{39}Ar$ geochronology (Harrison and Zietler, 2005). In this study, we examine actinolite, glaucophane, tourmaline, and white mica as possible targets. Amphiboles typically contain 0.1–1.0% K, and therefore the possibility of contamination with excess Ar makes dating limited (Harrison and Zietler, 2005). It is important to note that in metamorphic amphiboles exsolution can have significant impact on Ar retention (Harrison and Fitz

Gerald, 1986). Therefore, $^{40}Ar/^{39}Ar$ analyses of amphiboles from within the TPC may be difficult (see Smelik and Veblan, 1989, 1991). Actinolite is not targeted as frequently as other K-bearing minerals, however it can be dated successfully to examine the timing of greenschist-facies metamorphism (e.g., Borojević Šoštarić *et al.,* 2014; Zhang *et al.,* 2018, and references therein). Glaucophane that has been separated from blueschist and dated often yields younger $^{40}Ar/^{39}Ar$ ages than white mica from the same sample (McDougall and Harrison, 1999). Tourmaline, a relatively new $^{40}Ar/^{39}Ar$ geochronometer, is useful for this research because it is not sensitive to chemical or mechanical alteration and it is stable over a wide range of P-T conditions (up to 6 GPa and 850° C; Jourdan and Thern, 2014). Therefore, it can be used to date the peak metamorphism of high-pressure samples as well as the metamorphism of lower grade rocks (i.e., pelitic schist; Korsakov *et al.,* 2008; Bea *et al.,* 2009). White mica typically contains 8–10% K concentration, is common in metamorphic rocks, and is typically retentive of radiogenic Ar below ~ 400°C (Purdy and Jäger, 1976; Harrison and Zietler, 2005). Warren *et al*. (2012) address the difficulty of using white mica ages from $^{40}Ar/^{39}Ar$ analyses to determine the timing of high-pressure metamorphism. These authors conclude that the P-T conditions of formation are necessary to ensure certainty that ages represent crystallization ages rather than cooling ages.

1.2.5 Understanding Deformation Mechanisms with Microstructures

To address the question of P-T conditions associated with metamorphic assemblages without utilizing petrologic modeling and microprobe work, we can rely on the microstructures of quartz in association with deformation-related microstructures

examined in thin section (Passchier and Trouw, 2005). If the rocks of the TPC reached ultrahigh-pressure conditions, as current research may imply (Honsberger, 2015; Gonzalez *et al.,* 2018), the observation of coesite is a possibility. Coesite, a high-pressure polymorph of quartz, is commonly preserved in ultrahigh-pressure metamorphic rocks as inclusions in minerals with radial fractures that form during a volumetric change related to the transition of coesite to quartz (Figure 1-2; cf. Baldwin *et al*., 2008).

Quartz is present in most of the metamorphic rocks of the TPC (Laird and Albee, 1981; Bothner and Laird, 1987) and the morphology of individual grains can give insight as to the P-T conditions under which they have been deformed. At very low-grade (< 300°C) conditions, brittle fracturing in quartz is the dominant deformation mechanism, with pressure solution and solution transfer of material also present (Dunlap *et al.,* 1997; van Daalen *et al.*, 1999; Stipp *et al.*, 2002). At these conditions the characteristic structures examined are fractures in grains and undulose extinction (Nishikawa and Takeshita, 1999). At low-grade conditions (300–400°C), characteristic structures are undulose extinction and deformation lamellae (Hirth and Tullis, 1992; Stipp *et al.,* 2002). The dominant dynamic recrystallization mechanism at these conditions is by bulging recrystallization, with bulges and small recrystallized grains along quartz grain boundaries (Figure 1-11; Stipp *et al.*, 2002). At medium temperatures (400–500°C) the dominant recrystallization mechanism is subgrain rotation recrystallization (Figure 1-11; Lloyd and Freeman, 1994; Stipp *et al.,* 2002). At high temperatures (500–700°C) recrystallization of quartz is mostly by grain boundary migration, where grain boundaries are irregular and have an amoeboid/lobate shape (Figure 1-11; Stipp *et al.*, 2002). After

deformation ceases, it is possible for recrystallization and grain boundary area reduction to continue if temperatures remain high (Kruhl, 2001). The resultant structure observed in thin section is quartz grains that have 120° triple junctions.

1.3 Geologic Setting of the Tillotson Peak Complex

The Tillotson peak Complex in northern Vermont represents a rare slice of material that has been subducted to mantle depths and exhumed to the surface without total retrograde overprinting of prior structures. Throughout New England; the estimate of P-T conditions for the TPC (Honsberger, 2015) remains the highest, and therefore understanding the exhumation history of the TPC is vital to understand the tectonic history of the eastern margin of Proto-North America. From the timing of peak metamorphism of the TPC to the present, a minimum of three tectonic events have modified this margin.

1.3.1 Regional Geology

The complex tectonic history of the North American margin is recorded within the rocks of Northern Appalachians and much of Vermont (Figure 1-1; Stanley and Ratcliffe, 1985; Thompson and Thompson, 2003; Kim *et al*., 2003). Many of these rocks were deposited in an ancient rift and resultant ocean basin that developed east of Laurentia (Kim *et al*., 2003) prior to the onset of the Taconic Orogeny. Since the deposition of these rocks, they have experienced deformation related to a minimum of three phases of regional metamorphism (Laird and Albee, 1981b; Castonguay *et al*., 2012).

In the early Paleozoic, rifting of the supercontinent Rodina lead to the formation of narrow rift basins that were filled in with clastic and volcanic rocks (Cawood *et al*., 2001), and eventually, transitioned to drift and the opening of the Iapetus Ocean (Figure 1-12). This transition from rifting to drifting is the stage in the evolution of a passive margin at which rift faulting ceases and seafloor spreading begins (Neuendorf *et al*., 2011). Sediments deposited in the Iapetan Ocean lithified into the carbonates and siliclastic units that compose the carbonate platform (CP; Figure 1-1) in western Vermont.

1.3.2 Tectonic Model for the Taconic Orogeny

The Taconic Orogeny is associated with at least two phases of metamorphism and deformation, lasting from the late Cambrian to the Ordovician (~505–445 Ma; Laird *et al*., 1984; Stanley and Ratcliffe, 1985; Castonguay *et al*., 2012; Tremblay and Pinet, 2016, and references therein). Additional interpretations include a third phase of metamorphism during the late Taconic (van Staal et. al., 2007). During the late Cambrian and Early Ordovician, oceanic crust began to subduct along an eastward-dipping (relative to present coordinates) subduction zone off the coast of Laurentia (Figure 1-12), and arcs formed above it (e.g., Shelburne Falls Arc; Karabinos *et al*., 1998). During this time, ophiolites and medium- to high-pressure metamorphic rocks of Quebec and the Belvidere Mountain Complex were initially metamorphosed (~505–486 Ma; Laird *et al*., 1984, 1993; Whitehead *et al*., 1996; Castonguay *et al*., 2012; Ratcliffe *et al*., 1998).

After ophiolite formation, the metamorphic sole of ophiolites, and potentially high-pressure rocks such as the TPC, were exhumed during a relatively short time period (<10 Myr; Honsberger, 2015). The process of subduction along the Laurentian margin culminated in the accretion of peri-Laurentian arc environments, and ophiolites (Figure 1-12; Stanley and Ratcliffe, 1985; Karabinos *et al*., 1998). Ages recorded between 471 and 456 Ma (D_E; Castonguay *et al*., 2012) are inferred to be related to low–medium-pressure metamorphic and cooling ages during and after the collision stage along the Laurentia margin (Karabinos *et al*., 2017). In New England and northern Vermont, it is interpreted that the main cause of the Taconic Orogeny was a result of the closure of the Neo-Iapetan Ocean and the associated collision of thrust slices and arc-environments, such as the Shelburne Falls Arc and Moretown Terrane, with the Laurentian Margin (Figure 1-12; Karabinos *et al*., 1998; Kim *et al*., 2003; Macdonald *et al*., 2014).

This collision led to the obduction of thrust slices, such as the Rowe-Hawley Belt (RHB, Figure 1-1), onto Laurentia (Stanley and Ratcliffe, 1985), which were originally deposited as sediments and rift volcanics during the late rift to early drift stage of the opening of the Iapetus Ocean (Thompson and Thompson, 2003). The Rowe-Hawley Belt in north-central Vermont, which encompasses the TPC and Belvidere Mountain Complex, is a tectonic assemblage of continental margin, oceanic, and suprasubduction zone rocks that were juxtaposed during the Ordovician Taconic Orogeny, and later deformed and metamorphosed by the Silurian Salinic Orogeny and Devonian Acadian Orogeny (Kim *et al*., 2010; Castonguay *et al*., 2012). Research from Laird *et al*. (1984, 1993) suggests that the rocks of the western Rowe-Hawley Belt are generally medium–

high-pressure facies (e.g., TPC, Belvidere Mountain Complex), where rocks of the Moretown Formation Slices to the east formed at low-pressure conditions.

Younger Taconian ages preserved in the northern Appalachians (455–445 Ma; Ratcliffe *et al*., 1998; van Staal *et al*., 2007) are thought to represent the long-continued subduction and collision along this margin with Laurentian arc environments, the timing of which is associated with the timing of formation of the Bronson Hill Arc (Tucker and Robinson, 1990), as well as the collision of present-day southern New England with the Moretown Terrane (Karabinos *et al.*, 2017).

1.3.3 Tectonic model for the Salinic Orogeny

The extent to which the Silurian Salinic Orogeny impacted New England was studied in little detail until recently (Rankin *et al*., 2007; Castonguay *et al*., 2012; Karabinos *et al*., 2017; Gonzalez *et al*., 2018; Tam *et al*., 2018). The best documentation of structures preserved during this event is located in Maine, New Brunswick, and Newfoundland (West *et al*., 1992; van Staal and de Roo, 1995; van Staal. *et al*., 2009). In northern Vermont, the impact of the Salinic Orogeny is only recently studied in $^{40}Ar/^{39}Ar$ age spectra (Castonguay *et al*., 2012; Tam *et al*., 2018), and structures observed have yet to be fully correlated with Silurian structures observed in Maine and Canada.

The orogeny is composed of two separate regimes that preserve compressional and extensional related structures (Castonguay *et al*., 2001, 2007; Pinet, 2013; Tremblay and Pinet, 2016, and references therein). The cause of this orogeny is interpreted to be associated with the docking of Ganderia onto Proto-North America following a

subduction flip (SE to NW) at the end of the Taconic Orogeny (Figure 1-12; van Staal and Barr, 2012; Tremblay and Pinet, 2016) resulting in hinterland directed folds, back-thrusts, and retrograde metamorphism (Tremblay and Castonguay, 2002; Tremblay and Pinet, 2016). It is interpreted that at this time, continental and oceanic material that was subducted, including ophiolites and the TPC, were transported towards the SE in the hanging wall of back-thrusts, and may be locally exhumed to the surface (Tremblay and Pinet, 2016). Regional extension, associated with the formation of large-scale normal faults like the Burgess Branch Fault Zone, as well as the formation of the Connecticut Valley Gaspé Trough (CVGT; Figure 1-1) is interpreted to be related to asthenospheric upwelling and resultant isostatic uplift and collapse following the docking of Ganderia (Figure 1-12; Tremblay and Pinet, 2005).

1.3.4 Tectonic model for the Acadian Orogeny

From the Salinic Orogeny to the onset of the Acadian, the mountains to the west were eroded significantly, and shales, limestones, and sandstones were deposited in the elongate basins extending from southern New England to the Gaspé Peninsula (CVGT; Figure 1-1; Tremblay and Pinet, 2005). The Devonian Acadian orogeny is interpreted to be a result of closing of the Iapetus Ocean between the composite North American margin and Avalonia, and a narrow seaway that separated Avalonia from Ganderia (Figure 1-12; Hussey *et al*., 2010).

When collision began during the Acadian, Ganderia was fully assembled onto the North American margin as a part of the preceding Salinic Orogeny (van Staal and Barr, 2012). After the onset of collision, deformation and metamorphism was dominantly

related to magmatism (Tremblay and Pinet, 2016, and references therein). The intrusion of granitoid bodies is interpreted to have occurred around 394–355 Ma (Naylor, 1971; Laird *et al*., 1984; Eusden *et al*., 2000). Deformation along the North American margin is continuous during and after the emplacement of Acadian plutons (Red, Figure 1-12d; Lagor, 2016). In northern Vermont and southern Quebec, the compression related to the collision phase of this orogeny is preserved as N–S striking large-scale folding, such as the Green Mountain Anticlinorium and Sutton Notre Dame Mountains Anticlinorium (Tremblay and Pinet, 1994; Thompson *et al*., 1999). Locally, retrograde metamorphism is related to metamorphism during magmatism and collision (Laird *et al*., 1993; Castonguay *et al*., 2012).

1.3.5 Geology of the TPC

Evidence of the peri-Laurentian Taconic subduction zone is preserved *via* the blueschist and eclogite of the TPC in northern Vermont (Laird and Albee, 1981; Bothner and Laird, 1987). The primary phase of Taconian metamorphism of these rocks is interpreted to have occurred between 471–460 Ma (Laird *et al*., 1984, 1993). The estimate for peak metamorphic conditions of the TPC (≤ 2.5GPa; Laird and Albee, 1981; Honsberger, 2015; Gonzalez *et al*., 2018) reflect the highest-pressure Taconian metamorphism that is preserved in Vermont. Laird *et al*. (2001) determined that, because of their depleted light rare earth element content, likely protoliths for the mafic schists within the TPC were Iapetan midocean ridge basalts formed during seafloor spreading.

The TPC is composed of blueschist- and eclogite-facies metapelites, metabasalts, and ultramafics. The complex is located on the eastern limb of the Green Mountain

Anticlinorium, within the Rowe-Hawley Belt (Figure 1-1; Laird and Albee, 1981; Laird *et al*., 2001; Kim *et al*., 2001). High-pressure rocks of the TPC preserve the highest-pressure Taconian metamorphism in northern Vermont (Laird and Albee, 1981; Honsberger, 2015). Additional high-pressure metamorphic rocks that have been heavily overprinted, like much of the TPC, are present in the Baie Verte Peninsula, Canada (Castonguay *et al*., 2014) and in northwest Connecticut (Chu *et al*., 2015).

Early P-T estimates on high-pressure rocks of the TPC gave lower P-T range of 0.9 GPa, 360°C–1.1 GPa, 470°C, which were estimated from omphacite inclusions and adjacent garnets. Additionally, higher P-T ranges of 1.2 GPa, 520°C–1.4 GPa, 620°C (Laird and Albee, 1981; Laird *et al*., 1993, 2013) were determined from garnet rim-omphacite pairs. Laird *et al*. (1993) estimated a range of metamorphic temperatures of pelitic rocks to be 440°C–567°C at 1.0 GPa due to the petrologic relationships of minerals in these rocks. More recently, Honsberger (2015) and Gonzalez *et al*. (2018) have determined that peak metamorphism of the blueschist and eclogite-facies rocks within the TPC reached conditions upwards of 2.5 GPa, 510–510°C at ~70 km below the surface (Figure 1-13). Petrologic modeling also determined that the growth of actinolite occurred at or below ~0.3–0.4 GPa, magnesio-hornblende at ~0.8–1.0 GPa, and barroisite at ~1.2–1.3 GPa (Honsberger, 2015). The P-T estimates for peak and retrograde metamorphism led researchers to the conclusion that exhumation of the TPC from > 60 km below the surface to ~10 km occurred over the course of 10 Myr (Honsberger, 2015b). Laird and Albee (1981) inferred that greenschist-facies metamorphism, which

overprints much of the TPC, is related to metamorphism along the end of the retrograde path during the Acadian Orogeny.

The primary units within the field area are the Hazens Notch Formation, the Haystack-Tillotson Slice, and ultramafic lenses (Bothner and Laird, 1999; Figure 1-5). Descriptions of rock types come from field observations and bedrock mapping by Bothner and Laird (1999). The TPC is mapped on all sides as in thrust contact with the Hazens Notch Formation. In the field area, the Hazens Notch Formation (Figure 1-5) is a black to rusty weathering schist with albite, graphite, chlorite, and minor sulfides. The Hazens Notch Formation also includes a felsic gneiss member in this field area. Felsic gneiss, the most expansive unit in this field area, is typically gray to greenish gneiss, with varied color dependent on chlorite content. Isolated ultramafic lenses found along the contact of the Hazens Notch Formation with blueschist, eclogite, and felsic gneiss members of the Hazens Notch Formation display a weak foliation. Blueschist and eclogite of the Haystack-Tillotson slice are dark blue–gray in color, and are distinguished from other rocks in the area by their glaucophane and garnet content, as well as their hardness relative to other rocks of the TPC. On Tillotson Peak, proximal to Lockwood Brook, pelitic schist is intercalated with blueschist and eclogite. This intercalated pelitic schist is distinguished from the Hazens Notch schist *via* a lack of graphite and rusty weathering. Boudins of amphibolite and eclogite are present within layers of felsic gneiss and pelitic schist (Figure 1-3).

Discontinuously zoned amphiboles (i.e., barroisite and glaucophane overgrown by actinolite; Laird and Albee, 1981) and amphibole grains with exsolution lamellae (i.e.,

winchite and cummingtonite in glaucophane; Smelik and Veblan, 1989, 1991) have been documented within the TPC. This and the structural and metamorphic context of the TPC give evidence to a complex polyphase history.

1.3.6 Geology of the Belvidere Mountain Complex and ophiolites in Quebec

The Belvidere Mountain Complex is a sequence of serpentinized ultramafics, amphibolite, and metapelites that formed under medium- to high-pressure conditions along the Taconian suture zone (Figure 1-14; Gale, 1980; Laird and Albee, 1981b; Laird *et al*., 1984; Laird and Honsberger, 2013). Within the Belvidere Mountain Complex, the earliest Taconian structure (Gale, 1980) and metamorphism (473–505 Ma; Figure 1-13–1-15; Laird *et al*., 1984, 1993; Castonguay *et al*., 2012) in Vermont is preserved. The rocks of the Belvidere Mountain Complex are thought to have been metamorphosed and deformed prior to the rocks of the TPC, before being structurally juxtaposed with surrounding metasedimentary rocks at 470–460 Ma (Bothner and Laird 1987; Kim *et al*., 2003). Research from Gale (1980) on the geochemistry of the rocks of the Belvidere Mountain Complex suggests a mid-ocean ridge basalt or back arc basin basalt protolith for amphibolite and mafic schist.

The Taconic orogeny in Quebec is attributed to the emplacement of ophiolites, like the Belvidere Mountain Complex (Tremblay *et al*., 2011), that formed during the early stages of Laurentian subduction. Ophiolites in Quebec have similar ages to the mafic schist and amphibolite dated in the Belvidere Mountain Complex that suggest metamorphism at 473–504 Ma (David and Marquis, 1994; De Souza *et al*., 2012; Whitehead *et al*., 1996; Tremblay *et al*., 2011; Castonguay *et al*., 2012; Laird *et al*.,

1984). Estimated P-T conditions for the metamorphism of ophiolites in Quebec are summarized by Tremblay and Pinet (2016) including a range of 0.5–0.7 GPa, 500–850°C estimate for the Thetford mines area and a range of 0.6–0.9 GPa, 600–800°C (Feininger 1981; Clague *et al*., 1981; O'Bierne-Ryan *et al*., 1990). Recent estimates from petrologic modeling on rocks of the medium- to high-pressure rocks of the Belvidere Mountain Complex constrain P-T conditions of 1.2–1.3 GPa, 500–510°C (Figure 1-13; Honsberger, 2015). Other data derived from the amphibolite of the Belvidere Mountain Complex yielded P-T estimates of ~0.9 GPa, 550–650°C for the growth of barroisite (Laird *et al*., 1993).

1.3.7 Structural Geology

The structural data presented in this paper combines the observations of previous researchers in the TPC and the region (Kim *et al*., 2003; Bothner and Laird 1987, 1999; Thompson and Thompson, 1999, 2003) with observations and conclusions made during this study. Previous researchers discuss at least three dominant deformation events in northern Vermont. D_1 and D_2 are attributed to deformation during the Ordovician Taconic Orogeny, while D_3 is attributed to the Devonian Acadian Orogeny (Figure 1-16). An additional phase of deformation during the Silurian has been examined in Quebec, and recently researchers have investigated the Salinic impact on rocks of Vermont (Castonguay *et al*., 2012; Karabinos *et al*., 2017; Tam *et al*., 2018) to compare with correlative structures in Maine and Canada.

S_0, lithologic layering, is rarely preserved in northern Vermont and is frequently transposed by the development of later foliations (Kim *et al*., 1999, 2003; Tremblay and

Pinet 2016). Bothner and Laird (1987) interpret S_0 in the TPC to be preserved as 2–5 cm thick amphibole and garnet-rich compositional layers in mafic rocks.

Throughout northern Vermont, D_1 structures are attributed to early Taconian underplating and obduction onto the Laurentian margin (Thompson and Thompson, 2003). In most areas S_1 and S_2 are a composite fabric, roughly paralleling one another (Kim *et al*., 2003). In northern Vermont, S_1 is most frequently examined in quartzite beds (Thompson *et al*., 1999). Prior research in TPC suggests that S_1 is the dominant foliation in the field area, that is interpreted to parallel or closely parallel original lithologic layering, and is axial planar to small isoclinal F_1 folds (Bothner and Laird, 1987). F_1 folds in northern Vermont are typically rootless sheared isoclinal folds with fold axes that parallel L_1 quartz lineations, which trend E–W from the Lamoille River south to the Winooski River (Thompson and Thompson, 1999). D_1 in both the Belvidere Mountain Complex and the TPC are associated with zoned amphibole (barroisite–hornblende in the Belvidere Mountain Complex and glaucophane–actinolite in the TPC; Laird and Albee, 1981; Bothner and Laird, 1987).

D_2 deformation in northern Vermont occurred during the development of back-folds and back-thrusts during the Late Taconian Orogeny (Thompson and Thompson, 2003). S_2 in the TPC is a spaced crenulation cleavage, most commonly examined in metapelite samples, related to E–W trending F_2 folds that generate the map-scale pattern of the TPC (Bothner and Laird, 1987). F_2 folds are upright-to-lightly reclined E–W trending folds that are distinct from the dominant N–S trending Taconic and Acadian fold axes of northern Vermont (Cady *et al*., 1963; Bothner and Laird, 1987). Regionally, F_2

folds are reclined isoclinal folds, and are axial planar to the dominant foliation (Thompson *et al*., 1999, Kim *et al*., 1999). Thompson and Thompson (2003) interpret D_{1-2} regionally to be related to west-directed peak metamorphism.

Acadian deformation is attributed to D_3 structures in northern Vermont. This includes N–S trending F_3 folding associated with formation of the Green Mountain Anticlinorium, an associated west-dipping spaced crenulation cleavage, and the intrusion of granitoid bodies (Kim *et al*., 1999). In the TPC, F_3 folding is not visible in outcrop or thin section, however folding about the NW-trending Gilmore Antiform is confirmed by the observation of fold axes measurements from Lockwood Brook and Eclogite Brook (Bothner and Laird, 1987). S_3 in the field area is a north-striking crenulation cleavage primarily documented in felsic gneiss and blueschist bodies (Bothner and Laird, 1999). In the rest of northern Vermont, this fabric is a north-striking spaced crenulation that is especially well developed in phyllites (Thompson *et al*., 1999).

1.4 Geochronologic Constraints for Metamorphism in northern Vermont and southern Quebec

The timing of metamorphism in northern Vermont and southern Quebec can be constrained to be related to three main tectonic events; D_E, D_M, and D_L (i.e., D_{early}, D_{middle}, and D_{late}; Figure 1-16; Castonguay *et al*, 2012). In Vermont and Quebec, D_E has been attributed to two–three phases of deformation during the Taconic Orogeny, D_M has been correlated an extensional and compressional event during the Salinic Orogeny, and D_L is attributed to the deformation related to magmatism and regional metamorphism during the Acadian Orogeny (Castonguay *et al.*, 2012). Until recently, two main tectonic

events are interpreted to have occurred in Vermont (D_E & D_L), with little emphasis on the impact of Salinic orogenesis (Laird *et al*., 1984, 1993). Comparing Silurian ages in Vermont on similar lithologies and structures to those with reported Salinic ages in southern Quebec is important in understanding the development of the North American margin.

1.4.1 Metamorphism During the Early Taconic Orogeny

The oldest Taconian metamorphic rocks preserve deformation that occurred after rifting transitioned to collision along the Laurentian margin at 505–473 Ma (Figure 1-14, 1-16; Laird *et al*., 1984; Whitehead *et al*., 1996; Malo *et al*., 2008; Castonguay *et al*., 2012). These ages represent the formation of metamorphic soles and low-pressure metamorphic rocks composed of metapelites, metabasites, and metaclastic rocks at the base of the ophiolite-mantle sequence (e.g., Belvidere Mountain Complex, Thetford Mines Ophiolite, and the metamorphic sole of the Pennington Sheet; Laird *et al*., 1984; Kim *et al*., 2003; Tremblay and Pinet, 2016; Whitehead *et al*., 1996). Young ages that bracket this range for ophiolite formation (e.g., 475 ± 3 Ma; Castonguay *et al*., 2012) may be an inaccurate representation of peak metamorphism due to retrogression and low potassium content in examined samples. They are also interpreted to reflect a cooling history after formation (Karabinos *et al.*, 2017).

1.4.2 Metamorphism During the Late Taconic Orogeny

Primary Taconian metamorphism and deformation in Vermont and Quebec is interpreted to have occurred from 471–456 Ma, indicated from $^{40}Ar/^{39}Ar$ and U-Pb ages

on a multitude of samples (Laird *et al*., 1984, 1993; Castonguay *et al*., 2001, 2003, 2012; Tremblay and Pinet 2016, and references therein; Karabinos *et al*., 2017). Early studies in Vermont suggest that peak thermal conditions were reached at 465 ± 5 Ma (Laird *et al*., 1984; Sutter *et al*., 1985) and that the main phase of Taconian deformation lasted from 470–440 Ma. This range includes the 468 ± 6.4 Ma age on glaucophane from the TPC that was originally inferred to be related to the peak metamorphism of eclogite-facies metamorphic rocks (Laird *et al*., 1984). Additional research from Vermont and Quebec (Spear and Harrison, 1989; Tremblay and Pinet, 2016) suggests that ages recorded younger than ~445 Ma may be related to post-Taconic deformation during the Silurian.

1.4.3 Metamorphism during the Salinic Orogeny

The Silurian Salinic Orogeny has been discussed in little detail as a driving force for deformation and metamorphism of rocks of northern Vermont, with few exceptions that relate the tectonometamorphic history of southern Quebec with northern Vermont (Castonguay *et al*., 2012). Spear and Harrison (1989) discuss the possibility of Salinic deformation occurring between 440–415 Ma, utilizing the minimum ages of complex $^{40}Ar/^{39}Ar$ spectra. Laird *et al*. (1984) calculated a step-heated $^{40}Ar/^{39}Ar$ age of 415 ± 3.8 Ma on amphibole from the Stowe formation. Recent research from medium- to high-pressure metamorphic rocks of northern Vermont (Castonguay *et al*., 2012, Tam *et al*., 2018) suggests that Salinic deformation occurred from ~446–415 Ma. Evidence for Silurian metamorphism in Quebec and Newfoundland has been examined in greater detail, and the timing is determined to be ~433–405 Ma (Castonguay *et al*., 2001, 2007;

Tremblay and Pinet, 2016). The earliest stages of Salinic deformation in Quebec are estimated to have started around 440–435 Ma (Castonguay *et al*., 2001, 2007; Tremblay and Pinet, 2016, and references therein). The orogeny is further separated into two dominant events, a compressional period that occurred from ~433–420 Ma and an extensional regime that lasted from ~420–405 Ma (Castonguay *et al*., 2001, 2007, 2012; Tremblay and Pinet, 2016, and references therein). Recent research (Gonzalez *et al*., 2018) along the Burgess Branch Fault Zone in northern Vermont suggests that it may have formed during the same time as Salinic normal faults in Quebec.

1.4.4 Acadian Overprinting on the rocks of the Northern Appalachians

The bracket of timing of Acadian metamorphism and deformation in northern Vermont was defined by Laird *et al*. (1984) to be 386–355 Ma. The early interpretation from analyses on metapelites and mafic rocks was that this timing was related to the greenschist overprinting in northern Vermont on medium- to high-pressure facies rocks (Laird and Albee, 1981) that had an age of 460 ± 10 Ma (Laird *et al*., 1984, 1993). In an additional study in New England, Sutter *et al*. (1985) find that metamorphism during the Acadian was likely around 376 ± 5 Ma. In southern Quebec, researchers constrain the timing of Acadian metamorphism to be ~390–376 Ma (Tremblay *et al*., 2000; Castonguay *et al*., 2012). These data shows a diachronous trend in ages from New England to Quebec (Tremblay and Pinet, 2016, and references therein).

1.4.5 Recent Studies in the TPC

To date, there is yet to be a detailed study on the pressure-temperature-time-deformation (P-T-t-D) path of high-pressure rocks of the TPC. While there has been research on the geochemistry, structure, and petrography of the TPC, little research focuses on the structural and metamorphic history of the TPC with relationship to time. For decades, a single 468 ± 6.4 Ma total fusion $^{40}Ar/^{39}Ar$ age on glaucophane from Laird *et al*. (1984) has been the sole geochronologic constraint available in the published literature. $^{40}Ar/^{39}Ar$ total fusion ages from recent work (Figure 1-14, 1-15) indicate that high-pressure subduction zone metamorphism (1.6–2.5 GPa, 450–510°C; Honsberger, 2015; Gonzalez *et al*., 2018) occurred between 480–468 Ma. Total fusion ages likely only constrain a minimum age for high-pressure metamorphism due to the polymetamorphic history (McDougall and Harrison, 1999) of the TPC. Therefore, $^{40}Ar/^{39}Ar$ total fusion analysis of amphibole may not be accurate (i.e., yielding mixed ages).

Recent data from Pidgeon (2017) and Tam *et al*. (2018) have resulted in white mica plateau ages from metapelites and blueschist of the TPC of 456.7 ± 1.8 Ma (1σ) to 466.2 ± 1.5 Ma (1σ). Minimum ages and age gradients in samples from both studies give evidence to a lower temperature Silurian disturbance (Figure 1-14, 1-15; Pidgeon, 2017; Tam *et al*., 2018). These data and the $^{40}Ar/^{39}Ar$ total fusion age on glaucophane from Laird *et al*. (1984) are concordant with constraints on the timing of eclogite-facies metamorphism that occurred in the Baie Verte Peninsula, Canada (465 Ma; Castonguay *et al*., 2014) and in northwest Connecticut (456 ± 11 Ma; Chu *et al*., 2015) during the Taconic Orogeny.

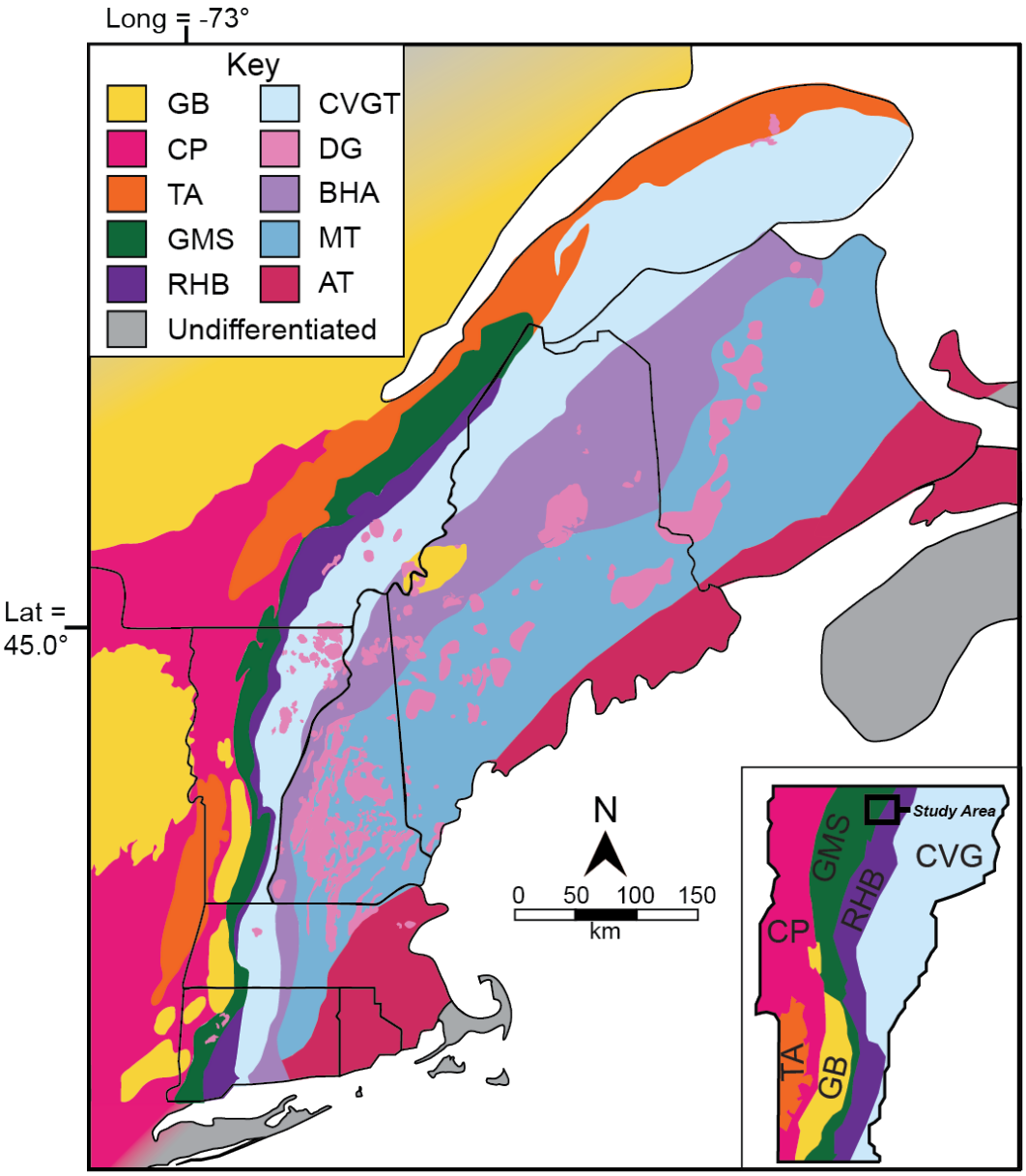

Figure 1-1: Simplified tectonic map of New England and southern Quebec: GB: Grenvillian Basement, CP: Carbonate Platform, TA: Taconic Allochthon, GMS: Green Mountain Slice, RHB: Rowe-Hawley Belt, CVGT: Connecticut Valley Gaspé Trough, BHA: Bronson Hill Anticlinorium, MT- Merrimack Trough, AT-Avalon Terrane, DG-Devonian Granite. Drafted by Lagor (2016) based on compiled bedrock maps of Weeler *et al.* (1996)- Canada; Thériault *et al.* (2012)- Quebec; Mersereau *et al.* (2008)- New Brunswick; Keppie et al. (2000)- Nova Scotia; Osberg *et al.* (1985)- Maine; Lyons *et al.* (1997)- New Hampshire; Zen *et al.* (1983)- Massachusetts; Hermes *et al.* (1994)- Rhode Island; Rodgers (1985)- Connecticut; Fisher *et al.* (1970)- New York; and Ratcliffe *et al.* (2011)- Vermont. Inset shows the generalized map of tectonic belts in Vermont with study area, the region of the TPC, indicated by a black box. CP = Carbonate platform, TA = Taconic allochthon, GB = Grenvillian basement, GMS = Green Mountain Slice, RHB = Rowe-Hawley Belt, CVG = Connecticut Valley-Gaspe Trough. Map is compiled from Doll (1961), Ratcliffe *et al.* (2011), and references therein.

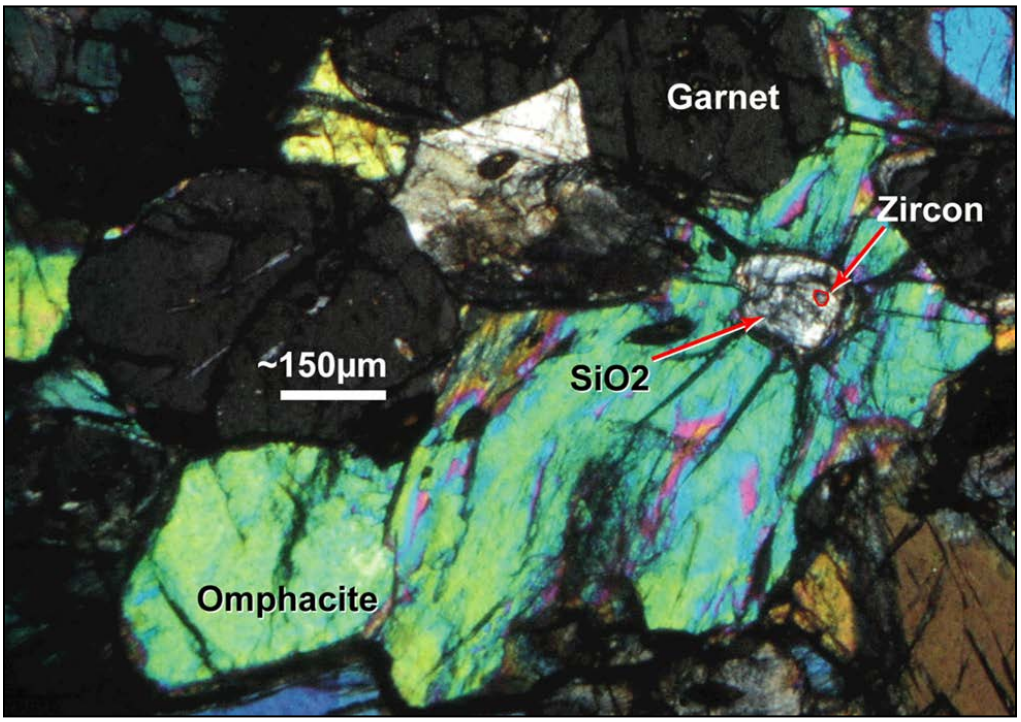

Figure 1-2: Photomicrograph of a sample of UHP eclogite from Papua New Guinea with coesite included within omphacite (image from Baldwin *et al.*, 2008). Radial fractures around SiO_2 inclusions are indicative of UHP metamorphism and are used to distinguish coesite from quartz in eclogite. Fractures form due to an ~ 10% volumetric increase during the transition from coesite to quartz (Wang *et al.*, 1989).

Figure 1-3: Blueschist and eclogite in Eclogite Brook, TPC. a: Asymmetric eclogite boudin, which in this outcrop implies a top-to-the-NW shear direction. b: Eclogite lens in hinge of isoclinal F_1 fold described by Bothner and Laird (1987).

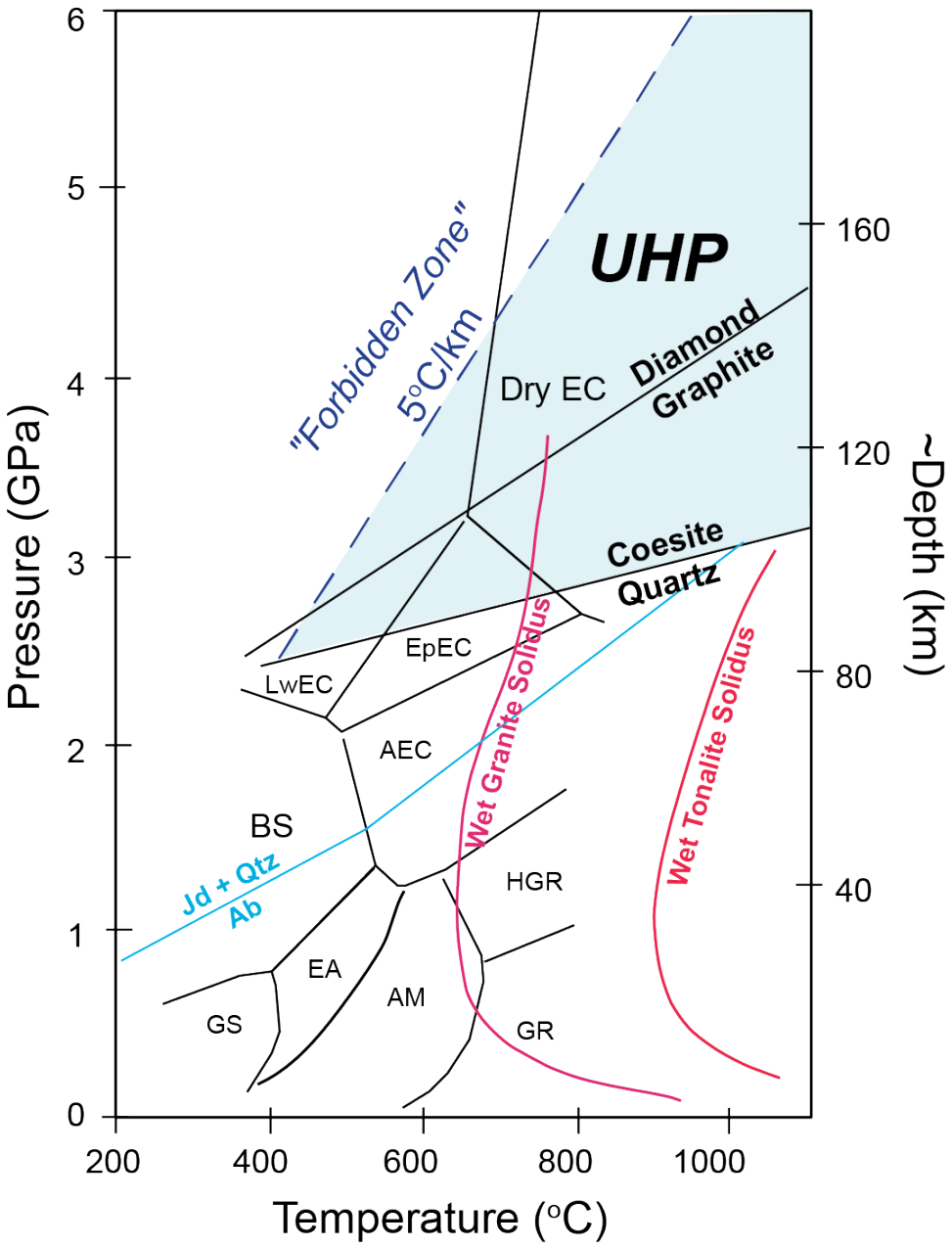

Figure 1-4: Metamorphic facies diagram modified from Ernst (2001) that includes pressure, temperature, and depth. UHP conditions are defined by the quartz–coesite boundary. Abbreviations are as follows: AEC-amphibole-eclogite; AM: amphibolite; BS: blueschist; Dry EC: dry eclogite; EA: epidote-amphibolite; EpEC: epidote-eclogite; GR: granulite; GS: greenschist; HGR: hornblende-granulite LwEC: lawsonite-eclogtite.

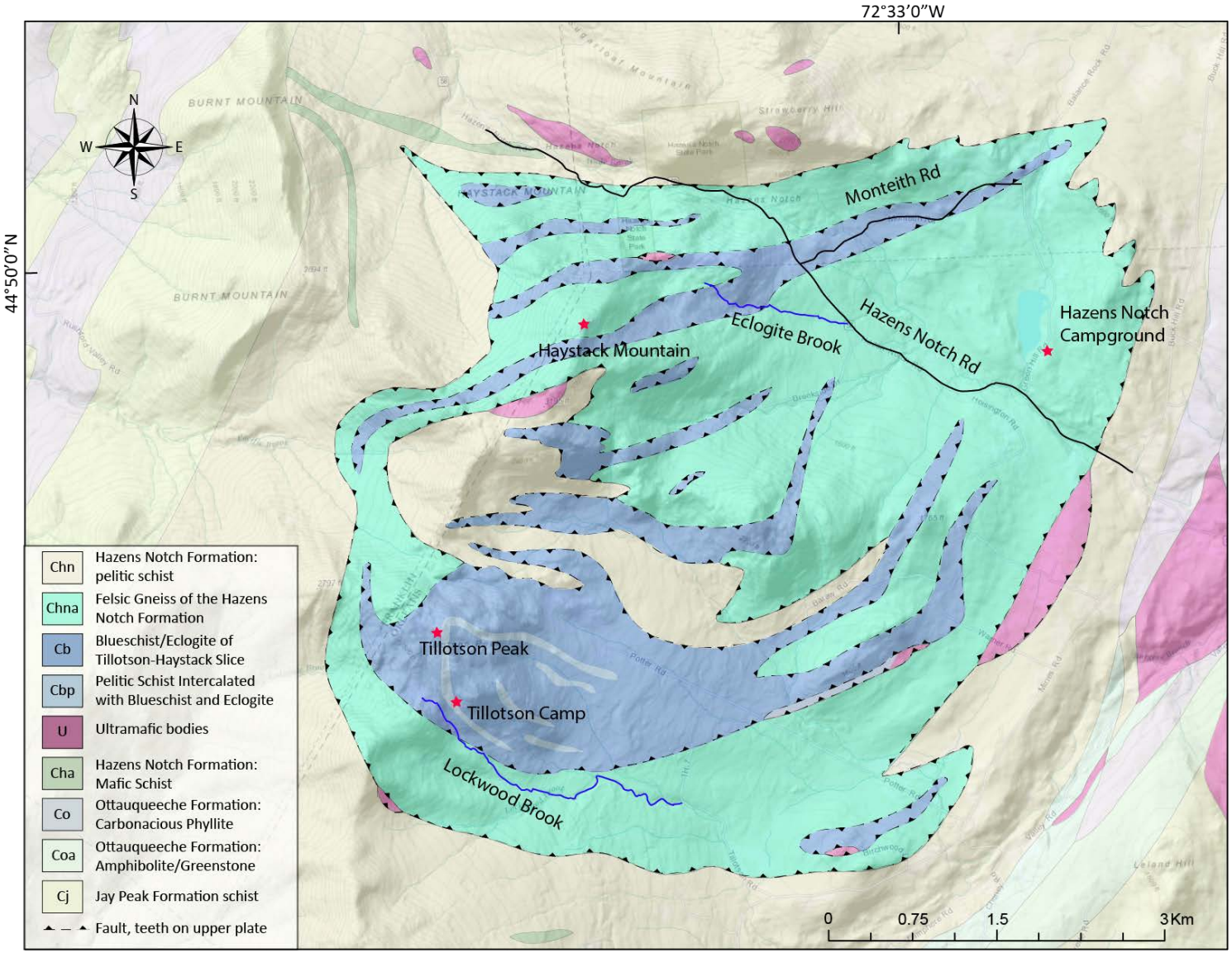
72°33'0"W
44°50'0"N
N
W
E
S
BURNT MOUNTAIN
BURNT MOUNTAIN
HAYSTACK MOUNTAIN
Monteith Rd
Hazens Notch Rd
Eclogite Brook
Haystack Mountain
Hazens Notch Campground
Tillotson Peak
Tillotson Camp
Lockwood Brook
Chn Hazens Notch Formation: pelitic schist
Chna Felsic Gneiss of the Hazens Notch Formation
Cb Blueschist/Eclogite of Tillotson-Haystack Slice
Cbp Pelitic Schist Intercalated with Blueschist and Eclogite
U Ultramafic bodies
Cha Hazens Notch Formation: Mafic Schist
Co Ottauqueeche Formation: Carbonacious Phyllite
Coa Ottauqueeche Formation: Amphibolite/Greenstone
Cj Jay Peak Formation schist
Fault, teeth on upper plate
0
0.75
1.5
3Km

Figure 1-5: Geologic map of the Tillotson peak complex Geologic modified from the bedrock mapping of Bothner and Laird (1999), with mentioned locations from this study and Bothner and Laird (1987).

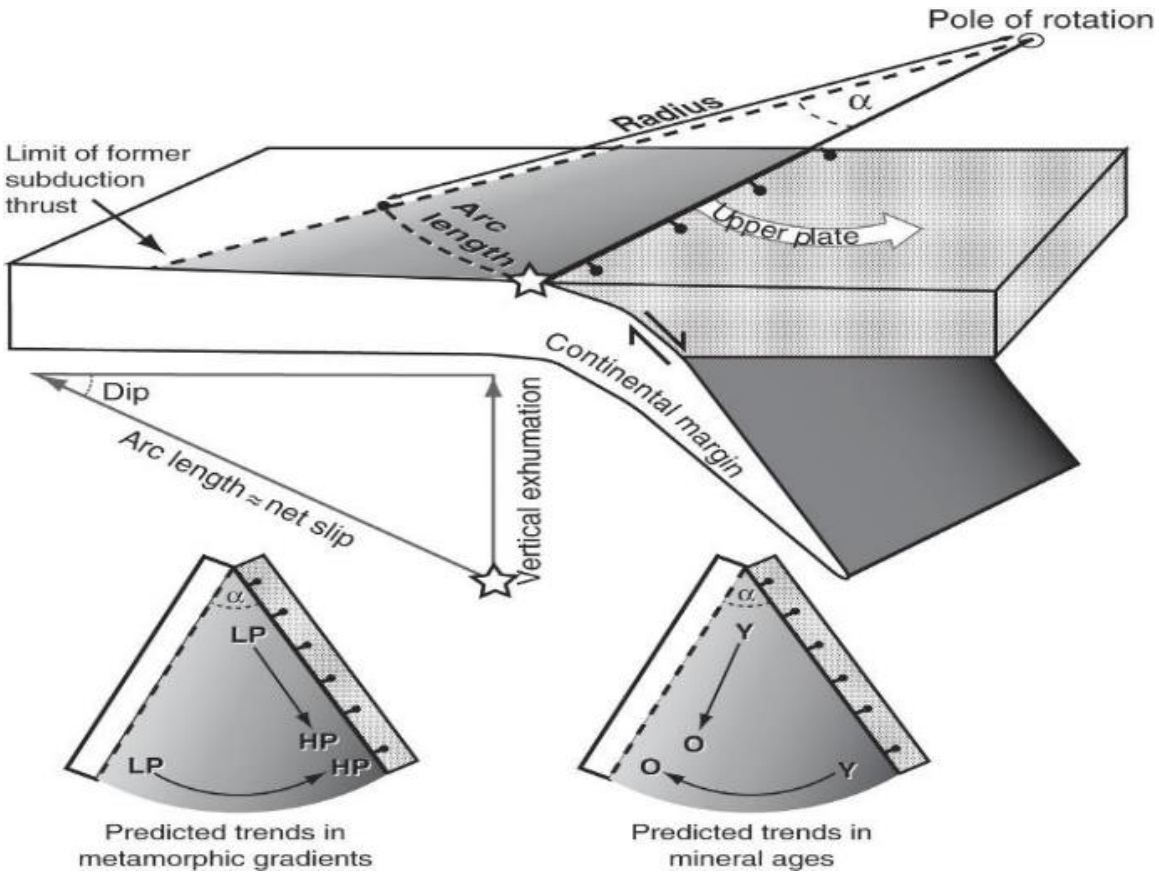

Figure 1-6: Exhumation *via* microplate rotation from Webb *et al.* (2008). As the subducted plate rotates, exhumation is facilitated by a normal-sense shear zone. The predicted trend in metamorphic gradient is high-P to low-P, and the predicted trend in mineral ages is young to older from proximal to the subduction boundary to farther inland.

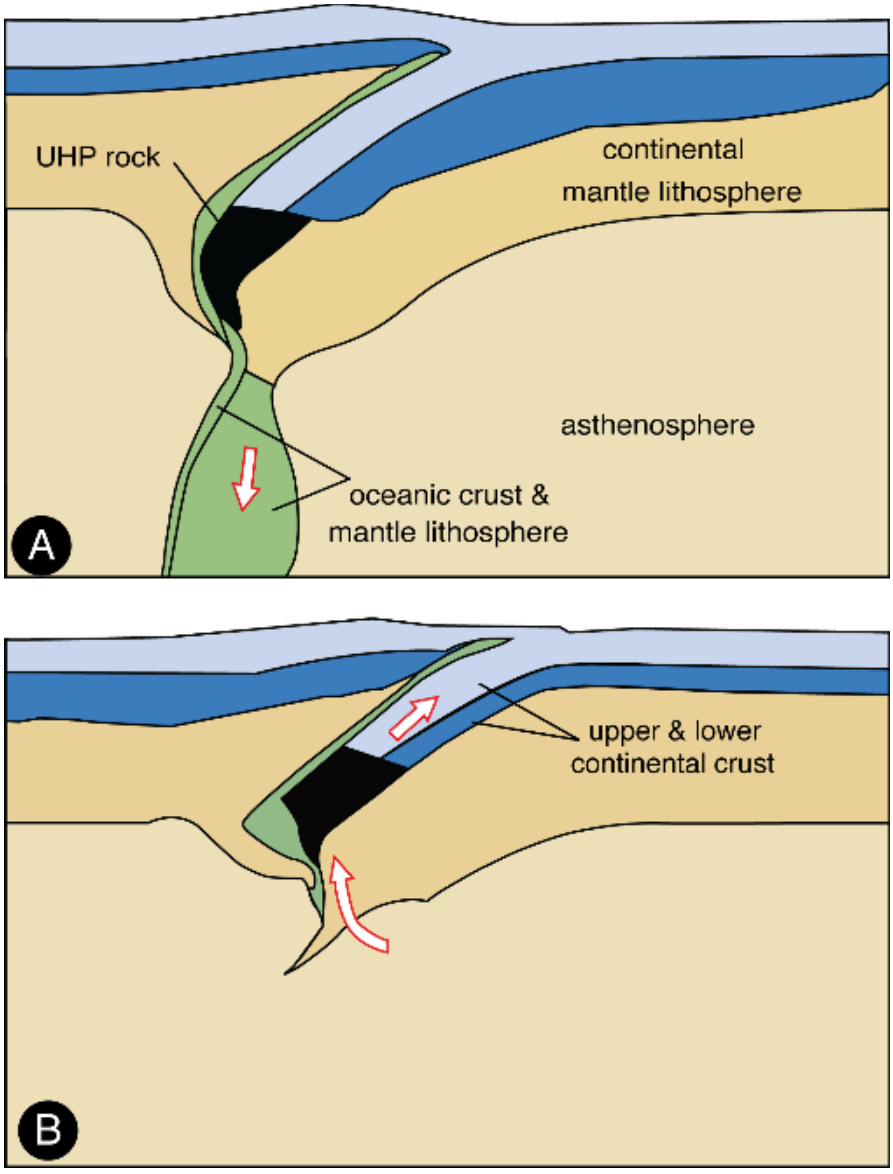

Figure 1-7: Eduction as a means of exhumation from Hacker and Gerya (2013). As subduction continues, slab pull exceeds slab strength, and UHP material is exhumed, relative to the subduction channel.

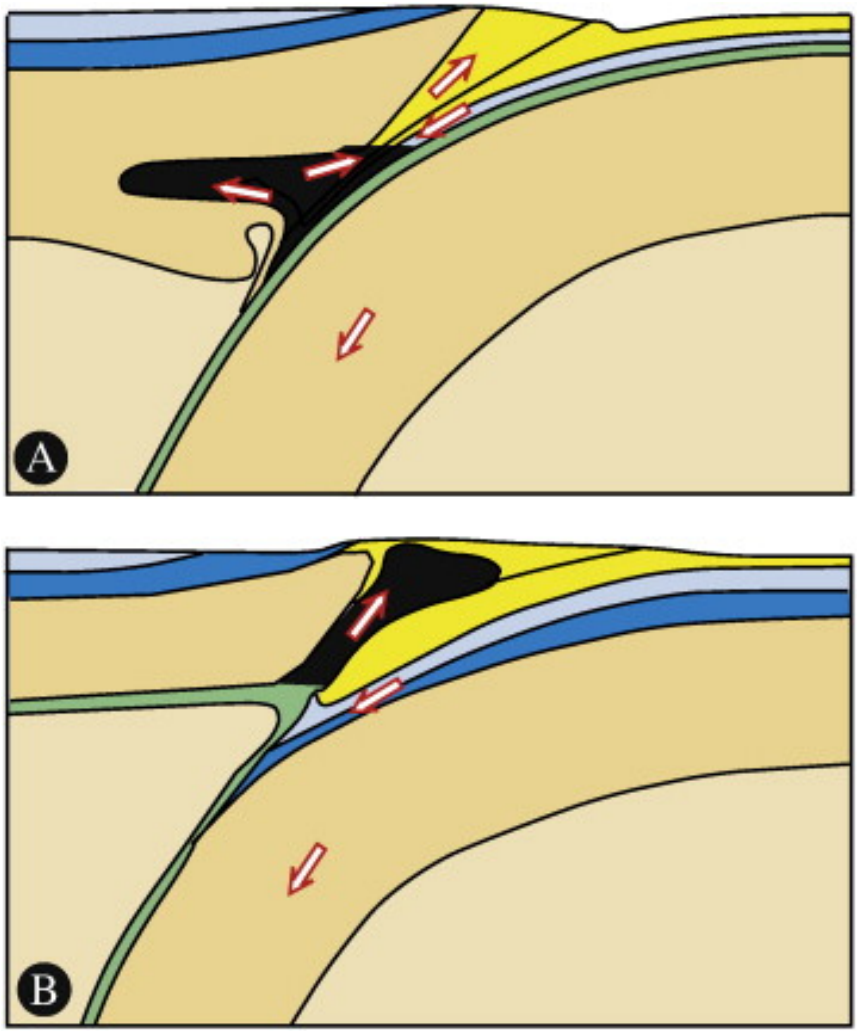

Figure 1-8: Exhumation within a serpentine channel, from Hacker and Gerya (2013). In this proposed model, low viscosity material lubricated the subduction channel and return flow of continued subduction causes exhumation of UHP material (black)**.**

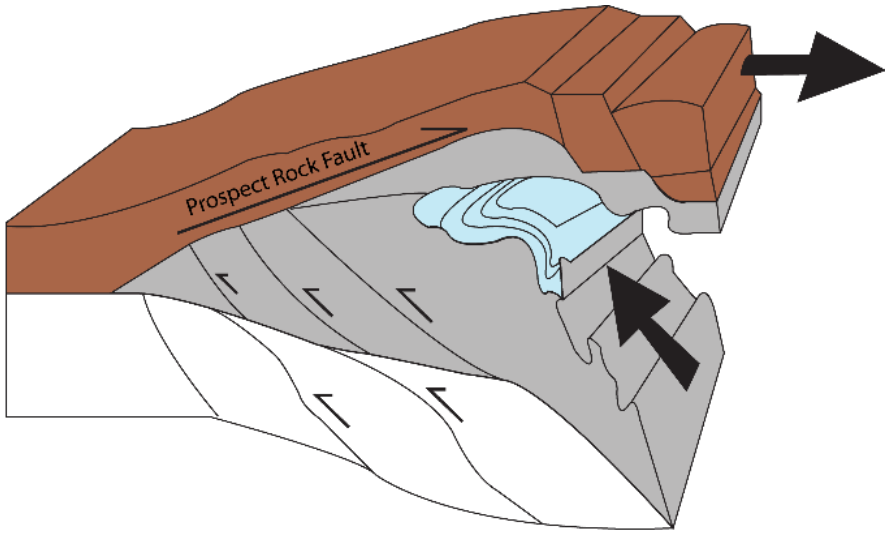

Figure 1-9: Proposed tectonic wedging model from Lamon (2001). In this proposed model, the prospect rock acts as a roof thrust emplacing medium to high-grade metamorphic rock into lower grade units.

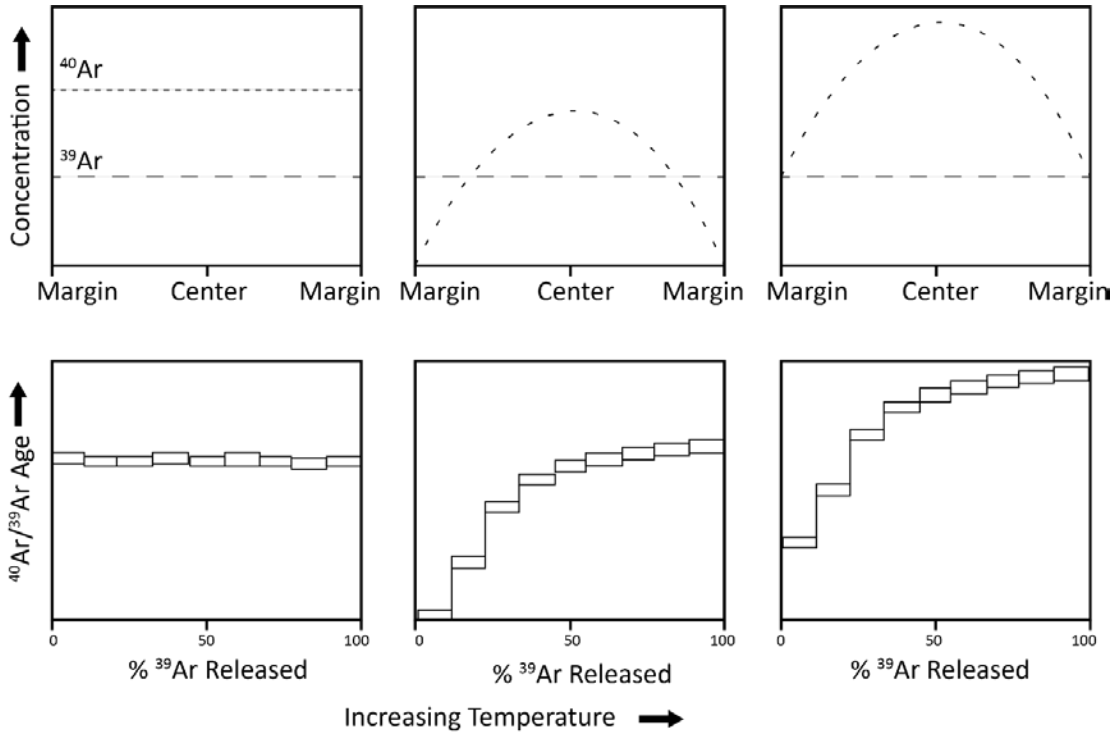

Figure 1-10: Figure from McDougall and Harrison (1999) showing theoretical results from three samples dated with the step-heated $^{40}Ar/^{39}Ar$ method. The top row of diagrams show the concentration of radiogenic ^{40}Ar and ^{39}Ar and the bottom show idealized age spectra for these samples. The left most diagrams represent an idealized crystal that cooled rapidly and was undisturbed after formation. The middle diagrams are of a crystal that lost argon due to reheating during geologically recent time. The far right shows a similar situation, except significant time has passed since the argon loss event. Similar age gradients may result from resetting by deformation as well.

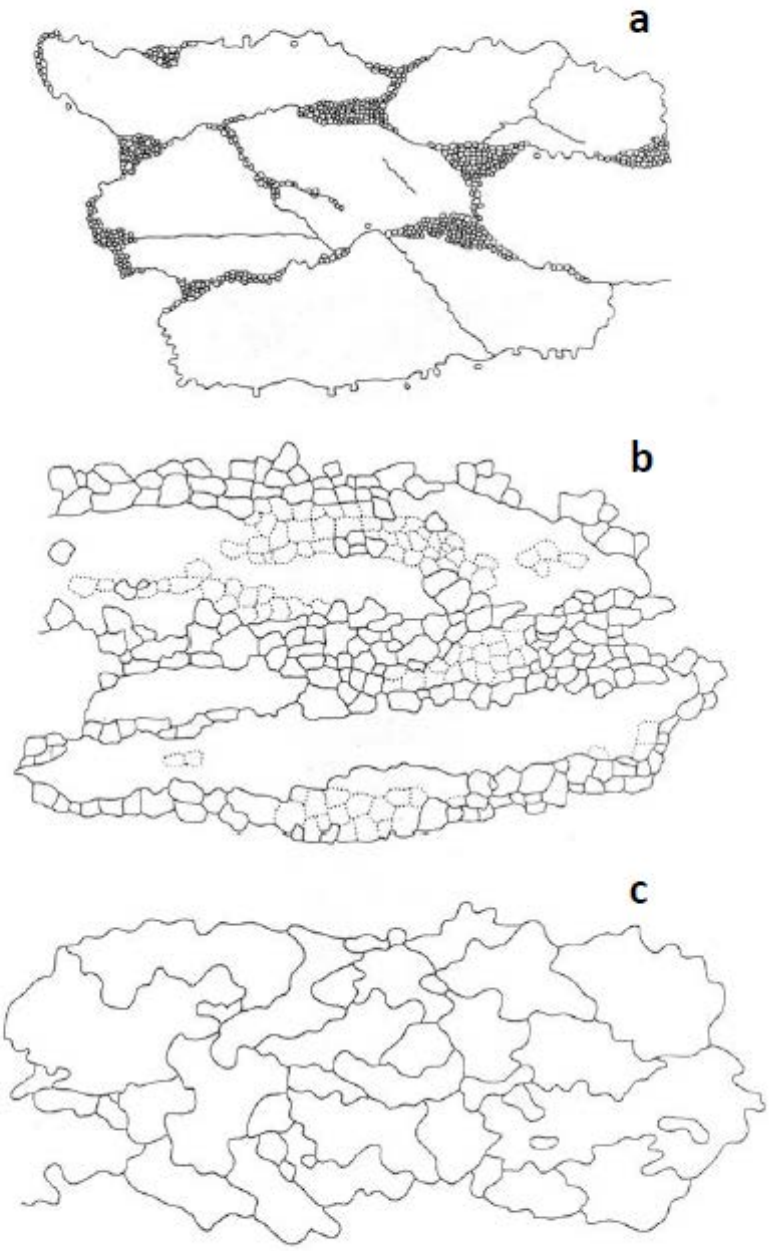

Figure 1-11: Phases of dynamic recrystallization in quartz with increasing temperature from Stipp *et al.* (2002). A) Bulging recrystallization occurs at low-T (300–400°C), with subgrains at the boundaries of quartz grains. B) Subgrain rotation recrystallization occurs at intermediate temperatures (400–500°C), and form oblique to the foliation. C) Grain boundary migration forms at high-T (500–700°C) and results in amoeboid, lobate shaped grain boundaries.

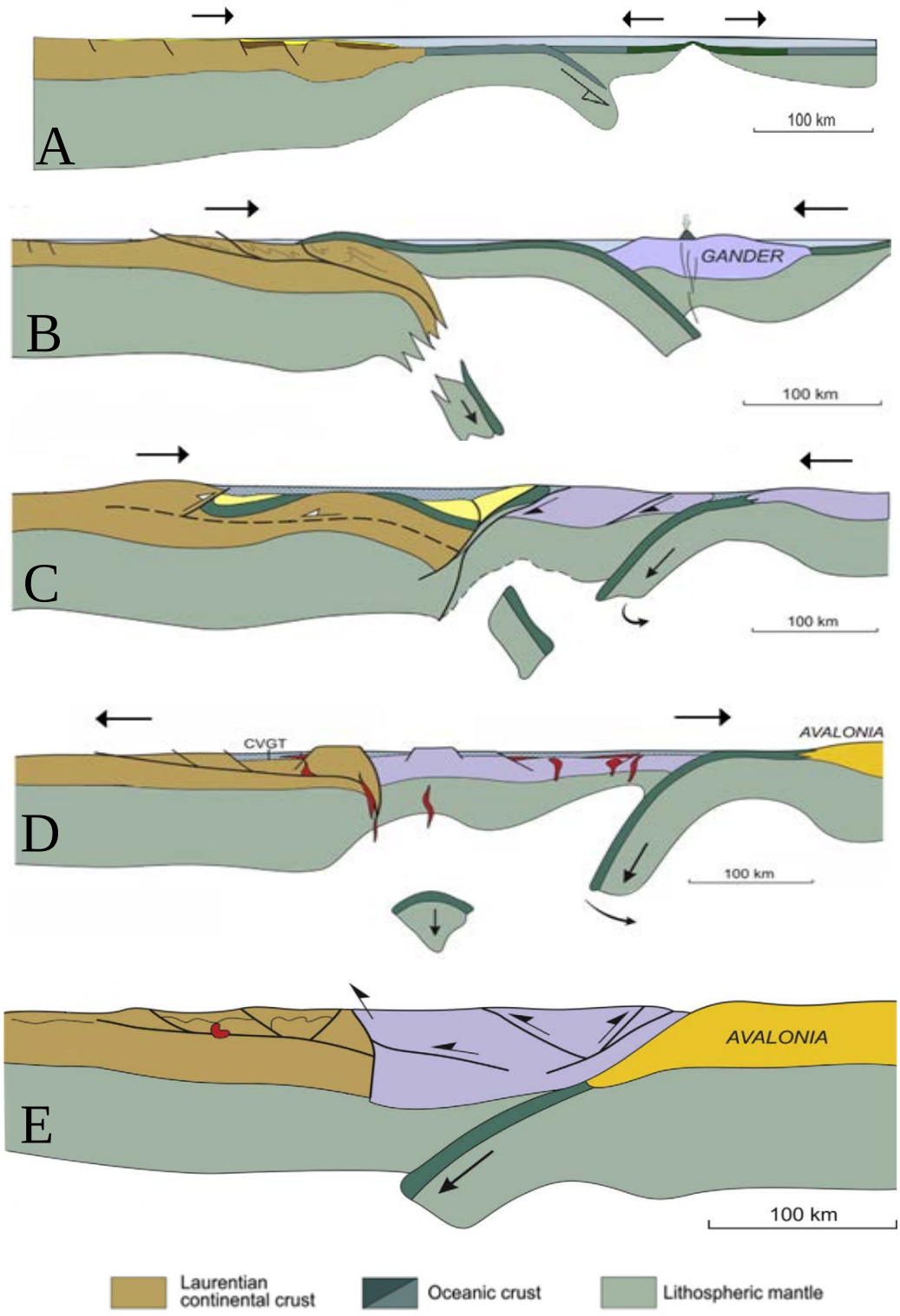
A
100 km
B
GANDER
100 km
C
100 km
D
CVGT
AVALONIA
100 km
E
AVALONIA
100 km
Laurentian continental crust
Oceanic crust
Lithospheric mantle

Figure 1-12: Schematic diagram that shows the Tectonic evolution of the Laurentian margin from the late Cambrian to the Devonian from Tremblay and Pinet (2016). A) 500–470 Ma: as sea floor spreading occurs to the east (relative to present coordinates) of Laurentia, subduction of Laurentian oceanic crust begins. B) 470–450: Onset of Taconic Orogeny as a result of the collision of peri-Laurentian arc-environments with the Laurentian margin. C) 450–425 Ma: Compressional phase of the Salinic Orogeny associated with the collision of Gander and Laurentia. D) 425–410 Ma: Extensional phase of the Salinic Orogeny caused by upwelling of asthenosphere above a westward dipping (relative to present coordinates) subduction zone resulting in the formation of the Connecticut Valley Gaspé Trough. E) 390–370 Ma: Culmination of the Acadian Orogeny as a result of the collision of Avalonia with the Composite Laurentian Margin.

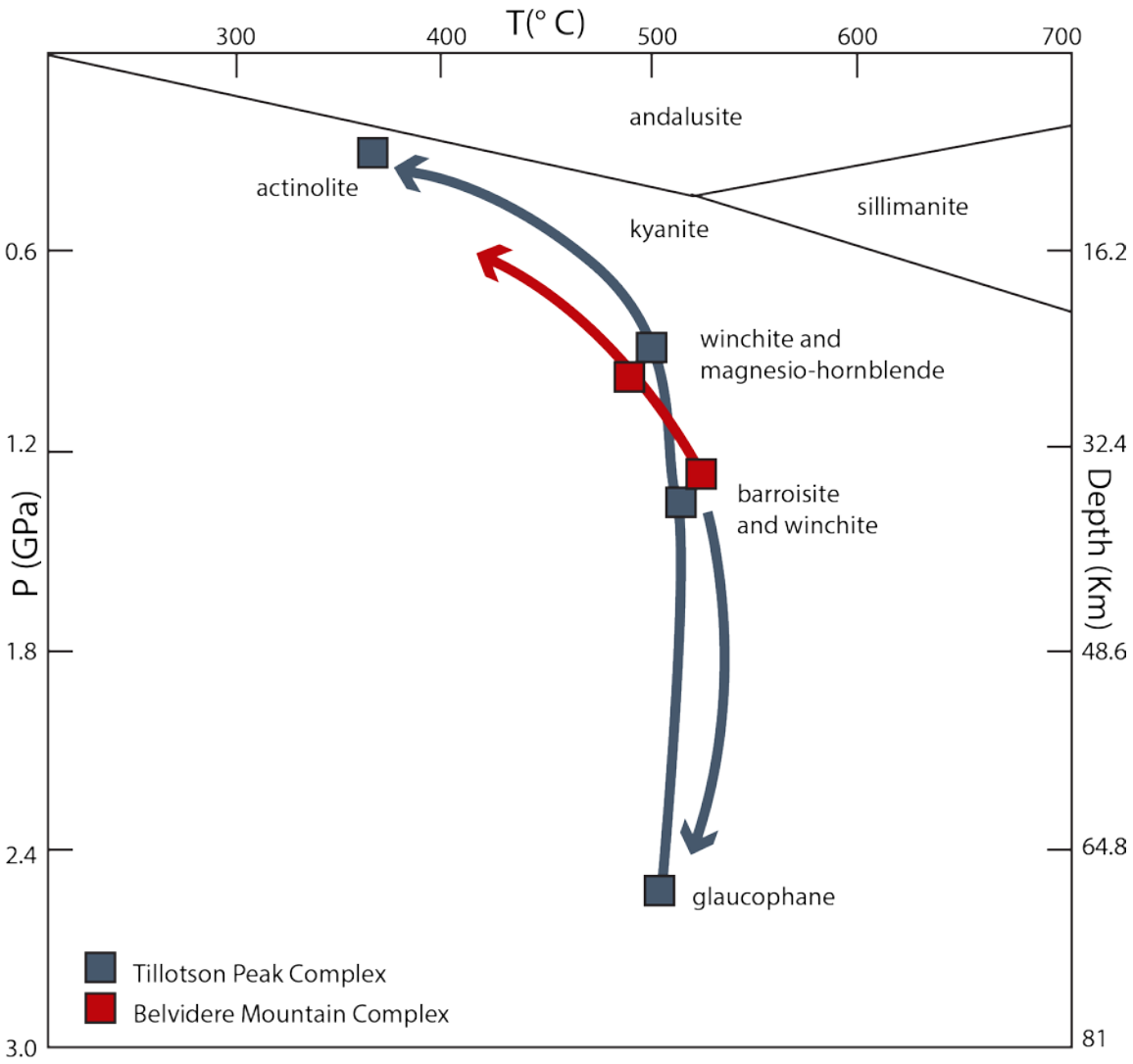

Figure 1-13: P-T-D diagram calculated from petrologic modelling of rocks of the TPC and Belvidere Mountain Complex from Honsberger (2015). The TPC (blue) is interpreted to reach peak conditions approaching UHP (2.5 GPa, 500°C) metamorphism at 468 ± 6.4 Ma (Laird *et al*., 1984), with actinolite related to greenschist-facies metamorphism crystallizing in the Acadian (Laird and Albee 1981, Laird *et al.*, 1993). The Belvidere Mountain Complex (red) is interpreted to barroisite–winchite conditions at 505–486 Ma (Laird *et al.*, 1984, 1993; Castonguay *et al.*, 2012).

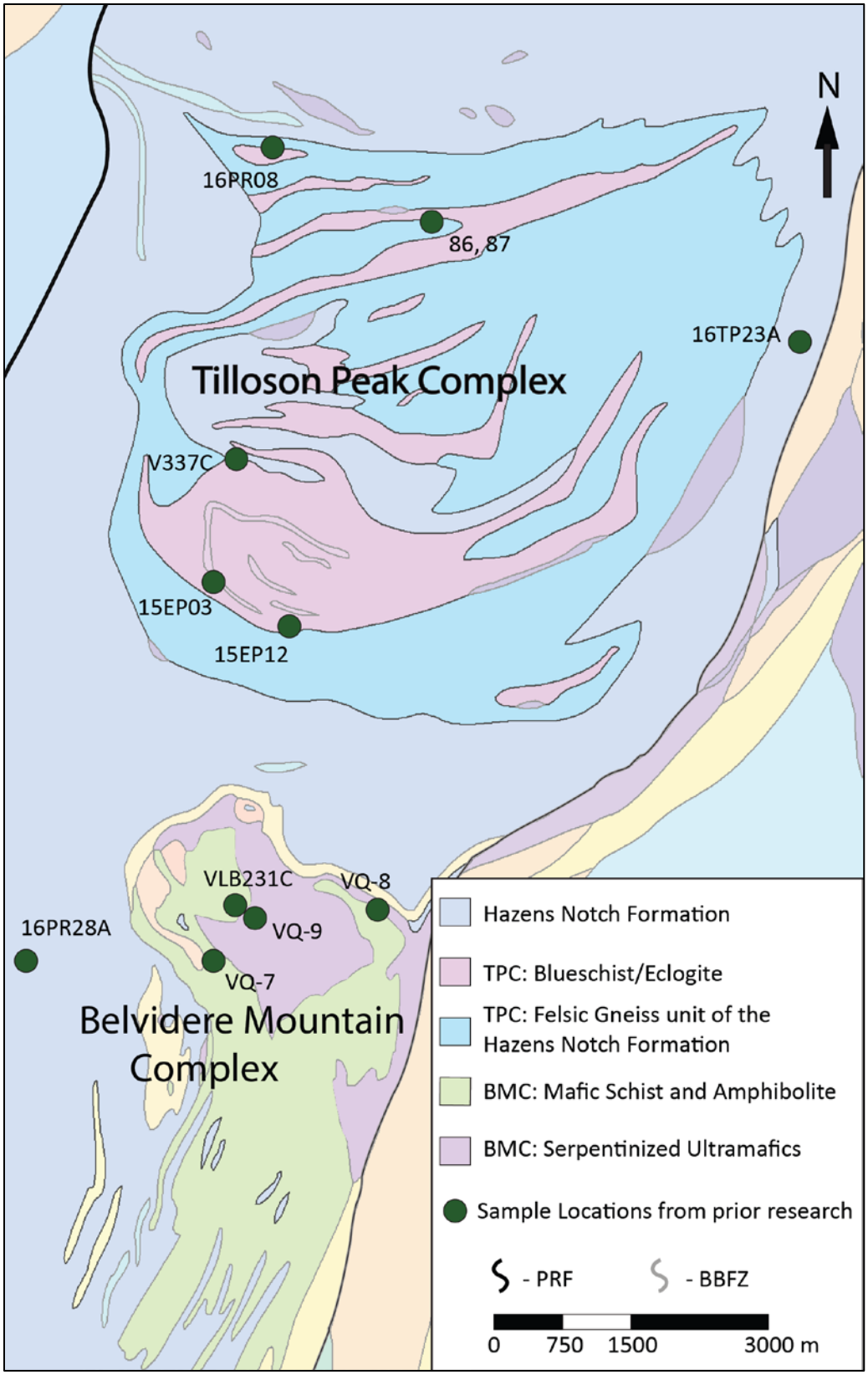
N
16PR08
86, 87
16TP23A
Tilloson Peak Complex
V337C
15EP03
15EP12
VLB231C
VQ-8
16PR28A
VQ-9
VQ-7
Belvidere Mountain Complex
Hazens Notch Formation
TPC: Blueschist/Eclogite
TPC: Felsic Gneiss unit of the Hazens Notch Formation
BMC: Mafic Schist and Amphibolite
BMC: Serpentinized Ultramafics
Sample Locations from prior research
- PRF
- BBFZ
0
750
1500
3000 m

Figure 1-14: Geologic map of the Belvidere Mountain Complex and Tillotson Peak Complex modified from Bothner and Laird (1999) and Ratcliffe *et al.* (2011) with sample sites from prior research. Abbreviations are as follows: TPC- Tillotson Peak Complex, BMC- Belvidere Mountain Complex, PRF- Prospect Rock Fault, BBFZ- Burgess Branch Fault Zone. 16PR08: Two aliquots of white mica from felsic gneiss yield plateau ages of 458–456 Ma (Figure 1-15; Tam *et al.,* 2018). 86, 87: Total Fusion ages of white mica from retrogressed blueschist give a range of 480–468 Ma (Gonzalez *et al.,* 2018). 16TP23A: Plateau ages of two aliquots of white mica from Hazens Notch Schist record a range of 451–447 (Figure 1-15; Tam *et al*., 2018). V337C: Total fusion age on glaucophane from blueschist of 468 ± 6.4 Ma (Laird *et al.,* 1984). 15EP03: White mica plateau age of 462.4 ± 1.4 Ma (1σ) on glaucophane-bearing schist (Figure 1-15; Pidgeon, 2017). 15EP12: White mica plateau age of 466.6 ± 1.5 Ma (1σ) on felsic gneiss (Figure 1-15; Pidgeon, 2017). VLB231C: Plateau age on barroisite of 505 ± 2 Ma (Figure 1-15; Laird *et al.,* 1993). VQ-8: Plateau age of 414.7 ± 2.4 Ma from white mica in the Hazens Notch Formation (Castonguay *et al.,* 2012). VQ-9: weighted mean age of 486 ± 31 Ma for amphibole from the Belvidere Mountain Amphibolite (Castonguay *et al.,* 2012). 16PR28A: Plateau age of 447.8 ± 2.1 Ma (1σ) from white mica of the Hazens Notch Formation (Tam *et al.,* 2018). VQ-7: Disturbed $^{40}Ar/^{39}Ar$ spectra yield inverse isochron ages of 426 ± 11 Ma and 474.7 ± 3.2 Ma (Castonguay *et al.,* 2012).

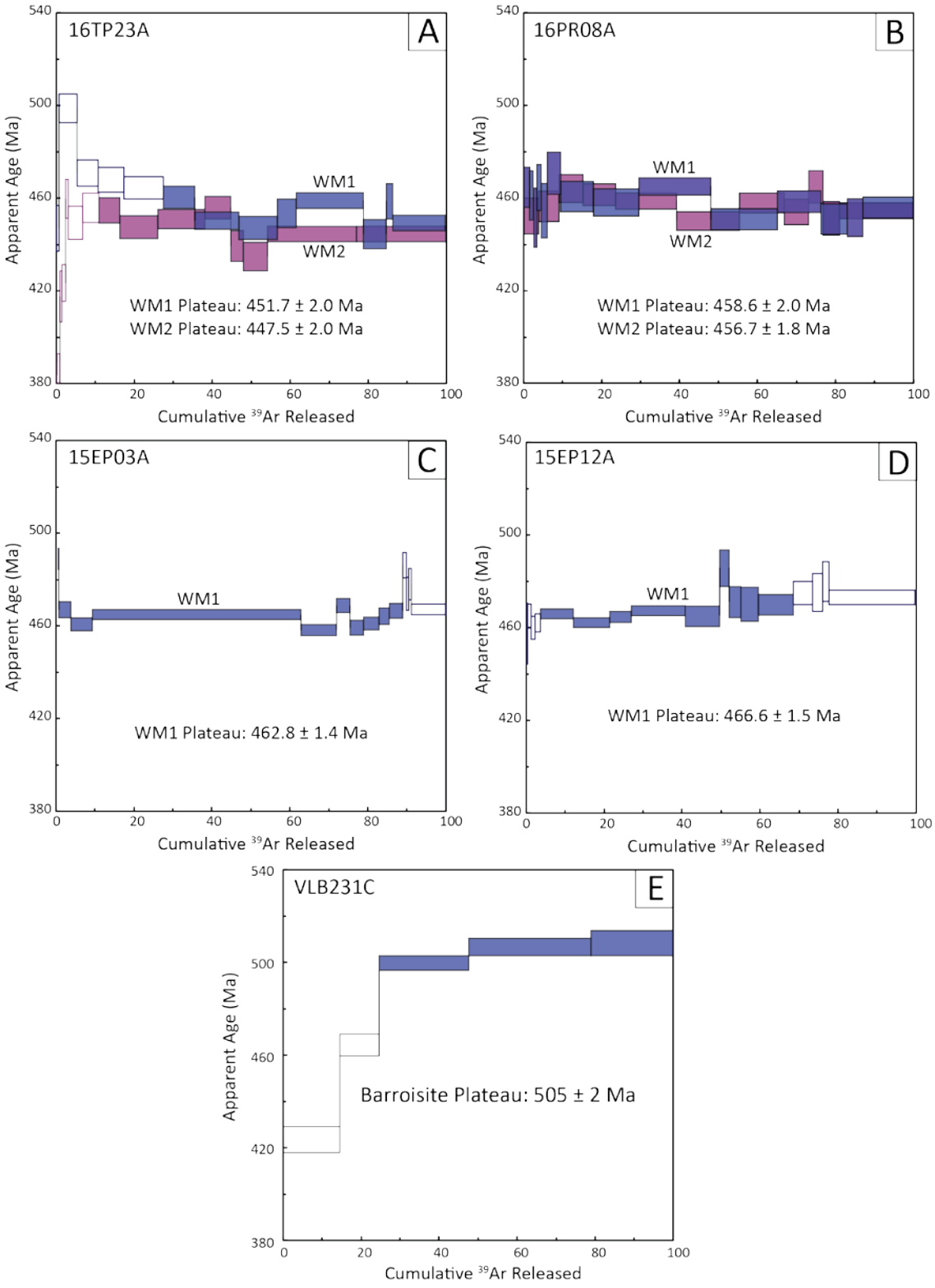
16TP23A
A
WM1
WM2
WM1 Plateau: 451.7 ± 2.0 Ma
WM2 Plateau: 447.5 ± 2.0 Ma
16PR08A
B
WM1
WM2
WM1 Plateau: 458.6 ± 2.0 Ma
WM2 Plateau: 456.7 ± 1.8 Ma
15EP03A
C
WM1
WM1 Plateau: 462.8 ± 1.4 Ma
15EP12A
D
WM1
WM1 Plateau: 466.6 ± 1.5 Ma
VLB231C
E
Barroisite Plateau: 505 ± 2 Ma
Apparent Age (Ma)
Cumulative ^{39}Ar Released

Figure 1-15: Argon age spectra from previous and recent research in and proximal to the TPC. A) Two separate aliquots of white mica from a sample of Hazens Notch Formation on the boundary of the TPC (Figure 1-14) yield plateau ages of 451–447 Ma (Tam *et al.*, 2018). B) Two aliquots of white mica from felsic gneiss in the TPC (1-15) have plateau ages of 458.6–456.7 Ma (Tam *et al.*, 2018). C) A single aliquot of white mica from glaucophane-bearing schist in the TPC (1-15) has a plateau age of 463.8 ± 1.4 Ma (Pidgeon, 2017). D) White mica dated from a sample of pelitic schist in the TPC (1-15) records a plateau age of 466.6 ± 1.5 Ma (Pidgeon, 2017) Barroisite from the Belvidere Mountain Amphibolite yields the oldest plateau age of Taconian metamorphism in Vermont at 505 ± 2 Ma (Laird *et al*., 1993).

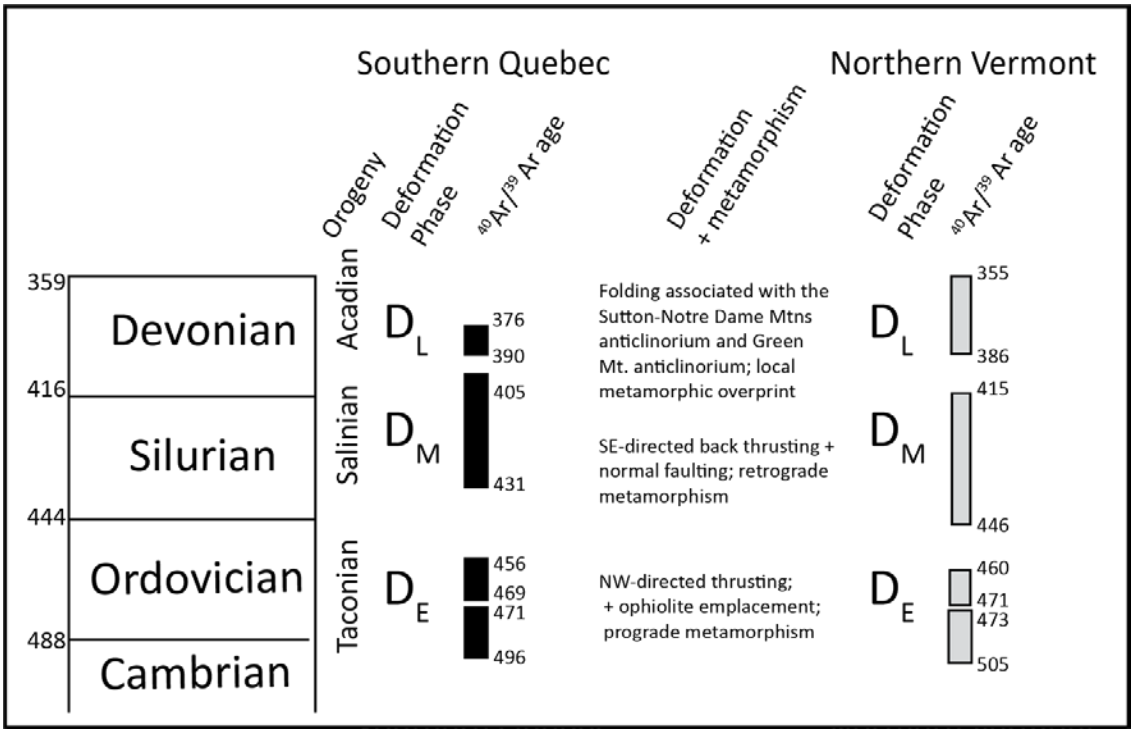

Figure 1-16: Summary of Taconic, Salinic, and Acadian metamorphism and deformation in Vermont and Southern Quebec, modified from Castonguay *et al.* (2012). D_E, D_M, D_L represent the early, middle, and late phase of deformation of late Cambrian to Devonian-aged rocks of the region.

CHAPTER 2: METHODS

2.1 Introduction

To address the goals outlined by this project, data were collected from outcrops of felsic gneiss, blueschist, ultramafics, and pelitic schist within the TPC. At each of these locations, observations included the documentation of shear zones, foliations, lineations, fold geometry, and relative age relationships. Additional information determined at each location included observations of lithological changes and apparent kinematic indicators. Locations for study were determined using the outcrop descriptions and structural mapping from previous research by Laird and Albee (1981); Laird *et al*. (1993); and Bothner and Laird (1987, 1999). Oriented samples, cut normal to the dominant foliation and 1) relative to the plunge of the dominant lineation (X-Z) and/or 2) perpendicular to lineation plunge direction (Y-Z), were collected from each of the main lithologies within the TPC to understand the timing of metamorphism and deformation as well as to examine the petrologic relationship of mafic and felsic rocks. Apparent kinematic indicators in the field, such as asymmetric amphibolite and eclogite boudins (Figure 1-3) and quartz sigma clasts in felsic gneiss, are used as apparent shear sense indicators and have been integrated with observations made during thin section analysis.

2.2 Microstructural Analysis:

Data that was obtained during this research was done so to correlate with previous and ongoing research to further understand the P-T-t-D history of the TPC. Orthogonal thin sections were cut parallel and perpendicular (X-Z and Y-Z axes of finite strain

ellipse, respectively) to the plunge of mineral stretching lineations and perpendicular to the dominant foliation. In the absence of mineral lineation, samples are cut orthogonally relative to the dip direction of the dominant foliation. Select samples have been analyzed *via* X-Ray diffractometry (XRD) and energy dispersive X-Ray spectroscopy (EDS) to confirm mineralogy observed in thin section.

Structural elements (folding, foliations, and kinematic indicators) observed in thin section are described in terms of generation and have been integrated with observations of similar structures in the field based on the relative timing of development. Samples with distinct foliations were selected for further geochronologic study to investigate the timing of deformation. Samples with microstructures in quartz and carbonate have been examined to determine whether grain recrystallization occurred statically or as a response to deformation. The timing of porphyroblast growth relative to foliation development was analyzed in samples, and those with asymmetry were examined to determine the shear sense. Core to rim zoning in mineral phases was documented to analyze the timing of mineral growth. In addition, accessory phases, such as titanite and rutile, were noted as potential targets for U-Pb dating.

2.3 Compositional Analysis of K-rich and High-Pressure Phases

To confirm observations made in thin section and to greater understand the P-T conditions under which these rocks formed, polished thin sections from selected samples were examined with the use of the Scanning Electron Microscope at Middlebury College in Middlebury, Vermont. Back Scatter Electron (BSE) images were collected and spot spectra were analyzed using an energy dispersive X-Ray spectroscopy (EDS) detector to

determine the compositions of minerals that define metamorphic foliations, and to examine compositional differences in mineral grains that have core to rim zoning. In addition, inclusions in minerals were examined for the occurrence of high-pressure indicator minerals. Omphacite and paragonite inclusions were identified in garnet porphyroblasts within blueschist samples. Representative oxide compositions for selected minerals determined from the SEM are included in Appendix B.

2.4 $^{40}Ar/^{39}Ar$ Dating of Actinolite, Glaucophane, Tourmaline, and White Mica

Targeted potassium-bearing minerals for further study were selected *via* observation under petrographic microscope, and included actinolite, glaucophane, tourmaline, and white mica. Ideal candidates for $^{40}Ar/^{39}Ar$ geochronology have little to no inclusions of other minerals and minimum alteration (chloritization, etc.). Mineral separates were handpicked from the 125–500 μm fractions of crushed rock samples to analyze native grain size. Grains from each sample were loaded into aluminum foil packets, arranged in suprasil vial, and placed in an aluminum canister (25 mm x 140 mm) for irradiation. Samples were irradiated with aliquots of Fish Canyon Tuff Sanidine with an age of 28.03 Ma (Renne *et al.*, 1998) to act as an apparent flux monitor to monitor the neutron dose. CaF_2 and KSO_4 were also irradiated to determine corrections for interfering nuclear reactions. Samples were irradiated for fourteen hours at the Cadmium-Lined In-Core Irradiation Tube (CLICIT) in the TRIGA reactor at Oregon State University.

$^{40}Ar/^{39}Ar$ step-heated analysis was conducted in the noble gas laboratory located in the Geology department at the University of Vermont. White mica grains were loaded

into degassed Nb foil packets before being loaded into 1.5 mm wells in a copper planchet. Depending on grain size, white mica was analyzed in aliquots of one to two grains per well. Actinolite, glaucophane, and tourmaline were loaded directly into 1.5mm wells in a copper planchet before being loaded into the mass spectrometer. Tourmaline grains were analyzed in aliquots of all grains picked from the sample, while amphiboles were analyzed in single-grain analyses.

Argon isotopes were analyzed on a noble gas mass spectrometer during step-heated analyses of single grains, when possible, or multigrain aliquots. Data from samples and flux monitors were corrected for blanks, mass discrimination, atmospheric argon, neutron-induced interfering isotopes, and the decay of ^{37}Ar and ^{39}Ar.

Mass discrimination was calculated by analyzing known aliquots of atmospheric argon for which $^{40}Ar/^{36}Ar$ measured in the range of 296.8 ± 0.35% – 307.8 ± 0.56%, and an assumed atmospheric value of 298.56 (Lee *et al.*, 2006). Interfering nuclear reactions were corrected for by analyzing argon extracted from irradiated and fused optical grade CaF_2 and KSO_4. The correction factors used to account for interfering nuclear reactions for the irradiated samples are: $[^{40}Ar/^{39}Ar]$ K = 5.4 x 10^{-4} ± 1.4 x 10^{-4} (Jicha & Brown, 2014), $[^{36}Ar/^{37}Ar]$ Ca = 2.65 x 10^{-4} ± 2.2 x 10^{-5} (Renne *et al.*, 2013), and $[^{39}Ar/^{37}Ar]$ Ca = 6.95 x 10^{-4} ± 8.96 x 10^{-6} (Renne *et al.*, 2013). To calculate J factors for samples, linear interpolation was based on sample position between flux monitor packets in the irradiation tube. Ages were calculated using the isotopic decay constants from Steiger and Jager (1977). Inverse isochron and apparent age data were calculated using an in-house data reduction program and Isoplot 3.0 (Ludwig, 2003). Plateau ages are reported

if sufficient criteria are met (McDougall and Harrison, 1999), and weighted mean ages, apparent minimum ages, and total gas integrated ages are reported. Errors associated with plateaus, apparent minimum ages, weighted mean ages, and integrated ages are quoted at the 1σ level.

2.5 U-Pb Geochronology

Titanite was examined as an accessory phase in samples of blueschist and pelitic schist. A thin section from each; a sample of pelitic schist (16TP03A) and blueschist (16TP08B) were sent to be analyzed by Dr. Andrew Kylander-Clark at the LA-ICP-MS laboratory in the Earth Sciences department at the University of California Santa Barbara. Results are plotted on a Terra-Wasserburg plot. For methodology of U-Pb dating of accessory phases, see Kylander-Clark *et al*. (2008).

CHAPTER 3: RESULTS

3.1 Introduction

Due to the reliance of this study on microstructural observations and associating those to key structures in the field to define the timing of distinct deformation events, we interpret an additional earlier foliation generation than previously discussed. This includes the previous mapping of Bothner and Laird (1999) that documents the bulk of structures, lithologies, and outcrops in the field area (Figure 3-1). Individual structures within hand samples and thin sections are described in terms of local foliation generation (S_n) and are correlated to foliation generation of the field area ($S_{\#}$) in table 3-1 and 3-2. A summary of petrographic observations and $^{40}Ar/^{39}Ar$ age data from samples mentioned in this section is included in table 3-3 and 3-4, respectively. $^{40}Ar/^{39}Ar$ age data presented in this research are given with 1σ error.

S_1 is variably preserved throughout the field area. Frequently, S_1 is preserved as inclusion trails in garnet porphyroblasts in metapelites and blueschist (Figure 3-2). In high-pressure samples, these inclusion trails are defined by glaucophane, omphacite, paragonite, and titanite. S_1 is also locally preserved in pelitic samples in quartz-rich microlithons oblique to the dominant foliation (Figure 3-2). F_1 is not observed directly in our study, but (if present) would have been transposed parallel to F_2, evidenced by earlier foliation than previously noted.

The dominant foliation surface in the TPC is S_2, which is axial planar to intrafolial isoclinal F_2 folds (Figure 3-2H,O, 3-3). F_2 folds rarely have three-dimensional exposure, however one rootless fold of eclogite within felsic gneiss (Figure 1-3) has fold

hinge that plunges steeply to the east. The strike and dip of S_2 foliation is variable due to folding following formation (Figure 4-4). L_2 stretching lineations trend approximately E–W, and are frequently defined on S_2 surfaces by elongate mica and amphibole. Kinematic indicators such as shear bands, rotated porphyroblasts, and boudinage structures related to S_2 are examined in the field and in thin section (Figure 1-3, 3-2).

S_3 in the TPC is preserved as an E–W striking spaced crenulation cleavage that is axial planar to F_3 folds. F_3 folds are upright-lightly reclined open features with axes that trend E–W (Figure 3-3, 3-4). These folds define the crab-like map pattern described by previous research (Figure 3-1; Cady *et al.*, 1963; Bothner and Laird, 1987). F_3 folds are observed at the outcrop scale, and the related S_3 crenulation is the dominant D_3 structure observed in thin section (Figure 3-2).

S_4 foliation is a N–S striking spaced crenulate cleavage that is locally preserved in hand sample and outcrop, and is not captured in thin section during this study. S_4 crenulation is axial planar to the interpreted F_4 folding about the NW-trending Gilmore Antiform. The presence of which was confirmed in prior research (Bothner and Laird, 1987) by the observation of F_3 fold axes from Lockwood Brook to Eclogite Brook (Figure 3-4).

3.2 16TP03A

Thin Section Observations

Sample 16TP03A is a green to gray felsic gneiss taken from an outcrop near the top of Eclogite Brook (Figure 3-1), in the northern section of the TPC. In hand sample and outcrop, S_n and S_{n-1} foliation are observed, and an L_{n-1} stretching lineation is defined

by elongate, fine-grained chlorite and white mica. S_n foliation is a spaced foliation defined by fine-grained cleavage domains (Figure 3-2A). S_{n-1} is a spaced foliation that is primarily defined by white mica and quartz, with lesser amounts of chlorite, epidote, opaques, garnet, tourmaline, and accessory minerals, which is crenulated by S_n.

Tourmaline grains are interpreted to have grown prior to D_2, as they have inclusions and core to rim structures (Figure 3-5A) apparent in BSE images. Microstructures preserved in quartz include dominantly lobate grain shapes as well as evidence for subgrain rotation recrystallization, deformation lamellae, and bulging recrystallization.

$^{40}Ar/^{39}Ar$ Geochronology

Two aliquots of white mica from sample 16TP03A were analyzed. The first white mica analysis resulted in a plateau age of 458.9 ± 2.4 Ma, with 79.5% of the ^{39}Ar included (Figure 3-6). The second aliquot resulted in a complex spectra that gave an integrated age of 460.3 ± 7.4 Ma. Both spectra had low-temperature initial steps with Silurian minimum apparent ages as well as in disturbed higher temperature steps of the second aliqout. The minimum apparent ages for the first and second analyses are 445.3 ± 8.2 Ma and 435.2 ± 5.5 Ma, respectively.

A single aliquot of tourmaline from 16TP03A was analyzed (Figure 3-7A). The apparent age spectra shows a gradient from anomalously old ages at the lowest temperature steps to a Carboniferous minimum age with increasing temperatures of extraction.

3.3 16TP04B

Thin Section Observations

Sample 16TP04B is a sample taken from the mapped blueschist unit from an outcrop located on an abandoned logging road directly adjacent to Eclogite Brook (Figure 3-1). In hand sample and outcrop, 0.5–1 mm garnet porphyroblasts are apparent, as well as an ENE-trending L_n stretching lineation defined by fine grains of white mica and chlorite.

The dominant penetrative fabric in hand sample and thin section is S_n, which is defined by fine-grained (0.01–0.2 mm) white mica, opaques, chlorite, and epidote. Garnet porphyroblasts in this thin section are partially to fully pseudomorphed by chlorite (Figure 3-2b). S_{n-1} is locally defined by inclusions within these porphyroblasts. Garnet sigma clast tails composed of chlorite, quartz, and epidote are consistent with top-to-the-NE, shear sense with a normal component. Quartz grains, apparent only locally in sigma clast tails on garnets, show dominantly amoeboid grain shapes as well as evidence for subgrain rotation recrystallization.

^{40}Ar/^{39}Ar Geochronology

Step-heating of white mica from 16TP04B (Figure 3-6B) resulted in a plateau age of 459.9 ±3.3 Ma that incorporates 100% of the cumulative ^{39}Ar released. After the first 27% of ^{39}Ar released, there is a clear gradient in apparent ages from 445–471 Ma as the temperature increases until the end of the experiment. The minimum apparent age included within plateau steps is 444.8 ± 7.9 Ma.

3.4 16TP05BA

Thin Section Observations

Sample 16TP05BA is a sample of felsic gneiss from an outcrop in Eclogite Brook (Figure 3-1). In outcrop and hand sample, there is a contact with the well-foliated mica-rich felsic gneiss and a layer of actinolite-rich albite schist that has randomly oriented actinolite grains. A thin section that includes lithologic contact was cut relative to an L_n stretching lineation defined by elongate white mica grains in the mica-rich felsic gneiss.

In thin section, S_{n-1} is defined by inclusions of quartz, white mica, biotite, and albite in 0.3–2.0 mm garnet porphyroblasts (Figure 3-2C, 3-2D). S_n is the dominant penetrative fabric in the thin section, and is defined primarily by compositional banding of quartz with layers of white mica, chlorite, and epidote, and lesser amounts of garnet and titanite. Albite porphyroblasts are located primarily with chlorite and actinolite, and appears to include S_n. Titanite grains are variable in grain size ($\leq$ 1 mm) throughout the thin section, and most contain inclusions. White mica grains in the gneiss near the actinolite contact have biotite rims. Approaching the contact, garnet is partially pseudomorphed and has chlorite tails that indicate top-to-the-E shear sense with a normal component (Figure 3-2D). Quartz grains in the thin section are variable in size, with grain boundary migration being the dominant method of recrystallization. Subgrain rotation recrystallization and grain boundary area reduction structures are also apparent, with minimal bulging structures.

$^{40}Ar/^{39}Ar$ Geochronology

A single aliquot of white mica was analyzed from 16TP05BA (Figure 3-6C), which yielded a plateau age of 466.2 ± 2.7 Ma, including 78.8% of the cumulative ^{39}Ar released. The minimum apparent age, not included within the plateau, is 419 ± 19 Ma.

Actinolite step-heating analysis from sample 16TP05BA yielded a complex age spectra (Figure 3-7B) that does not show a distinct pattern over the first 20% of ^{39}Ar released. In these lower temperature steps, ages range from Hadean to Neoproterozoic. Throughout the remainder of the steps, ages range from 705–605 Ma.

U/Pb Geochronology

Titanite from sample 16TP05BA was analyzed using U/Pb LA-ICP-MS geochronology. Plotted on a Terra-Wasserburg Concordia diagram, intercepts are present at 460 ± 17 Ma and 4959 ± 5.3 Ma (Figure 3-8). A single spot analysis yields the highest uranium concentration amongst the population of analyzed spot locations and falls close to the 460 ± 17 Ma intercept. The bulk of spots analyzed have $^{238}U/^{206}Pb$ and $^{207}Pb/^{206}Pb$ ratios that plot closely concordant to the early intercept at 4959 ± 5.3 Ma.

3.5 16TP05D

Thin Section Observations:

Sample 16TP05D is a sample taken from the mapped blueschist unit from an outcrop in Eclogite Brook (Figure 3-1). In both hand sample and in thin section, there is distinct layering between chlorite and epidote-rich layers and layers dominated by garnet and quartz. A L_n stretching lineation is defined by elongate fine grains of white mica, and trends ESE.

In the thin section the sample is divided into two compositionally layered domains. In one domain, S_n foliation is defined by very fine grains of epidote, white mica, chlorite, and quartz, with lesser amounts of carbonate and iron oxides. In the other domain of the thin section, alternating thin layers (≤ 0.5 mm) of carbonate and opaques and epidote, chlorite, and white mica define foliation (Figure 3-2E). Microfractures that are filled in with carbonate and opaques postdate the dominant fabric, cross cutting S_n foliation. In the other compositional domain of the thin section, S_n is defined by elongate epidote (0.5–1.0 mm) porphyroblasts, and quartz microlithons, with large (≤ 0.5 mm) garnet porphyroblasts. Quartz grains are amoeboid, suggesting grain boundary migration as the main mechanism of recrystallization. Evidence for subgrain rotation is also present.

^{40}Ar/^{39}Ar Geochronology:

White mica analyzed from 16TP05D yielded a plateau age of 463.7 ± 2.6 Ma, including 96.9% of the ^{39}Ar released (Figure 3-6D). Within the spectra, there is a gradient from younger to older ages as the temperature is increased after ~50% of the ^{39}Ar is released. The minimum apparent age is included within the plateau at 444.8 ± 8.6 Ma.

3.6 16TP08B

Thin Section Observations

Sample 16TP08B is a sample of blueschist from an outcrop 75 m north of Eclogite Brook (Figure 3-1). In outcrop and hand sample, euhedral garnet porphyroblasts (0.5–2 mm) are evident. On the hand sample, an east-trending L_n mineral lineation is defined by elongate glaucophane and white mica.

In thin section, S_{n-1} is preserved as inclusions of omphacite, white mica, titanite, epidote, and glaucophane in garnet porphyroblasts (Figure 3-2F). Based on the orientation of the internal and external foliations relative to garnets, S_{n-1} and S_n foliation are likely sub parallel to one another and define the dominant composite fabric. Amphiboles are zoned with glaucophane cores and actinolite rims, which together with zoned epidote, and white mica define S_{n-1}/S_n, with lesser amounts of calcite and accessory minerals. Variably asymmetric calcite boudins exhibit deformation twining and subgrain rotation. Epidote grains are commonly oriented at a high angle to the dominant foliation. However, the lack of alteration rims between minerals in thin section suggest epidote formed at the same time as glaucophane, white mica, and garnet. Garnet porphyroblasts and larger epidote grains exhibit fractures that are perpendicular to the S_{n-1}/S_n foliation. BSE imagery makes core to rim zoning of glaucophane to actinolite evident (Figure 3-5B). In addition, EDS mapping reveals zoning within garnets of higher manganese composition from the core to the rim (Figure 3-5C). A near-vertical, relative to S_n foliation, fracture cross-cuts S_n foliation and is associated with fine-grained alteration minerals in the surrounding matrix.

^{40}Ar/^{39}Ar Geochronology

Two aliquots of white mica were analyzed from sample 16TP08B (Figure 3-6E), and yielded significantly different plateau ages. The first aliquot resulted in a plateau of 484.6 ± 4.7 Ma that included 62.8% of the cumulative 39Ar released. The second aliquot of white mica resulted in a plateau age of 455.6 ± 5.0 Ma that incorporates 100% of the ^{39}Ar released. From ~20% of the total ^{39}Ar released until the end of the experiment, there

is a gradient in ages from 438–471 Ma as the temperature is increased. The minimum apparent ages of the first and second analyses, included within plateaus, are 471.8 ± 7.5 Ma and 403.8 ± 27.3 Ma, respectively.

Step-heating analyses of two aliquots of glaucophane resulted in complex spectra (Figure 3-6F). The first analysis resulted with an integrated age of 452 ± 3.9 Ma, and showed an inverse relation between temperature increase and apparent age. The second aliquot of glaucophane resulted in an integrated age of 467.6 ± 2.5 Ma, with a similar age gradient to the first. The recorded minimum ages are 418.2 ± 15.1 and 417.5 ± 6.3 Ma, respectively.

3.7 16TP15A/B

Thin Section Observations

Sample 16TP15A and 16TP15B are samples of pelitic schist intercalated within blueschist taken from an outcrop 70m southwest of Tillotson Camp in Lockwood Brook (Figure 3-1). In the hand sample for 16TP15A two distinct foliations are examined, the dominant of which S_n, is crenulated by S_{n+1}. L_n is a mineral lineation defined by elongate white mica that trends WNW. An S_{n+2} crenulation just slightly oblique to S_{n+1} is apparent in hand sample but cryptic in thin section based on the low angle relative to S_{n+1}.

In the thin section for sample 16TP15A, S_n is a spaced foliation is defined by coarse (0.5–1 mm) white mica domains and microlithons composed of quartz, garnet, and coarse (0.5–2.0 mm) glaucophane porphyroblasts (Figure 3-2g). Inclusions in glaucophane, as well as actinolite rims suggest that glaucophane may be relict of S_{n-1} formation. Additional evidence is given by the orientation of grains relative to the

dominant lineation direction. Garnets within this sample exhibit little, if any, alteration. S_{n+1} foliation is a spaced crenulation that deforms the dominant foliation (Figure 3-2G). Like most other samples, lobate grain shapes of quartz and minor amounts of subgrain rotation, bulging recrystallization, and polygonal quartz boundaries are all locally apparent.

In the hand sample and thin section for sample 16TP15B, isoclinal intrafolial folds are noted as a part of S_n foliation (Figure 3-2H) defined by layers of carbonate and epidote, white mica, and chlorite.

^{40}Ar/^{39}Ar Geochronology

Step-heating analysis on a single aliquot of white mica from 16TP15A (Figure 3-6G) yielded a plateau age of 461.8 ± 2.1 Ma, including 84.9% of the cumulative ^{39}Ar released. Approximately 75% of gas is released over five steps that have an age range of c. 463.1– 464.7 Ma. The minimum apparent age of this aliquot falls within the plateau at 449.5 ± 9.9 Ma.

3.8 16TP15D

Thin Section Observations

Sample 16TP15D is composed of pelitic schist taken from an outcrop in Lockwood Brook 100 m southwest of Tillotson Camp (Figure 3-1). In the thin section, anastomosing S_n foliation is defined by white mica and graphite rich domains. Garnet porphyroblasts are well preserved, and locally the relationship between internal and external foliations relative to garnet suggest that inclusion trails may be remnant of S_{n-1} foliation (Figure 3-2I). Rotated carbonate porphyroblasts exhibit deformation twinning.

Quartz domains exhibit polygonal textures indicative of grain boundary area reduction, and locally preserve grain boundary migration and subgrain rotation recrystallization microstructures.

^{40}Ar/^{39}Ar Geochronology

White mica from 16TP15D (Figure 3-6H) yielded a plateau age of 464.7 ± 3.6 Ma, including 82.8% of the ^{39}Ar released. The minimum apparent age, within steps that define the plateau, is 443.8 ± 13.3 Ma.

3.9 16TP16A

Thin Section Observations:

Sample 16TP16A is a sample of felsic gneiss taken from Eclogite Brook (Figure 3-1). In hand sample and outcrop, multiple foliation generations are observed. S_n is the dominant foliation, which is deformed by a S_{n+1} crenulation foliation. The thin section was cut relative to an east-trending $L_{n/n+1}$ intersection crenulation hinge line.

The observed S_{n+1} crenulation foliation is a near vertical, relative to S_n, spaced crenulation that deforms the dominant S_n foliation. S_n is a spaced foliation defined by domains of coarse-grained white mica, as well as quartz microlithons with garnet pseudomorphs, carbonate, and minor tourmaline (Figure 3-2J). S_{n-1} foliation is preserved as inclusions in garnets that have been replaced by chlorite pseudomorphs. Tourmaline grains are distinctly zoned from core to rim and are randomly oriented relative to the dominant lineation direction. Carbonate grains observed within thin section have deformation twinning, as well as evidence for subgrain rotation recrystallization. Randomly oriented white mica exhibits a decussate texture that may have formed after

S_{n+1} formation. Quartz recrystallization structures include grain boundary migration, bulging, grain boundary area reduction, and subgrain rotation recrystallization.

^{40}Ar/^{39}Ar Geochronology

A single aliquot of white mica was analyzed and yielded a plateau age of 461 ± 2.9 Ma (Figure 3-6I), incorporating 100% of the cumulative ^{39}Ar released. The spectra has a "hump" shape with steps on either end of the spectra bracketing three steps that are older, but still within the plateau. The minimum apparent age of younger steps included in this plateau is 445.3 ± 8 Ma.

Like sample 16TP03A, the step-heating analysis performed on a single aliquot of tourmaline resulted in an age gradient from older to younger ages with increasing temperatures of release (Figure 3-7A).

3.10 16TP17B

Thin Section Observations:

Sample 16TP17B is a sample of felsic gneiss taken from Eclogite Brook (Figure 3-1). In hand sample and outcrop, chlorite pseudomorphs of euhedral garnets with asymmetric tails are present. A single S_n foliation is present, and the thin section is cut with respect to L_n; a NE trending stretching lineation defined by elongate white mica.

In thin section, spaced S_n foliation is defined by coarse-grained white mica and quartz-rich microlithons, with chlorite psuedomorphs after garnet, fine-grained epidote and opaques present as well (Figure 3-2K). Garnets in the thin section are partially to fully pseudomorphed to chlorite. Inclusion trails in porphyroblasts and sigma clast tails indicate top-to-the-NE shear sense. Like most samples in the field area the main methods

of quartz recrystallization are grain boundary migration, subgrain rotation recrystallization, and bulging.

^{40}Ar/^{39}Ar Geochronology:

Step-heating of white mica from sample 16TP17B did not result in a plateau age (Figure 3-6J). The spectra varies by only 10 million years over 90% of the cumulative ^{39}Ar released. One outlier, a medium-high temperature step, records a minimum age of 403.9 Ma ± 6.9 Ma. The total gas integrated age of white mica from this sample is 446.3 ± 2.2 Ma.

3.11 16TP19A

Thin Section Observations:

Sample 16TP19A is a sample of felsic gneiss taken from an outcrop in Lockwood Brook (Figure 3-1). In hand sample, S_n is the penetrative fabric noted. $L_n/_{n+1}$ is a crenulation intersection of S_{n+1} that is sub parallel to a L_n stretching lineation defined by elongate chlorite and white mica. Sn+1 is near-vertical with respect to S_n foliation.

S_n is a continuous foliation that is defined primarily by very fine-grained white mica, epidote, and chlorite (Figure 3-2I). S_{n-1} in thin section is defined by inclusion trails in rotated garnet porphyroblasts. Chlorite-rich tails on garnet porphyroblasts indicate greenschist-facies top-to-the-SW directed deformation, with a normal component. S_{n+1} is difficult to discern in thin section but is confirmed by the observation of continually warped S_n foliation in hand sample.

$^{40}Ar/^{39}Ar$ Geochronology:

Analysis on a single aliquot of white mica from 16TP19A results in a plateau age of 465.9 ± 2.5 Ma (Figure 3-6K), including 96.9% of the ^{39}Ar released. Three initial low temperature steps, which are not included in the plateau, record ages of c. 468–494 Ma. The minimum apparent age of younger steps included in the plateau is 460.6 ± 5.1 Ma.

3.12 16TP21A

Thin Section Observations:

Sample 16TP21A is a sample of Hazens Notch Schist taken from an outcrop approximately one km northwest of Monteith road (Figure 3-1). In hand sample and outcrop, S_n is present. In the hand sample, it is possible to determine a top-to-the-NNE apparent shear sense. The thin section was cut relative to L_n, a stretching lineation defined by elongate white mica grains.

In the thin section, S_n is defined by quartz and albite rich microlithons (Figure 3-2M), as well as by domains of white mica, chlorite, and epidote. Like in samples 16TP03A and 16TP16A, zoned tourmalines are present as a minor accessory mineral. Isoclinal intrafolial F_n folds of white mica are present and are axial planar to S_n. The top-to-the-NNE shear sense determined in hand sample is supported by variably asymmetric boudinage structures composed of quartz and albite in thin section. Quartz exhibits recrystallization primarily by grain boundary migration, with minor subgrain rotation recrystallization.

$^{40}Ar/^{39}Ar$ Geochronology:

Two separate aliquots of white mica were examined from sample 16TP21A (Figure 3-6L). The first aliquot released too little gas to be analyzed. The second aliquot of white mica yielded a plateau age of 454 ± 2.7 Ma, including 87% of the ^{39}Ar released in the experiment. The minimum apparent age of this sample, not included within plateau steps, is 427.4 ± 17.4 Ma.

3.13 16TP22A

Thin Section Observations:

Sample 16TP22A is a sample of felsic gneiss that was taken from an outcrop at the Hazens Notch Campground (Figure 3-1). The thin section was cut relative to an L_n stretching lineation defined by elongate grains of chloritoid and white mica.

In thin section, a spaced S_n foliation is defined primarily by domains of white mica and quartz microlithons. Lesser minerals in the thin section include epidote, albite, titanite, chlorite pseudomorphs after garnet, and (Figure 3-2N). A top-to-the-NE, shear sense is indicated by the presence of delta clast tails on chlorite pseudomorphs after garnet composed of white mica and chlorite (Figure 3-2N). Also present in thin section is a dextral sense shear band that is oblique to S_n. Quartz is primarily located in bands where grain size varies. Quartz recrystallization structures include grain boundary migration primarily, with lesser amounts of subgrain rotation recrystallization and grain boundary area reduction.

$^{40}Ar/^{39}Ar$ Geochronology:

White mica from 16TP22A yielded a plateau age of 454.0 ± 2.7 Ma, including 97% of the ^{39}Ar (Figure 3-6M). An initial low temperature step, not incorporated within the plateau, gives an apparent minimum age of 428.1 ± 12.8 Ma.

3.14 16TP24A/B

Thin Section Observations:

Sample 16TP24A is a sample from the mapped blueschist taken from an outcrop 750 m east of the summit of Tillotson Peak (Figure 3-1). In the hand sample of 16TP24A, isoclinal folding is noted in both X-Z and Y-Z cuts.

In thin section, S_n and intrafolial isoclinal folds of S_n (F_n) are defined by very fine grains of white mica, chlorite, and epidote with compositional bands of carbonate, epidote, opaques, and garnet porphyroblasts. (Figure 3-2O). S_{n-1} is preserved as inclusions in rotated garnet porphyroblasts that are, for the most part, unaltered. Folding about F_n makes determining kinematic movement difficult. One prominent near-vertical, relative to S_n, microfracture cuts all S_n foliation.

$^{40}Ar/^{39}Ar$ Geochronology:

A single analysis on white mica from 16TP24A (Figure 3-6N) yielded a plateau age of 464.0 ± 2.9 Ma, including 95.6% of the cumulative ^{39}Ar released. The minimum apparent age of steps included within this plateau is 454.7 ± 8.2 Ma.

3.15 16TP26A

Thin Section Observations:

Sample 16TP26A is taken from an outcrop of Hazens Notch schist on the Long Trail one km northeast of the summit of Tillotson Peak (Figure 3-1). In hand sample and outcrop, a single L_n stretching lineation is defined by elongate white mica grains.

In thin section S_n is defined by white mica and biotite, with quartz-rich microlithons. In quartz-rich microlithons, white mica is oblique to S_n and defines S_{n-1} foliation (Figure 3-2P). Recrystallization mechanisms in quartz are primarily related to grain boundary migration and grain boundary area reduction, with lesser amounts of subgrain rotation recrystallization

^{40}Ar/^{39}Ar Geochronology:

Two aliquots of white mica were analyzed from 16TP26A (Figure 3-6O). The first aliquot gives a plateau age of 480.5 ± 3.3 Ma; including 86.1% of the ^{39}Ar released. The second aliquot of white mica from this sample yielded a plateau age of 469.7 ± 3.5 Ma, including 79.8% of the ^{39}Ar. Both samples show an apparent age gradient of younger to older ages from ~30% of the total ^{39}Ar released through the end of the experiment as the temperature is increased. The minimum ages of these analyses are 434.8 ± 17.6 Ma and 419 ± 16.8 Ma, respectively.

3.16 16TP27A

Thin Section Observations

Sample 16TP27A is taken from a boudin located in the mapped felsic gneiss in Eclogite Brook near samples 16TP05BA and 16TP05D (Figure 3-1). In thin section, S_{n-1} is observed in garnet porphyroblasts (0.25–0.5 mm) as inclusion trails. S_n foliation is defined primarily by epidote, chlorite, and white mica. In addition, lesser amounts of titanite, rutile, carbonate, and garnet porphyroblasts are present. Coarse-grained amphibole porphyroblasts overgrow S_n foliation (Figure 3-2Q). Carbonate grains exhibit deformation twins, and quartz exhibits grain boundary migration.

3.17 Kinematic Indicators in Additional Samples

Additional thin sections that were examined in detail, but were not analyzed with $^{40}Ar/^{39}Ar$ geochronology include samples of retrogressed blueschist and metapelites. Samples 16TP05A, 16TP05F, 16TP07A are all taken from outcrops in Eclogite Brook (Figure 3-1). Kinematic indicators in these samples give a sinistral, approximately top-to-the-E, shear sense with a normal component. Sample 16TP15E, from Lockwood Brook, has a sinistral, top-to-the-SE shear sense with a reverse component.

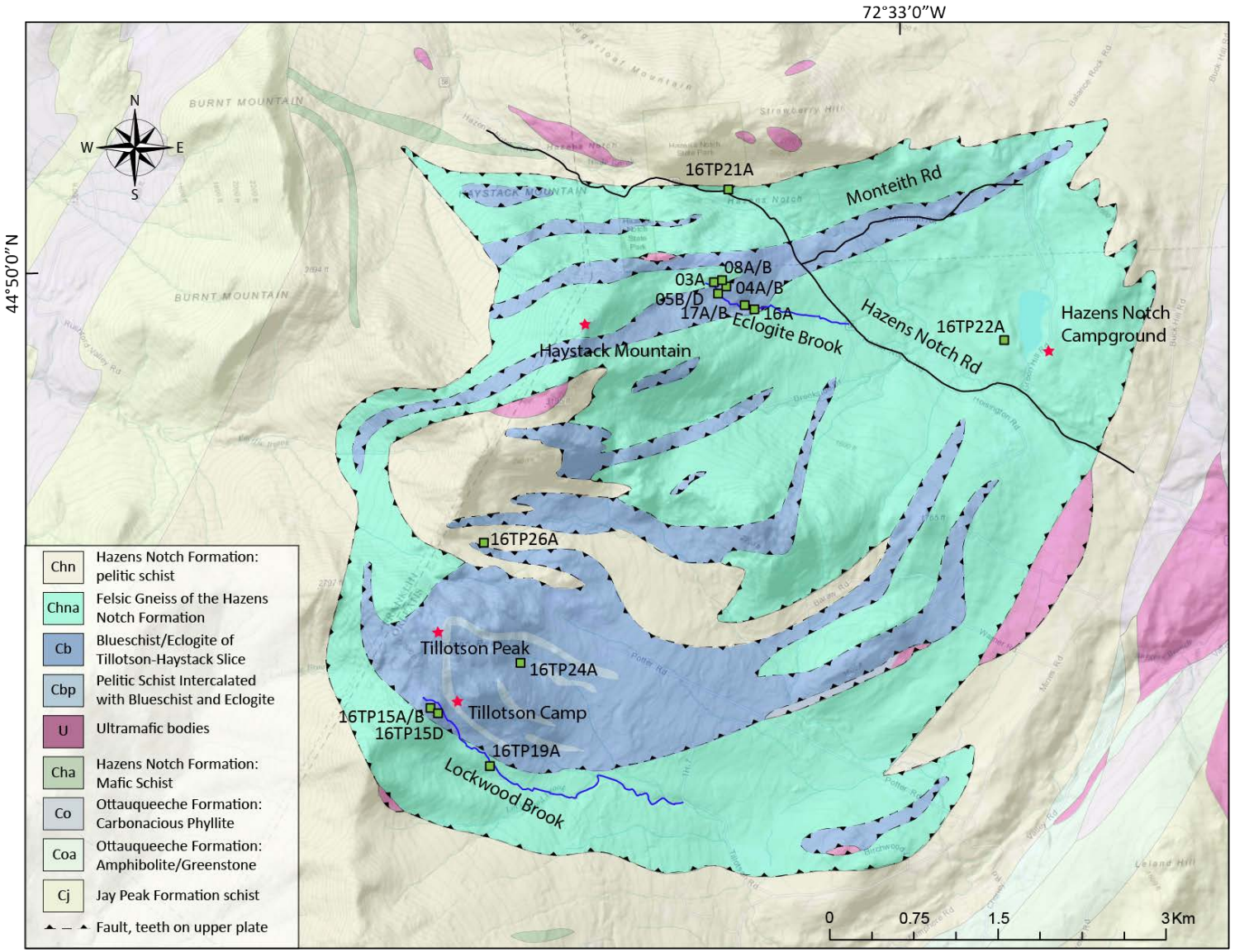
72°33'0"W
44°50'0"N
N
W
E
S
BURNT MOUNTAIN
BURNT MOUNTAIN
Monteith Rd
16TP21A
08A/B
03A
04A/B
05B/D
17A/B
16A
Eclogite Brook
Haystack Mountain
Hazens Notch Rd
16TP22A
Hazens Notch Campground
16TP26A
Tillotson Peak
16TP24A
16TP15A/B
16TP15D
Tillotson Camp
16TP19A
Lockwood Brook
Chn Hazens Notch Formation: pelitic schist
Chna Felsic Gneiss of the Hazens Notch Formation
Cb Blueschist/Eclogite of Tillotson-Haystack Slice
Cbp Pelitic Schist Intercalated with Blueschist and Eclogite
U Ultramafic bodies
Cha Hazens Notch Formation: Mafic Schist
Co Ottauqueeche Formation: Carbonacious Phyllite
Coa Ottauqueeche Formation: Amphibolite/Greenstone
Cj Jay Peak Formation schist
Fault, teeth on upper plate
0
0.75
1.5
3Km

Figure 3-1: Geologic map of the Tillotson Peak Complex modified from the bedrock mapping of Bothner and Laird (1999). a) Map of the TPC with mentioned locations from this study and Bothner and Laird (1987) included for context. b) Geologic map of the TPC with locations of samples examined in this study.

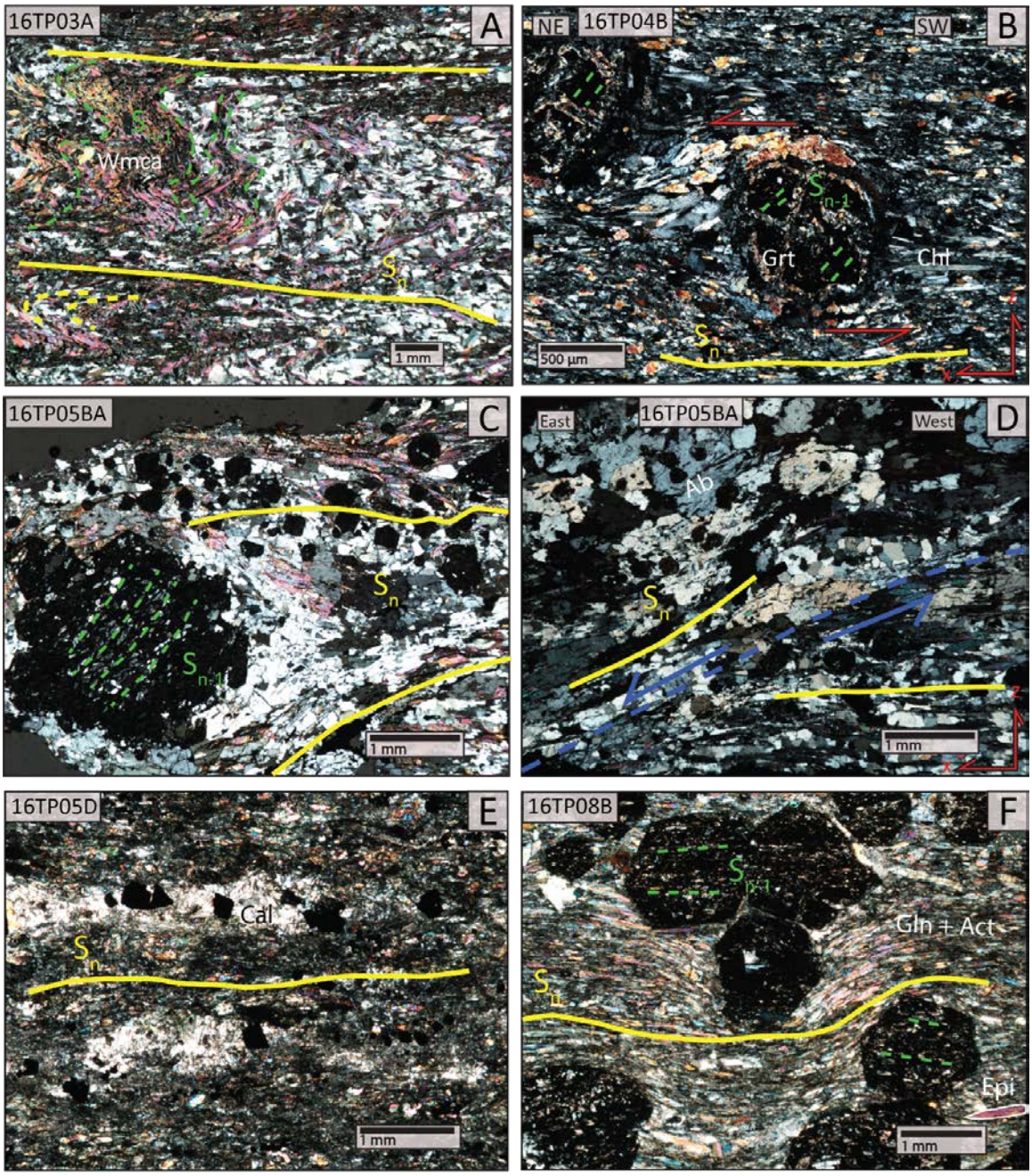
16TP03A
A
Wmca
S_n
1 mm
NE
16TP04B
SW
B
S_{n-1}
Grt
Chl
S_n
500 µm
16TP05BA
C
S_n
S_{n-1}
1 mm
East
16TP05BA
West
D
Ab
S_n
1 mm
16TP05D
E
Cal
S_n
1 mm
16TP08B
F
S_{n-1}
Gln + Act
S_n
Epi
1 mm

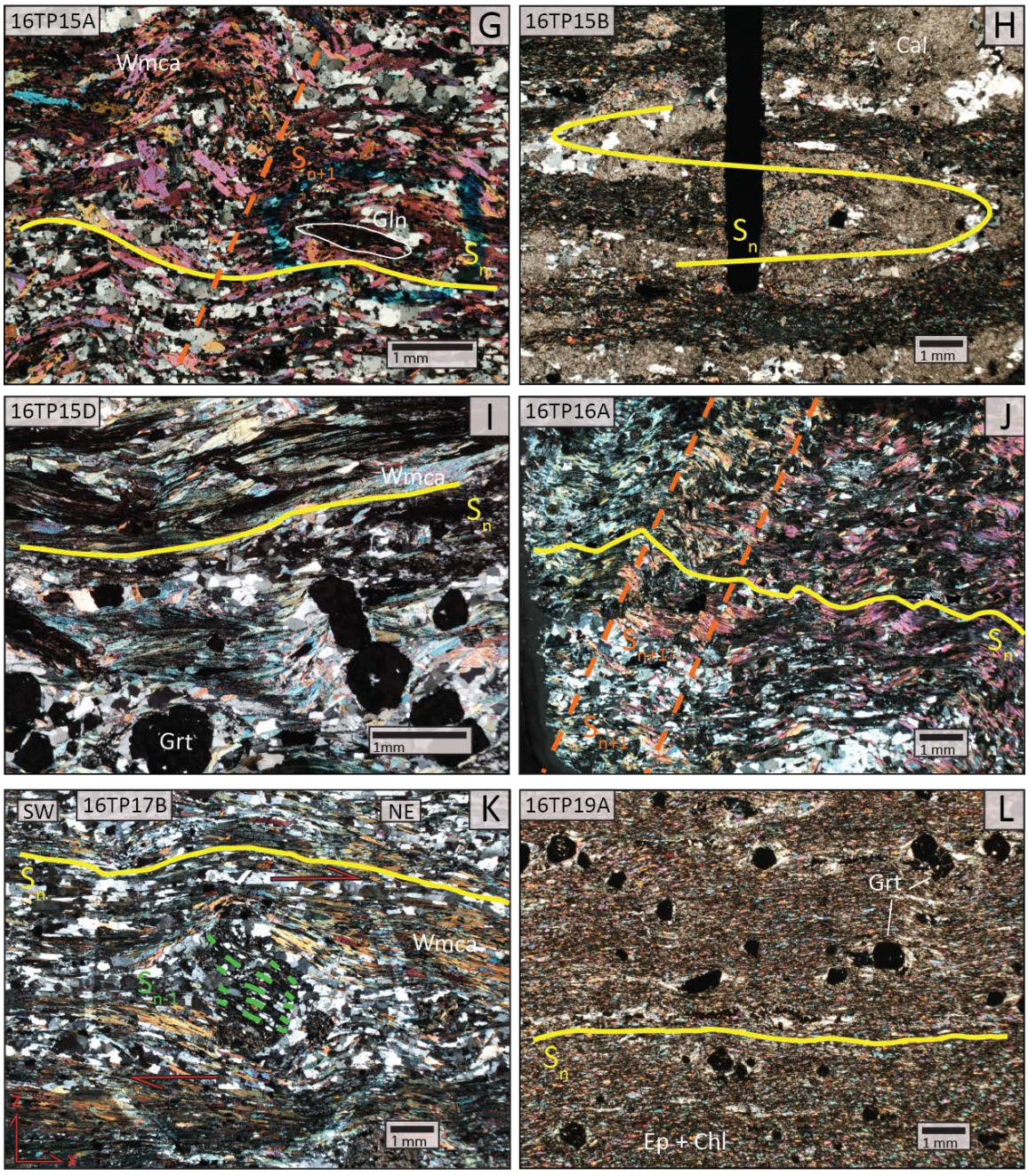
16TP15A
G
Wmca
S_{n+1}
Gln
S_n
1 mm
16TP15B
H
Cal
S_n
1 mm
16TP15D
I
Wmca
S_n
Grt
1mm
16TP16A
J
S_{n+1}
S_n
S_{n+1}
1 mm
SW
16TP17B
NE
K
S_n
Wmca
S_{n-1}
1 mm
16TP19A
L
Grt
S_n
Ep + Chl
1 mm

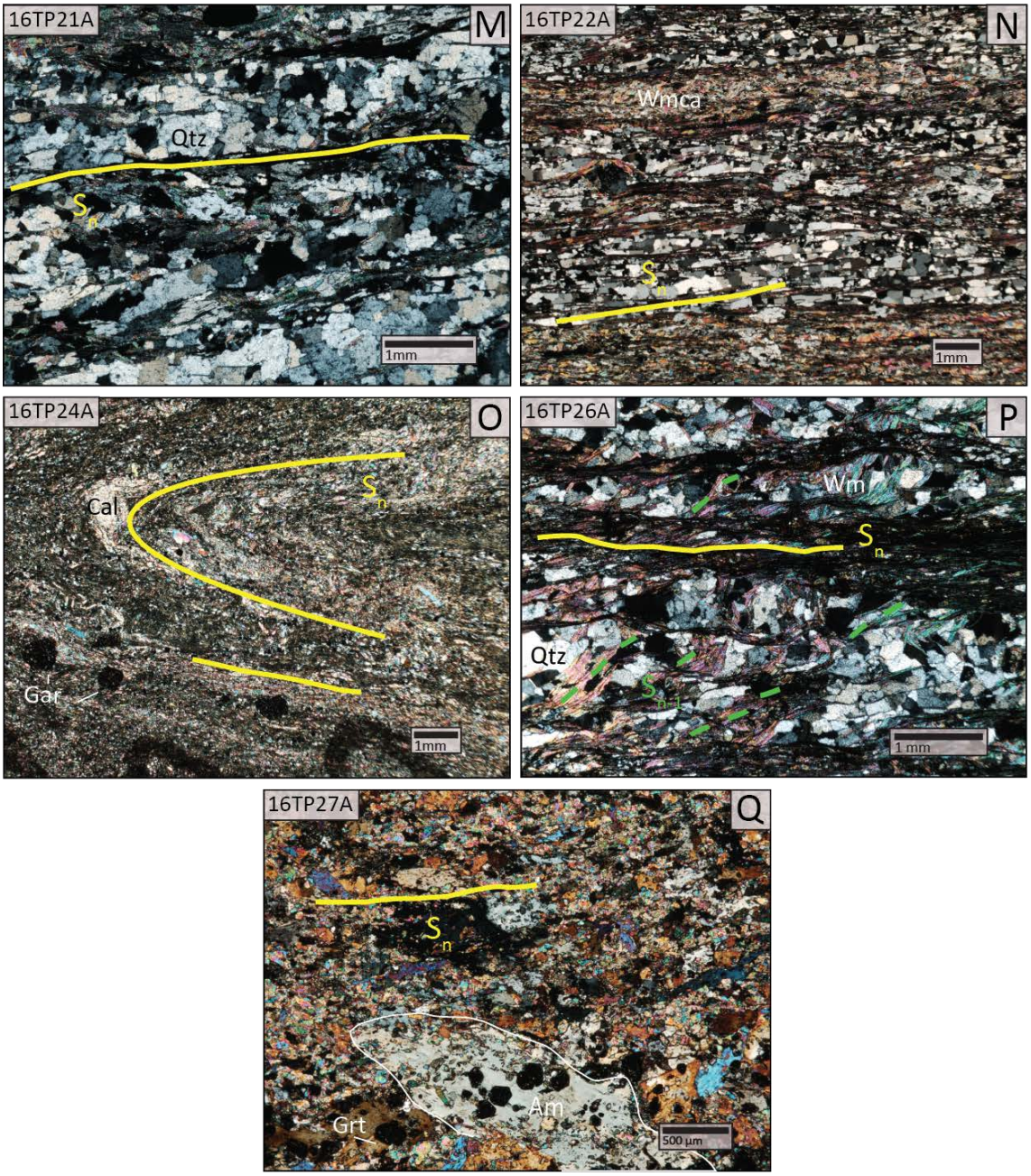
16TP21A
M
Qtz
S_n
1mm
16TP22A
N
Wmca
S_n
1mm
16TP24A
O
Cal
S_n
Gar
1mm
16TP26A
P
Wm
S_n
Qtz
S_{n-1}
1 mm
16TP27A
Q
S_n
Am
Grt
500 µm

Figure 3-2: Photomicrographs from selected samples in cross polarized light. Mineral abbreviations from Siivola and Schmid (2007), where Ab = albite, Act = actinolite, Am = amphibole, Cal = calcite, Chl = Chlorite, Ep = epidote, Gln = glaucophane, Grt = garnet, Qtz = quartz, and Wmca = white mica. X-Z arrows refer X-Z directions of finite strain ellipse; X: trend of the dominant lineation direction, Z: "top" of the sample relative to an oriented surface. S_n refers to the planar feature that the sample is oriented relative to. Orientations of structures are reported as trend/plunge for linear features and strike/dip for planar features. Summary of structures examined in Appendix B (A) 16TP03A: Medium to coarse grain white mica defines S_{n-1} (green), crenulated by S_n (B) 16TP04B: Partially psuedomorphed garnet porphyroblasts with chlorite tails show a sinistral, top-to-the-NE, shear sense. X: stretching lineation L_2 (063/17), strike and dip of S_n: 057/70. (C) 16TP05BA: Large garnet porphyroblasts have relict S_{n-1} foliation (green) preserved as inclusion trails. S_n (yellow) is defined by white mica. (D) 16TP05BA: Sinistral, top-to-the-E, sense shearing (blue) is indicated by the reorientation of S_n (yellow). X: stretching lineation L_2 (090/35), strike and dip of S_n: 273/85 (E) 16TP05D: S_n (yellow)is defined by very fine-grained epidote and white mica. Lightly boudinaged carbonate pods do not give an accurate indicator of shear. (F): 16TP08B: Large garnet porphyroblasts have S_{n-1} inclusion trails (green) defined by omphacite, white mica, titanite, and epidote. S_{n-1} & S_n are nearly parallel to one another, indicated by relationship of internal and external foliation elements, relative to garnet. (G) 16TP15A: White mica domains and quartz microlithons define the dominant S_n (yellow). S_{n+1} (orange) is a crenulation cleavage. Coarse-grained glaucophane porphyroblasts are present in thin section parallel to S_n. (H) 16TP15B: S_n intrafolial folds highlighted by carbonate-rich layers. (I) 16TP15D: Garnet porphyroblasts with little retrograde pseudomorphing. (J) 16TP16A: S_n (yellow) defined by white mica is deformed by S_{n+1} crenulation cleavage. (K) 16TP17B: Pseudomorphs after garnet with S_{n-1} inclusion trails give a sinistral, top-to-the-SW, shear sense. X: stretching lineation L_2 (046/31), strike and dip of S_n: 035/73. (L) 16TP19A: S_n foliation is defined by very fine-grained white mica, epidote, and chlorite, with garnet porphyroblasts. (M) 16TP21A: White mica and quartz microlithons with strain-free polygonal grains define S_n (yellow). (N) 16TP22A: Gneissic layering with S_n defined primarily by white mica and quartz microlithons. Quartz bands have been recrystallized by grain boundary area reduction. (O) 16TP24A: S_n foliation and intrafolial folds (yellow) are defined by white mica, epidote, chlorite, and carbonate and epidote bands. (P) 16TP26A: S_n defined by fine-grained white mica (yellow). White-mica in quartz microlithons preserve S_{n-1} (green). (Q) 16TP27A: Coarse-grained amphibole (white) includes earlier white mica and epidote that define S_n (yellow).

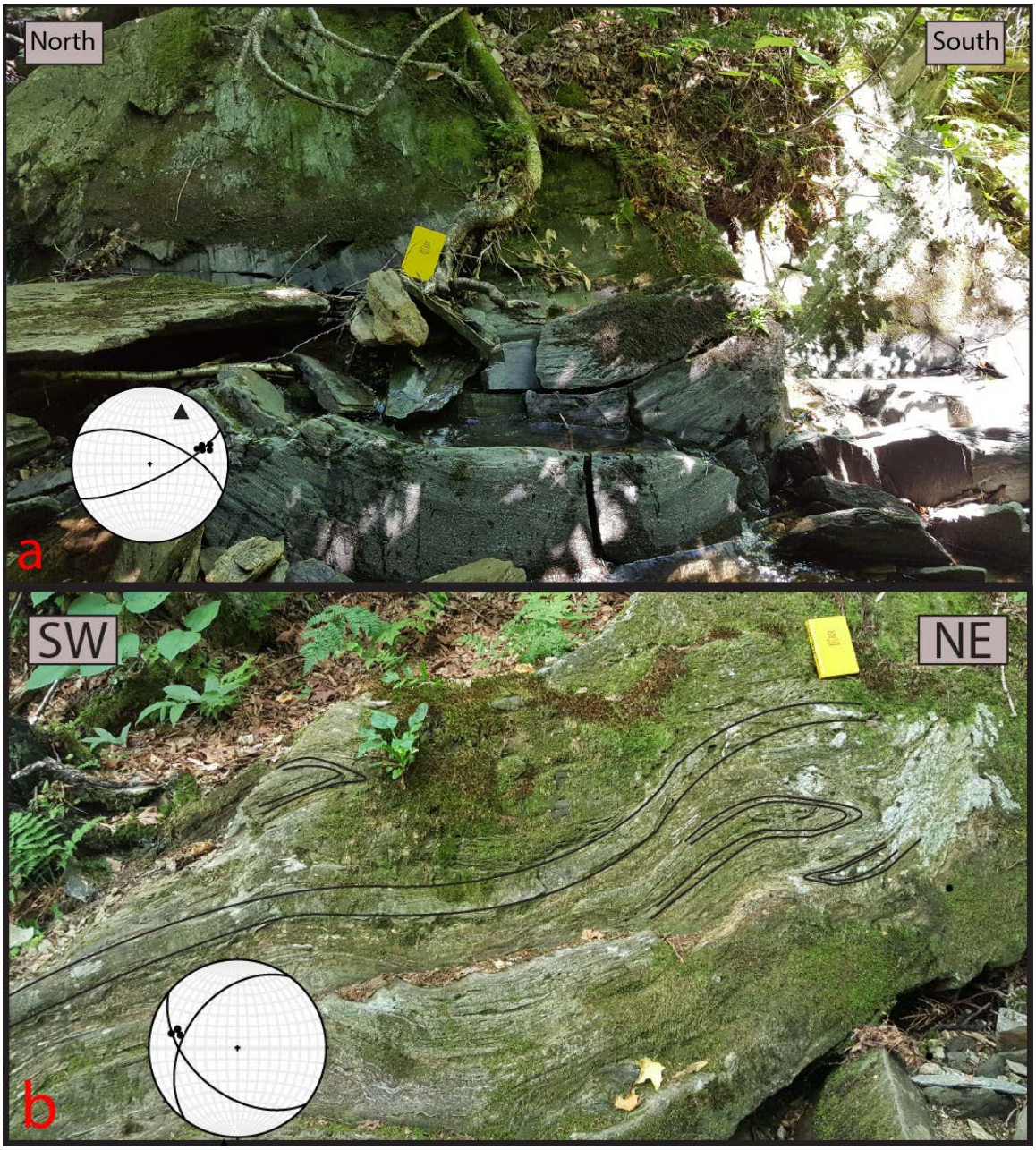

Figure 3-3: F_2 and F_3 folding in the TPC. a) F_3 gentle synform in eclogite brook. Outcrop is composed of felsic gneiss and blueschist-facies rocks. An equal area stereonet shows the pole to the axial plane of F_3 (triangle), fold axis measurements (circles) and foliation measurements (great circles). This outcrop is the location of sample 16TP05D. b) Open F_3 folds and intrafolial F_2. The stereonet shows measured fold limb foliation and axes of F_3 folds. This outcrop is mapped as blueschist near Lockwood Brook.

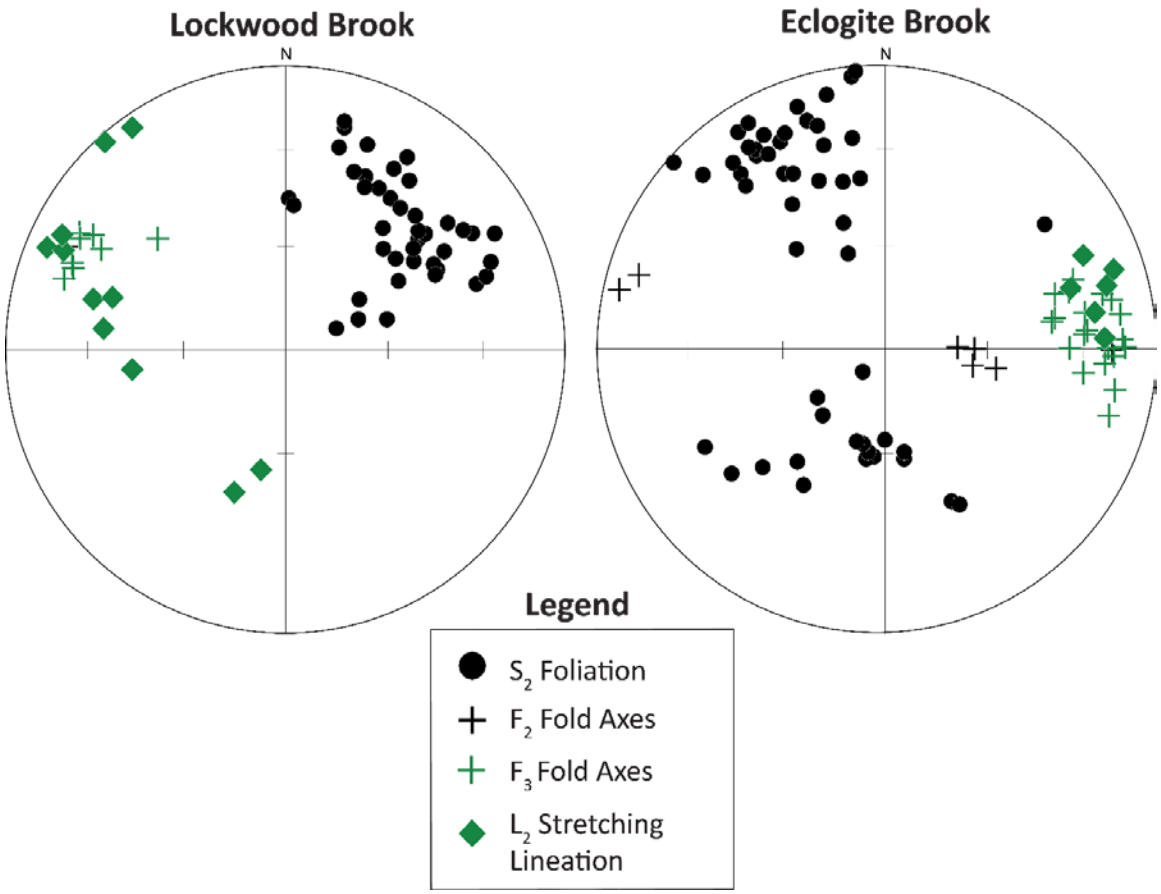

Figure 3-4: Equal-area lower-hemisphere stereonet projections of structural data collected from the areas surrounding Lockwood Brook and Eclogite Brook in the TPC. The presence of NW-trending F_4 about the Gilmore Antiform was confirmed by Bothner and Laird (1987) by the change in the trend of F_3 fold axes from Lockwood Brook to Eclogite Brook (see Figure 3-1 for locations).

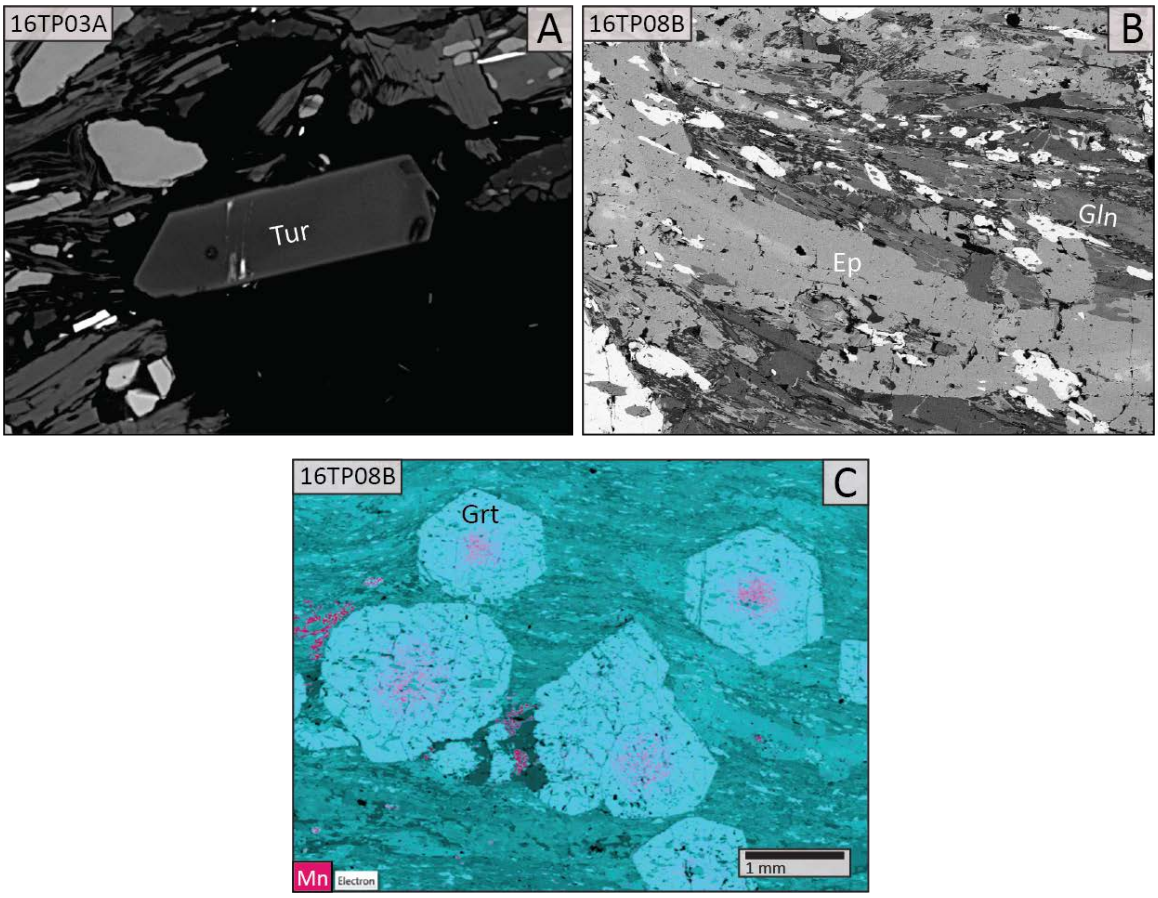

Figure 3-5: SEM images of selected samples. Mineral abbreviations from Siivola and Schmid (2007), where, Ep = epidote, Gln = glaucophane, Grt = garnet, Tur = tourmaline (A) BSE image from sample 16TP03A with tourmaline that shows distinct zoning from the core to the rim of the grain. (B) BSE image from 16TP08B that shows zoning of amphibole from glaucophane cores to actinolite rims. (C) EDS image from 16TP08B with garnets that have manganese rich cores.

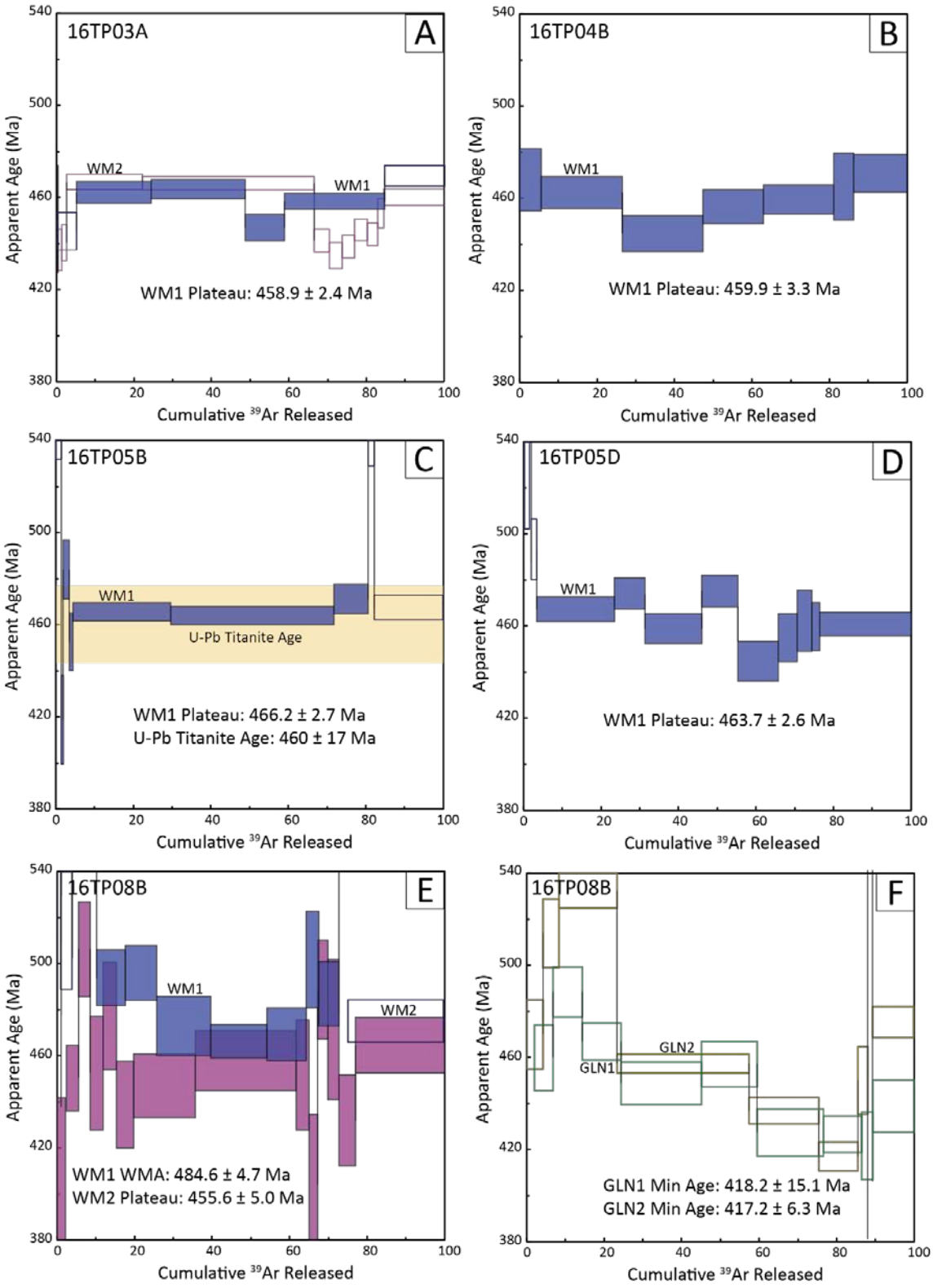
16TP03A
A
WM2
WM1
WM1 Plateau: 458.9 ± 2.4 Ma
16TP04B
B
WM1
WM1 Plateau: 459.9 ± 3.3 Ma
16TP05B
C
WM1
U-Pb Titanite Age
WM1 Plateau: 466.2 ± 2.7 Ma
U-Pb Titanite Age: 460 ± 17 Ma
16TP05D
D
WM1
WM1 Plateau: 463.7 ± 2.6 Ma
16TP08B
E
WM1
WM2
WM1 WMA: 484.6 ± 4.7 Ma
WM2 Plateau: 455.6 ± 5.0 Ma
16TP08B
F
GLN2
GLN1
GLN1 Min Age: 418.2 ± 15.1 Ma
GLN2 Min Age: 417.2 ± 6.3 Ma
Apparent Age (Ma)
Cumulative ^{39}Ar Released

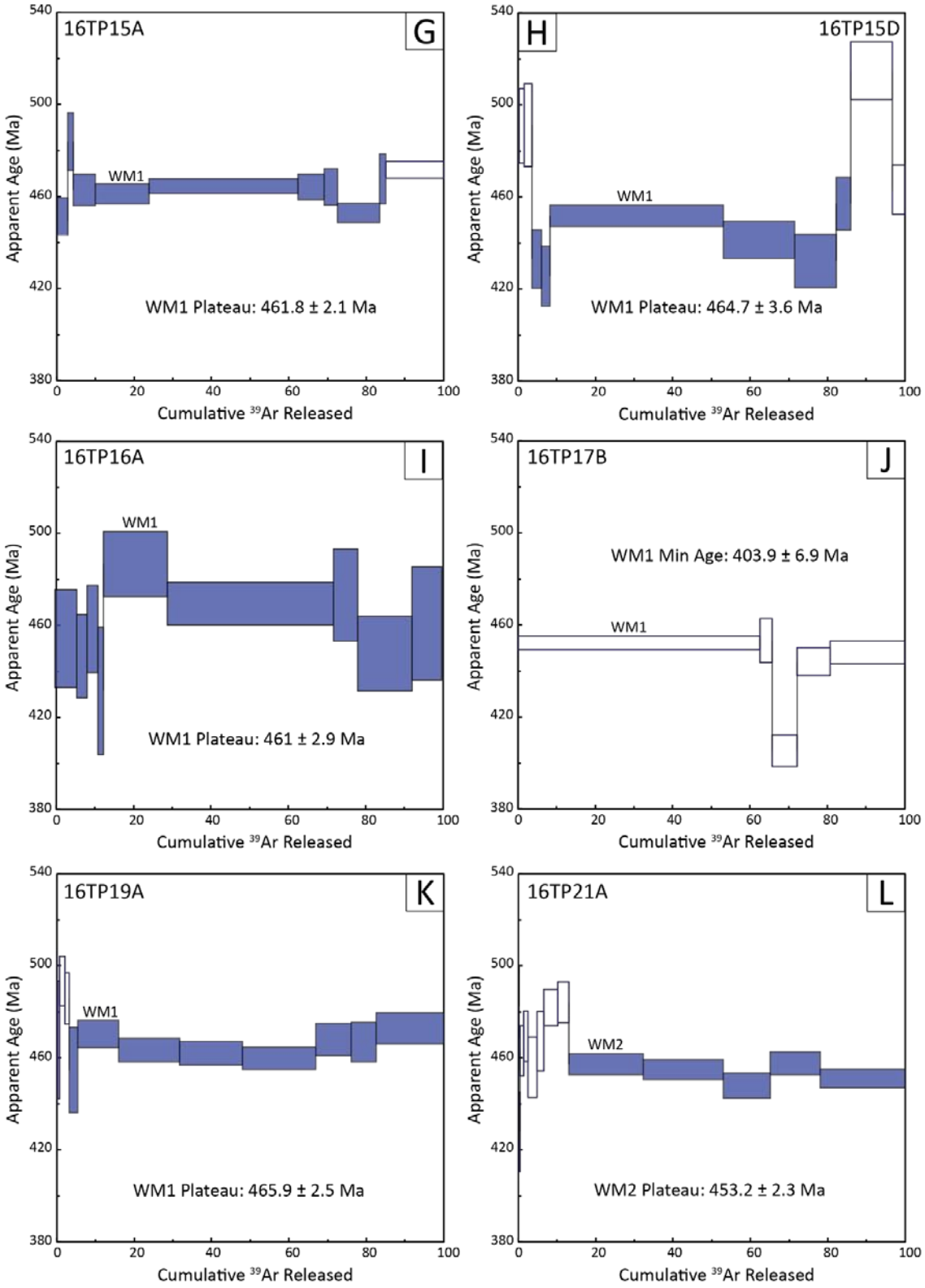
16TP15A
G
WM1
WM1 Plateau: 461.8 ± 2.1 Ma
16TP15D
H
WM1
WM1 Plateau: 464.7 ± 3.6 Ma
16TP16A
I
WM1
WM1 Plateau: 461 ± 2.9 Ma
16TP17B
J
WM1 Min Age: 403.9 ± 6.9 Ma
WM1
16TP19A
K
WM1
WM1 Plateau: 465.9 ± 2.5 Ma
16TP21A
L
WM2
WM2 Plateau: 453.2 ± 2.3 Ma
Apparent Age (Ma)
Cumulative ^{39}Ar Released
540
500
460
420
380
0
20
40
60
80
100

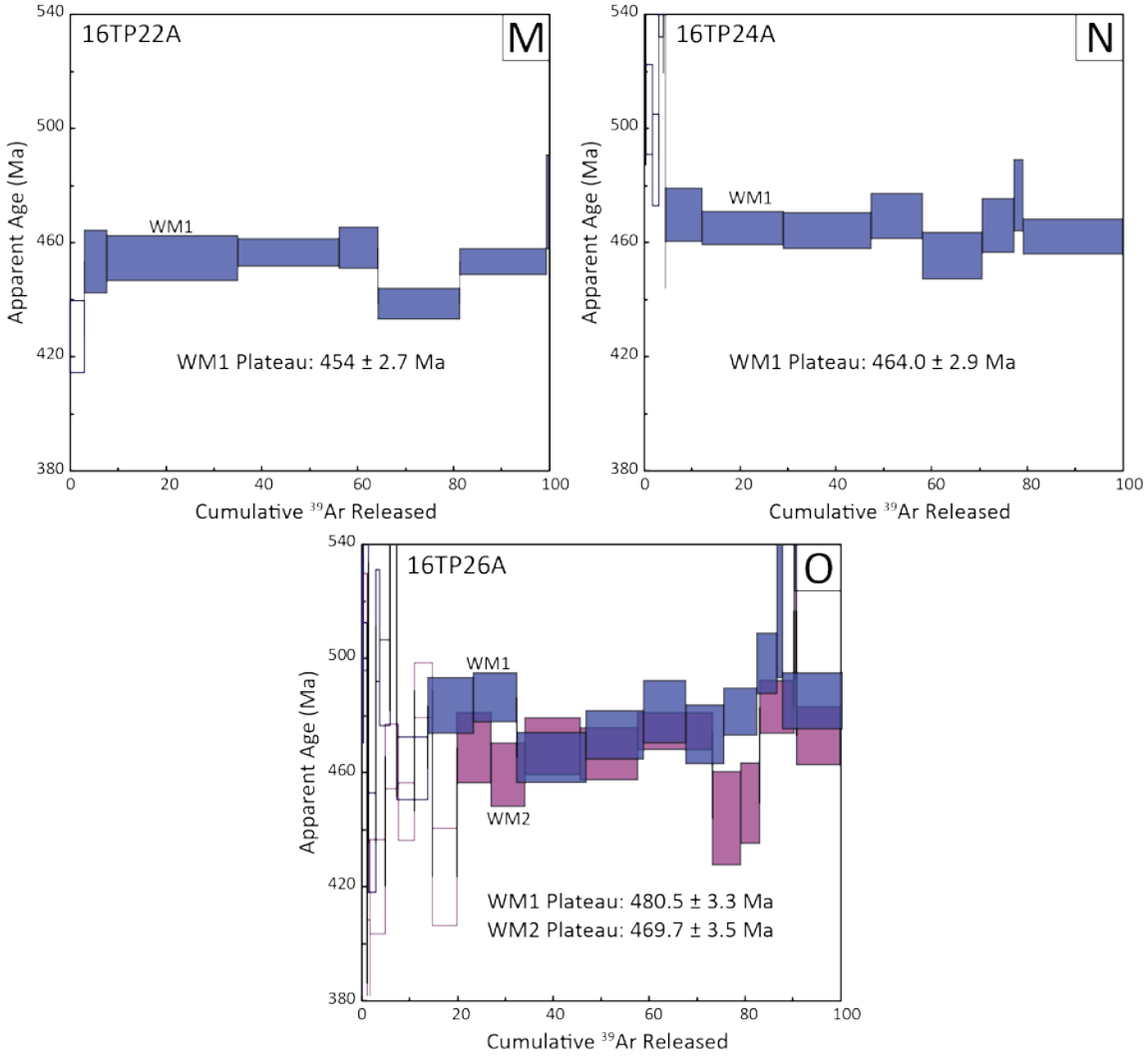
16TP22A
M
WM1
WM1 Plateau: 454 ± 2.7 Ma
Apparent Age (Ma)
Cumulative ^{39}Ar Released
16TP24A
N
WM1
WM1 Plateau: 464.0 ± 2.9 Ma
Apparent Age (Ma)
Cumulative ^{39}Ar Released
16TP26A
O
WM1
WM2
WM1 Plateau: 480.5 ± 3.3 Ma
WM2 Plateau: 469.7 ± 3.5 Ma
Apparent Age (Ma)
Cumulative ^{39}Ar Released

Figure 3-6: Step-heated $^{40}Ar/^{39}Ar$ age spectra from white mica and glaucophane. WM= white mica, GLN= glaucophane. Error bars are 1σ. (A) 16TP03A: WM-1 yields a plateau age of 458.9 ± 2.4 Ma, incorporating 79.5% of the total ^{39}Ar released and a minimum apparent age of 445.3 ± 8.2 Ma. WM-2 gives a minimum apparent age of 435.2 ± 5.5 Ma. (B) 16TP04B: WM-1 yields a plateau age of 459.9 ± 3.3, Ma incorporating 100% of the total ^{39}Ar released and a minimum apparent age of 444.8 ± 7.9 Ma. (C) 16TP05BA: WM-1 yields a plateau age of 466.2 ± 2.7 Ma, incorporating 78.8% of the total ^{39}Ar released and a minimum apparent age of 419 ± 19.2 Ma. Included in yellow is the 460 ± 17 Ma age obtained from in situ U-Pb dating of titanite. (D) 16TP05D: WM-1 yields a plateau age of 463.7 ± 2.6 Ma, incorporating 96.9% of the total ^{39}Ar released and a minimum apparent age of 444.8 ± 7.9 Ma. (E) 16TP08B: WM-1 yields a plateau age of 484.6 ± 4.7 Ma, incorporating 62.8% of the total ^{39}Ar released and a minimum apparent age of 471.8 ± 7.5 Ma. WM-2 yields a plateau age of 455.6 ± 5 Ma, incorporating 100% of the total ^{39}Ar released and a minimum apparent age of 403.8 ± 27.3 Ma. (F) 16TP08B: GLN-1 yields a minimum apparent age of 418.2 ± 15.2 Ma. GLN-2 yields a minimum apparent age of 417.2 ± 6.3 Ma. (G) 16TP15A: WM-1 yields a plateau age of 461.8 ± 2.1 Ma, incorporating 84.9% of the total ^{39}Ar released and a minimum apparent age of 449.5 ± 9.9 Ma. (H) 16TP15D: WM-1 yields a plateau age of 464.7 ± 3.6 Ma, incorporating 82.8% of the total ^{39}Ar released and a minimum apparent age of 443.8 ± 13.3 Ma. (I) 16TP16A: WM-1 yields a plateau age of 461 ± 2.9 Ma, incorporating 100% of the total ^{39}Ar released and a minimum apparent age of 445.3 ± 13.8 Ma. (J) 16TP17B: WM-1 yields a minimum age of 403.9 ± 6.8 Ma. (K) 16TP19A: WM-1 yields a plateau age of 465.9 ± 2.5 Ma, incorporating 96.9% of the total ^{39}Ar released and a minimum age of 455.7 ± 18.5 Ma. (L) 16TP21A: WM-2 yields a plateau age of 453.2 ± 2.3 Ma, incorporating 87% of the total ^{39}Ar released and a minimum apparent age of 427.4 ± 17.4 Ma. (M) 16TP22A: WM-2 yields a plateau age of 454.0 ± 2.7 Ma, incorporating 97% of the total ^{39}Ar released and a minimum apparent age of 428.1 ± 13 Ma. (N) 16TP24A: WM-1 yields a plateau age of 464 ± 2.9 Ma, incorporating 95.6% of the total ^{39}Ar released and a minimum apparent age of 454.7 ± 8.1 Ma. (O) 16TP26A: WM-1 yields a plateau age of 480.5 ± 3.3 Ma, incorporating 86.1% of the total ^{39}Ar released and a minimum apparent age of 434.8 ± 17.6 Ma. WM-2 yields a plateau age of 469.7 ± 3.5 Ma, incorporating 79.8% of the total ^{39}Ar released and a minimum apparent age of 419 ± 16.8 Ma.

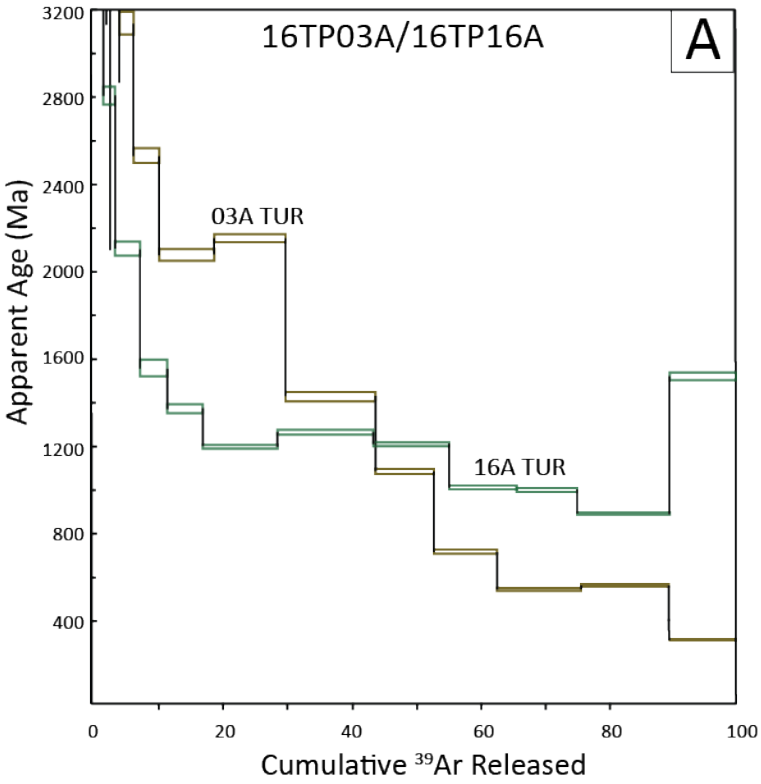
16TP03A/16TP16A
A
03A TUR
16A TUR
Apparent Age (Ma)
3200
2800
2400
2000
1600
1200
800
400
0
20
40
60
80
100
Cumulative ^{39}Ar Released

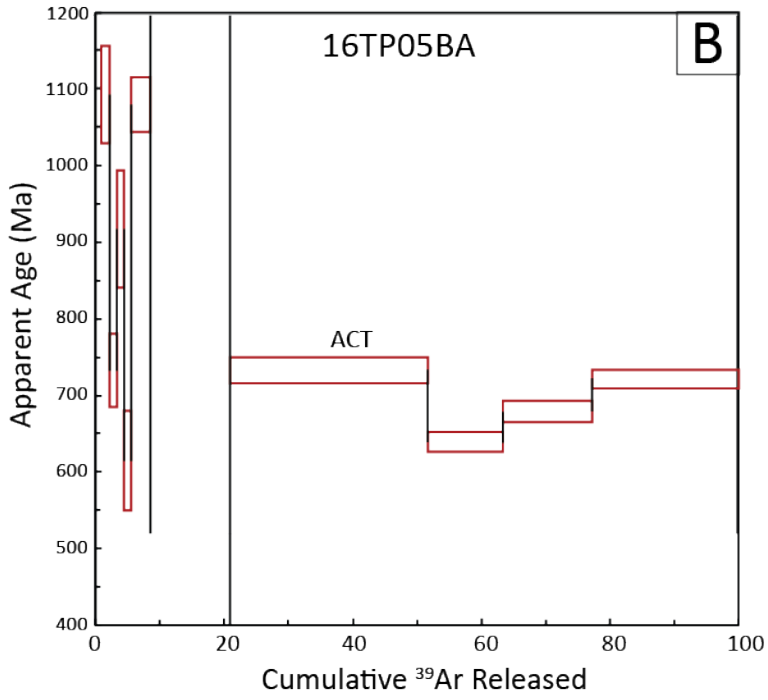
16TP05BA
B
ACT
Apparent Age (Ma)
1200
1100
1000
900
800
700
600
500
400
0
20
40
60
80
100
Cumulative ^{39}Ar Released

Figure 3-7: Step-heated $^{40}Ar/^{39}Ar$ age spectra from tourmaline and actinolite. TUR= tourmaline, ACT= actinolite. Error bars are 1σ. (A) TUR from 16TP03A yields a minimum apparent age of 309.8 ± 5.4 Ma and an integrated total gas age of 1264.9 ± 5.2 Ma. TUR from 16TP16A yields a minimum age of 791.7 ± 5.1 Ma and an integrated total gas age of 1193.6 ± 4.3 Ma. (B) 16TP05BA: ACT yields a minimum apparent age of 579.5 ± 63.7 Ma and an integrated total gas age of 887.3 ± 9.1 Ma.

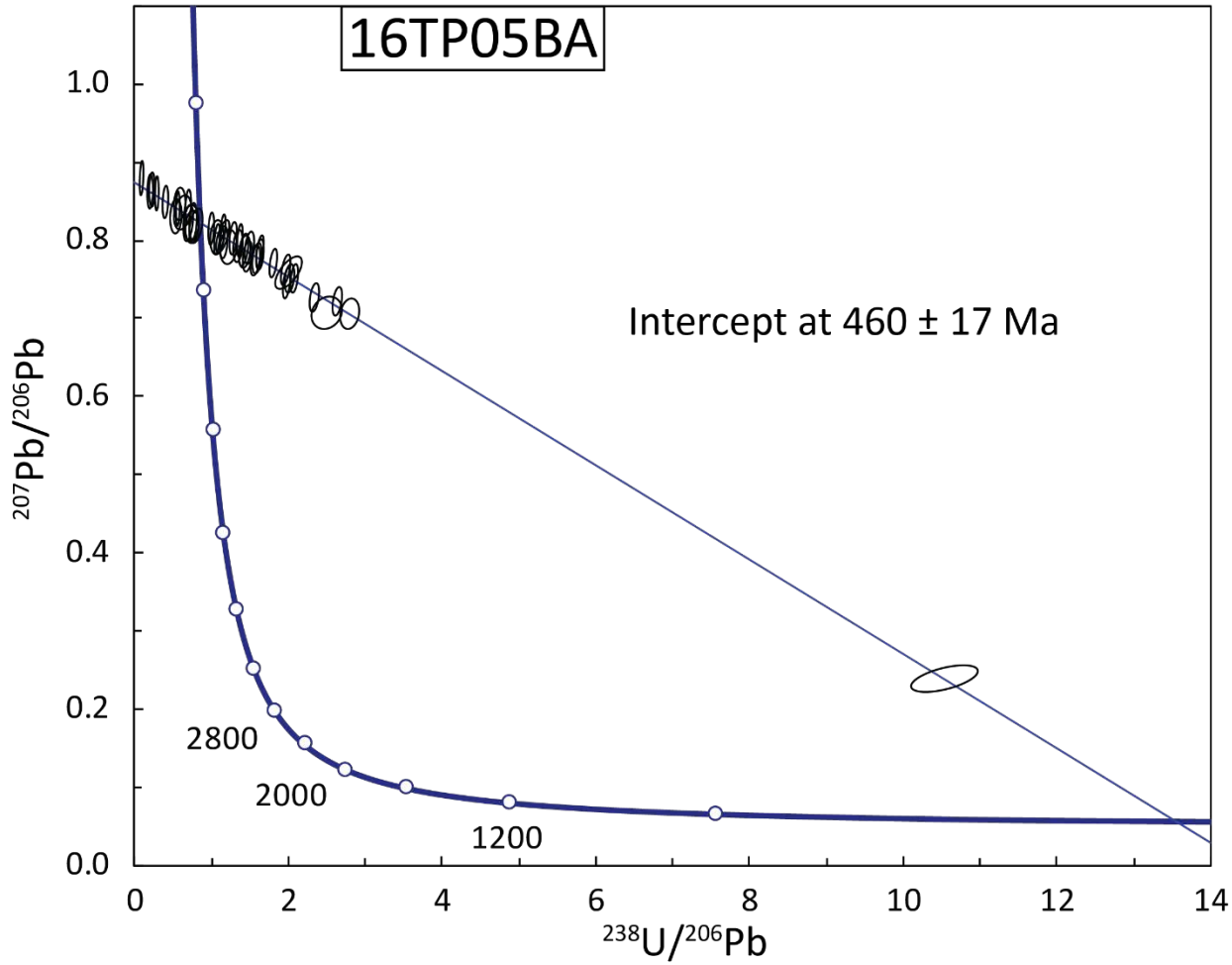

Figure 3-8: Terra-Wasserburg concordia diagram for titanite from sample 16TP05BA. Data point ellipses are 2σ. MSWD = 0.55. Ellipses that are not directly on the concordia curve must have been impacted by lead loss or gain.

Table 3-1: Correlation of structures from the TPC area from previous research (Bothner and Laird, 1987, 1999) and this study.

Deformation		Struture Generation Prior Research	Structure Examined in This Study		
D_3	Large scale upright folding (Gilmore Antiform and Green Mountain Anticlinorium)	S_3 (Acadian S_1), F_3 folding	Locally preserved N–S striking spaced crenulation lightly oblique to S_3	S_4 (Salinic S_1), F_4 folding	**D_4**
D_2	Formation of E-W trending macroscopic folds	Taconian S_2, E–W Map-scale F_2 folding	Near-vertical spaced crenulation cleavage axial planar to F_3 folds	Taconian S_3, E–W Map-scale F_3 folding	**D_3**
D_1	Regional retrograde deformation and exhumation	Taconian S_1, Isoclinal F_1 folds	Dominant transposition surface, axial planar to isoclinal intrafolial folds. Often parallel to original lithologic Layering	Taconian S_2, isoclinal F_2 folds, L_2 stretching lineations	**D_2**
	Prograde deformation and metamorphism of rocks in the region		Preserved as inclusions in garnet porphyroblasts and as relict micas oblique to dominant foliation	Taconian S_1	**D_1**

Table 3-2: Individual structural elements in thin section correlated with the four foliation generations interpreted for the evolution of the TPC.

	Structure			
Sample	**S_1**	**S_2**	**S_3**	**S_4**
16TP03A		S_{n-1} defined by white mica and quartz foliation that is deformed by S_{n+1}	S_n is a spaced crenulation cleavage	
16TP04B	S_{n-1} is preserved as inclusions in of white mica and epidote fractured garnet porphyroblasts	S_n continuous foliation defined by fine grained white mica, chlorite, epidote		
16TP05BA	S_{n-1} is preserved as inclusions of quartz, white mica, titanite, and epidote in garnet porphyroblasts	S_n is continuous foliation defined by white mica, titanite and quartz , with albite overgrowth		
16TP05D	S_{n-1} is preserved as inclusions in garnet porphyroblasts	S_n defined by fine grained white mica, chlorite, and epidote, and large epidote porphyroblasts, as well as garnet and quartz in "coticule" layer		
16TP08B	S_{n-1} is preserved as inclusions of omphacite, paragonite, white mica, titanite, and epidote in fractured garnet porphyroblasts and closely parallels S_n	S_n defined by glaucophane zoned to actinolite, white mica, epidote and carbonate		
16TP15A		S_n defined by coarse grained white mica and quartz, as well as very fine grained opaques and garnet.	S_{n+1} Is a spaced crenulation axial planar to F_3 that deforms foliation	S_{n+2} is a near vertical crenulation cleavage slightly oblique to S_{n+1}
16TP15B	S_{n-1} is preserved as inclusions in garnet porphyroblasts	S_n is defined by fine grained epidote, chlorite, white mica, and layers and pods of carbonate and quartz. Sn is warped by intrafolial isoclinal folds		
16TP15D	S_{n-1} is defined by white mica, in quartz rich microlithons, oblique to the dominant foliation	S_n defined by very fine grained white mica cleavage domains and medium grained white mica, with quartz microlithons		

Structure

Structure:	S_1	S_2	S_3	S_4
16TP16A		S_n defined by white mica, quartz, and chlorite	S_{n+1} Is a spaced crenulation that deforms foliation	S_{n+2} is a near vertical crenulation cleavage slightly oblique to S_{n+1} and is difficult to discern in thin section
16TP17B	S_{n-1} is defined by inclusions of quartz, epidote, and white mica in partially to fully replaced porphyroblasts	S_n defined by white mica, quartz, and chlorite		
16TP19A	S_{n-1} is preserved as inclusions of white mica and epidote in garnet porphyroblasts	S_n defined by white mica, epidote, and chlorite	S_{n+1} difficult to discern in thin section, spaced crenulation	
16TP21A	S_{n-1} is likely preserved as white mica that are oblique to Sn	S_n defined by white mica, quartz, chlorite, and epidote		
16TP22A	S_{n-1} is preserved in albite and partially to fully replaced garnet porphyroblasts, as well as in white mica rich cleavage domains where grains are oriented oblique to Sn	S_n is continuous foliation defined by white mica, quartz, and chlorite		
16TP24A		S_n defined by white mica, chlorite, quartz, opaques, epidote, and carbonate and is folded about F_2 intrafolial isoclinal folds		
16TP24B	S_{n-1} is preserved as inclusions in partially to fully replaced garnet porphyroblasts	S_n is defined by fine grains of white mica, chlorite, epidote, quartz, and large chlorite-garnet porphyroblasts		
16TP26A	S_{n-1} is preserved in quartz-rich microlithons as white mica grains that are oblique to foliation	S_n defined by white mica and quartz		
16TP27A	S_{n-1} is defined by inclusions in garnet porphyroblasts	S_n defined by white mica, chlorite, carbonate, titanite, epidote, and quartz, with amphibole overgrowth		

Table 3-3: Modal mineralogy based on observations made in thin section

Sample Number	Quartz	White Mica	Chlorite	Calcite	Plagioclase	Epidote	Garnet	Actinolite	Glaucophane	Other	Comments
16TP03A	40%	25%	3%		< 5%	< 5%	13%	<2%		< 3% Tourmaline, <3% Magnetite	Actinolite is only locally preserved, defining crenulated foliation
16TP04B	< 5%	22%	25%		< 5%	25%	15%			< 5% Opaques(magnetite/pyrite)	Fine grained with the exception of garnet porphyroblasts
16TP05B	30%	20%	7%		25%		15%	3%		7% Titanite, <3% pyrite, < 1% apatite and zircon	Possible shearing related to chloritization of garnets
16TP05D	15%	10%	20%	< 5%	< 5%	30%	10%	4%		< 4% magnetite and pyrite	Pseudomorphing of garnets near contact of quartz-rich layer with host
16TP08B	< 5%	8%		< 5%		20%	20%	15%	25%	< 2% Titanite, <1% zircon	Paragonite and Omphacite (< 1%) preserved as inclusions in garnet
16TP15A	35%	40%					15%		10%	< 5% magnetite and pyrite	Gln is not oriented relative to the c-axis
16TP15B	8%	12%	20%	20%	< 2%	25%	8%			< 5% opaques	Intrafolial folds are axial planar to Sn in thin section and hand sample
16TP15D	30%	35%	< 6%	< 5%	< 4%		15%			< 4% opaques	Rotated carbonate porphyroblasts give weak indication of shear
16TP16A	25%	35%	10%	10%			10%			< 3% Tourmaline, < 3% Magnetite, < 5% rutile and titanite	Four separate foliations observed in sample
16TP17B	35%	30%	20%			10%	< 5%			< 5% magnetite and pyrite	Garnets are partially to fully altered to chlorite pseudomorphs
16TP19A	< 5%	25%	30%		< 5%	25%	10%				
16TP21A	55%	20%				12%	7%			< 3% tourmaline, < 3% illmenite and magnetite, < 1% zircon	Tourmaline have core to rim structures
16TP22A	40%	25%	10%		10%	< 5%	< 5%			< 5% opaques	Pseudomorphed garnets give dextral shear sense
16TP24A	< 5%	20%	20%	16%		25%	10%			< 4% opaques	S_{n+1} spaced crenulation deforms intrafolial folds
16TP24B	20%	15%	25%		<2%	25%	<10%			< 3% opaques	Relict garnet cores and sigma clast tails indicate shear
16TP26A	45%	35%			<2%	<5%	10%			< 3% illmenite and magnetite	S_{n-1} preserved in quartz-rich microlithons
16TP27A	5%	15%	5%	<5%		25%	15%			25% amphibole, <5% rutile and titanite	Amphibole overgrows Sn and is not distinctly oriented

Table 3-4: Summary of $^{40}Ar/^{39}Ar$ data for samples examined in this research. PA: plateau age, MSWD: mean square weighted deviates, IA: integrated age. Mineral abbreviations: ACT: actinolite, GLN: glaucophane, TUR: tourmaline, WM: white mica.

Sample	Northing	Easting	Description	Aliquot	PA (Ma)	1σ Error (Ma)	$\%^{39}Ar$	MSWD	Minimum age	1σ Error (Ma)	TFA (Ma)	1σ Error (Ma)
16TP03A	4967384	696149	Pelitic Schist	TUR					309.8	5.4	1264.9	5.2
				WM1	458.9	2.4	79.5	2.1	445.3	8.2	460.3	1.9
				WM2					435.2	5.5	460.3	1.6
16TP04B	4967378	696280	Felsic Gneiss	WM1	459.9	3.3	100	1.08	444.8	7.9	459.2	3.2
16TP05BA	4967288	696174	Pelitic Schist	ACT					579.5	63.7	887.3	9.1
				WM1	466.2	2.7	78.8	1.02	419	19.2	465.2	2.3
16TP05D	4967288	696174	Felsic Gneiss	WM1	463.7	2.6	96.9	1.5	444.8	8.6	464.2	2.4
16TP08B	4967406	696200	Blueschist	GLN					418.2	15.1	452.0	3.9
				GLN2					417.2	6.3	467.6	2.5
				WM1	484.6	4.7	62.8	1.5	471.8	7.5	495.7	4.2
				WM2	455.6	5	100	1.5	408.3	27.3	453.9	5.5
16TP15A	4963604	693597	Pelitic Schist	WM1	461.8	2.1	84.9	1.3	449.5	9.9	463.9	1.7
16TP15D	4963552	693669	Pelitic Schist	WM1	464.7	3.6	82.8	1.6	443.8	13.3	474.5	3.3
16TP16A	4967182	696462	Pelitic Schist	TUR					791.7	5.1	1193.6	4.3
				WM1	461.0	2.9	100	0.84	445.3	13.8	462.8	2.9
16TP17B	4967188	696436	Felsic Gneiss	WM1					403.9	6.8	446.3	2.2
16TP19A	4963132	694117	Felsic Gneiss	WM1	465.9	2.5	96.9	0.61	455.7	18.5	467	2.2
16TP21A	4968198	696236	Hazens Notch Fm.	WM2	453.2	2.3	87	0.73	427.4	17.4	455.5	1.9
16TP22A	4966927	698692	Felsic Gneiss	WM1	454.0	2.7	97	1.7	428.1	12.97	453.4	2.9
16TP24A	4964035	694524	Blueschist	WM1	464	2.9	95.6	0.44	454.7	8.1	466.1	2.6
16TP26A	4965054	694048	Hazens Notch Fm.	WM1	480.5	3.3	86.1	1.1	384.6	22.3	479.6	2.9
				WM2	469.7	3.5	79.8	1.3	419	16.8	463	3

CHAPTER 4: DISCUSSION

4.1 Introduction

Previous researchers obtained plateau ages from white mica and total gas ages from amphibole and white mica to attempt to determine the timing of peak metamorphism of the high-pressure rocks of the TPC (Laird *et al.*, 1984; Pidgeon, 2017; Gonzalez *et al.*, 2018). However, the timing of distinct structural and metamorphic events has never been examined in detail prior to this study. The data presented in here document the relative timing of four structural events in the TPC. When integrated with results from $^{40}Ar/^{39}Ar$ step heating, the combined data constrain the timing of prograde–peak metamorphism and later retrograde events.

To determine if an age of a sample relates to the timing of crystallization at high-pressure conditions or a later cooling age, the P-T conditions of formation must be understood (Warren *et al.*, 2012). With P-T conditions of formation, it is possible to estimate the closure temperature of the mineral examined. White mica may form over a variety of conditions; the effective closure temperature of muscovite is 300–400°C, and phengite may have a closure temperature closer to 600°C (Reiners and Brandon, 2006; Schmidt and Poli, 2003). In the TPC, phengitic white mica and omphacite inclusions in garnet are likely related to similar phase used for estimates for high-pressure, approaching ultrahigh-pressure, facies metamorphic conditions (≤ 2.5 GPa, 510°C; Honsberger, 2015; Gonzalez *et al.*, 2018). In addition, Mg-poor white mica, titanite, and glaucophane are interpreted to represent retrograde metamorphic overprinting (≤ 1.3 GPa, 450°C; Laird *et al.*, 1993, 2013).

4.2 Early (D_1) Deformation

4.2.1 Microstructures Related to Early (D_1) Deformation

The oldest observed foliation, S_1, is preserved as inclusions within garnet porphyroblasts (Figure 3-2) and as a crenulated foliation defined by phengitic white mica, oblique to the dominant S_2 foliation (Figure 3-2). EDS spot analyses on individual inclusions within garnets in blueschist identified high-pressure mineral inclusions of glaucophane, omphacite, titanite, and paragonite, which suggests that S_1 is associated with a prograde mineral assemblage. Therefore, D_1 deformation is inferred to be associated with prograde–peak metamorphism of the rocks of the TPC.

4.2.2 Timing of Early Deformation (D_1)

The earliest ages examined in this study are from samples in or near the center of the TPC, including those that preserve S_1. Sample 16TP08B, a garnet bearing blueschist, yields a plateau age of 484.6 ± 4.7 Ma from WM-1, phengitic white mica, which is interpreted to be a part of the early assemblage. The minimum apparent age of 471.8 ± 7.5 Ma likely coincides with the timing that Mg-bearing phengitic white mica defining S_1 was partially recrystallized during D_2. The second aliquot dated from this sample, WM-2, yielded a plateau age of 455.6 ± 5 Ma. This spectra shows a distinct age gradient of younger ages to older as the temperature is increased past the first ~20% of ^{39}Ar released. This age gradient and younger plateau are likely associated with dating a mixed population of white mica, as well as later deformation related to the formation of S_2 and the retrograde metamorphic overprint. Glaucophane from 16TP08B did not yield plateau

ages, however integrated total gas ages are 452 ± 3.9 Ma and 467.6 ± 2.5 Ma. Petrologic evidence indicates that glaucophane formed during the retrograde path in these samples, and total gas ages closely coincide with the formation of S_2 in samples. However, these ages may be impacted by the zoning of glaucophane to actinolite from core to rim.

Sample 16TP26A, a mica schist of the Hazens Notch Formation, yields a plateau age of 480.5 ± 3.3 Ma from WM-1; white mica that defines S_1 foliation in quartz microlithons. Younger apparent ages and a minimum apparent age of 434.8 ± 17.6 Ma from this analysis indicate that in the schist S_2 and later deformation had an impact on the recrystallization of early white mica or that a mixed population of white mica was dated. An additional plateau age from WM-2 of 469.7 ± 3.5 Ma is likely closely related to the timing of S_2 development, which is the dominant fabric element in the sample.

4.3 D_2 Deformation

4.3.1 Microstructures Related to D_2 Deformation

The dominant foliation in the field area, S_2, is defined by greenschist- and, locally, blueschist-facies minerals. Most outcrops that are mapped geographically as blueschist are retrogressed to an assemblage where S_2 is defined primarily by white mica, chlorite, and epidote. These observations suggest that S_2 formed during exhumation from peak metamorphic conditions.

Garnet porphyroblasts that contain S_1 foliation as inclusion trails are rotated and indicate predominantly top-to-the-E shear sense. In addition, carbonate boudins in blueschist give a variable shear sense. Within carbonate boudins, deformation twinning

of calcite and evidence for subgrain rotation recrystallization is present. In thin sections, the dominant mechanism by which quartz is recrystallized appears to be grain boundary migration. In addition, subgrain rotation recrystallization microstructures are present in most samples. Grain boundary area reduction has a light impact on most samples, and bulging is apparent dominantly in samples with S_3 overprinting.

It is possible to infer that grain boundary migration in quartz records the conditions of S_2 formation. Previous work estimates that the temperatures of metamorphism of the TPC are between 360–520°C (Laird and Albee, 1981; Laird *et al.*, 1993, 2013; Honsberger, 2015). This likely also coincides with the temperatures that S_2 formed, indicated by quartz microstructures.

In thin section and BSE imagery, zoning of garnet, epidote, and amphibole indicates multiple phases of mineral growth. Laird *et al.* (1993) interpreted that the growth of actinolite rims on glaucophane was an Acadian overprint. The data presented here suggests that the timing of this growth is likely Salinic.

4.3.2 Timing of D_2 and Exhumation of the TPC

Exhumation of rocks of the TPC is related to progressive deformation and S_2 development that is associated with intrafolial folding, the formation of boudins and mineral stretching lineations, and the rotation of garnet porphyroblasts. Kinematic indicators in thin section give a predominantly top-to-the-E shear sense.

To address the timing of foliation formation, we chose to examine multiple minerals from within a single sample. Sample 16TP05BA, a sample of pelitic schist intercalated within blueschist, yielded a white mica plateau age of 466.2 ± 2.7 Ma and a

U-Pb age of titanite of 460 ± 17 Ma (2σ). However, actinolite dated from the sample released very little ^{39}Ar, and the apparent age spectra and inverse isochron produced anonymously old ages, given the geologic context. Similarly, analyses on tourmaline that was obtained from sample 16TP03A and 16TP16A resulted in detrital total gas ages (1264.9 ± 5.2 Ma and 1193.6 ± 4.3 Ma, respectively).

The timing of D_2 deformation is constrained between 471–456 Ma by plateau ages of white mica, as well as a U-Pb age of titanite. Greenschist- and, locally, blueschist-facies metamorphic mineral assemblages define S_2 foliation in all samples. Plateau ages of samples with little to no development of S_3 or S_4 crenulations give the tightest bracket of D_2 ages around 466–461 Ma. Within these plots, apparent minimum ages are often Silurian. Samples with younger plateau ages (16TP21A: 453.2 ± 2.3 Ma; 16TP22A: 454 ± 2.7 Ma; Figure 3-6) are proximal to the boundary of the TPC in the felsic gneiss and Hazens Notch Formation and likely are related to the continued formation of S_2 foliation and the emplacement of the TPC. These ages may also be related to the timing of faulting along the boundary of the TPC with the Hazens Notch Formation.

We bracket the timing of D_2 deformation to occur over this ~15 Myr range from 471–456 Ma given the ages of samples calculated in this research, with relation to prior research on the timing of Taconian metamorphism (Laird *et al.,* 1984, 1993, Tremblay and Pinet, 2016). Of all nineteen total glaucophane and white mica aliquots investigated in this study, ~70% yielded a plateau age that falls in this range. This range is further supported by plateau ages from additional research that include: 458.6 ± 2 Ma and 457.6

±1.8 Ma (Figure 1-15; 16PR08A; Tam *et al.,* 2018), 462.8 ± 1.4 Ma (Figure 1-15; 15EP03A; Pidgeon, 2017), and 466.6 ± 1.5 Ma (Figure 1-15; 15EP12A; Pidgeon 2017). In each of these samples, S_2 is the dominant foliation element (Tam *et al.,* 2018; Pidgeon, 2017).

Examining total gas ages on glaucophane from this study gives a minimum age of blueschist-facies retrograde metamorphism. Glaucophane from sample 176TP08B yielded total gas ages of 452.0 ± 3.9 Ma (GLN-1) and 467.6 ± 2.5 Ma (GLN-2). These ages on glaucophane are similar to the total fusion $^{40}Ar/^{39}Ar$ age of 468 ± 6.4 Ma from Laird *et al.* (1984).

To understand the timing of E–W trending intrafolial F_2 folding as a result of progressive deformation during D_2, white mica from 16TP24A, a retrogressed blueschist, was examined. The resultant plateau of 464 ± 2.9 Ma on a plot that is minimally disturbed over the course of the experiment falls closely with other D_2 plateau ages. Apparent ages of steps within the plateau fall within a range of 475–454 Ma, closely coinciding with our estimates for the timing of prolonged D_2 deformation.

To further understand the timing of D_2 deformation in the area surrounding the TPC, age spectra from additional research in the area have been examined (Tam *et al.,* 2018). Tam *et al.* (2018) collected samples from near the boundary of felsic gneiss unit of the TPC and the Hazens Notch Formation that bounds the TPC. Minimum ages from felsic gneiss that do not have D_3 structures (16TP23A and 16PR08A) are: 445.6 ± 5.1 Ma (16TP23A-WM1; Tam *et al.,* 2018) and 451 ± 4.6 Ma and 451.3 ± 7.2 Ma (16PR08A-WM1/WM2; Tam *et al.,* 2018). It is likely that these ages coincide with the continued

formation of S_2 foliation and the faulting that occurred along the boundary of the TPC, which may be analogous to the timing of D_3 deformation within the TPC.

4.4 D_3 Deformation

4.4.1 Microstructures Related to D_3 Deformation

In thin section, D_3 deformation is preserved as a spaced S_3 crenulation cleavage that is axial planar to F_3 folds. S_3 is dominantly preserved in samples of pelitic schist within the TPC samples that have a well-defined S_2 foliation. There does not appear to be significant mineral growth related to the formation of S_3 crenulation.

4.4.2 Timing of D_3 Deformation and the Formation of East–West Trending F_3 Folds

D_3 structures within the TPC include E–W trending F_3 folds and a S_3 spaced crenulation cleavage that deforms the dominant S_2 foliation. Samples 16TP03A, 16TP15A, and 16TP16A, all pelitic schist within blueschist, have well-developed S_3 crenulation cleavages and were examined specifically to investigate the timing of S_3 overprint. Plateau ages in the samples ranged from 458.9–461.8, which overlap with the constraints on the timing of S_2 formation. Minimum apparent ages from sample 16TP03A were 445.3 ± 8.2 Ma and 435.2 ± 5.5 Ma, for WM-1 and WM-2 respectively. Additional minimum ages for these samples are 449.5 ± 9.9 Ma for sample 16TP15A (WM-1) and 445.3 ± 13.2 Ma for sample 16TP16A (WM-1).

In addition to samples of pelitic schist within blueschist that have distinct D_3 structures, similar minimum apparent ages can be found in samples 16TP04B, 16TP05D,

16TP19A, and 16TP24A. These samples are located in the geographically mapped blueschist unit, however have undergone retrograde metamorphic overprinting, and the dominant foliation (S_2) is defined by greenschist-facies minerals and does not have distinct a D_3 overprint. In these samples we interpret plateau ages to represent retrograde metamorphism related to the exhumation of the TPC. Minimum ages of these samples constrain a range of 455–445 Ma for the timing of D_3.

4.4.3 Microstructures Related to D_4 Deformation

In thin section, D_4 deformation is preserved as local retrograde metamorphic overprinting. S_4 is only locally preserved in outcrop and hand sample as a spaced crenulation cleavage axial planar to F_4 folding about the Gilmore Antiform, and is not captured in thin section in this study. Local retrograde metamorphic overprint is related to the pseudomorphing of garnet porphyroblasts to chlorite. Mineral growth related to D_4 deformation is primarily as static overgrowth in the greenschist-facies.

4.4.4 Timing of D_4- Folding about the Gilmore Antiform and Static Retrograde Overprinting

D_4 structures within the TPC include large scale F_4 folding about the NW-trending Gilmore Antiform, a locally apparent spaced crenulation cleavage, and retrograde metamorphic overprinting structures. To investigate the timing of D_4, age spectra from samples that had significant chlorite pseudomorphs after garnet, as well as actinolite and chlorite retrograde overgrowths were examined. Minimum apparent ages from samples constrain a timing of local retrograde metamorphic overprint, associated

with folding about the Gilmore Antiform, record the timing of D_4 to be between ~435–405 Ma.

Glaucophane from blueschist (16TP08B) of the TPC has glaucophane to actinolite core to rim zoning. Apparent minimum ages from aliquot 1 (GLN-1) aliquot 2 (GLN-2) of the analyses were 418.2 ± 15.1 Ma and 417.2 ± 6.3 Ma, which is likely related to the timing of actinolite rim growth on glaucophane cores during the Salinic Orogeny. Additionally, the second aliquot of white mica (WM-2) from 16TP08B yields a minimum age of 408.3 ± 30.9 Ma.

Sample 16TP05BA, a pelitic schist intercalated within blueschist, has actinolite and chlorite that overgrow the dominant foliation, as well as chlorite pseudomorphs after garnet. White mica from sample 16TP05BA yielded a plateau age of 466.2 ± 2.7 Ma and a minimum age of 419 ± 19.2 Ma. We infer that the minimum age is related to Ar loss during the metamorphic episode in which chlorite replaced garnet *via* static recrystallization and the growth of actinolite and chlorite elsewhere in thin section.

4.5 Summary of Timing of Deformation in the TPC

We infer that the timing of prograde–peak metamorphism related to blueschist–eclogite-facies metamorphism of the Tillotson Peak Complex is ~485–480 Ma. This is indicated by plateau ages of phengitic white mica in blueschist and pelitic schist. Later metamorphism, related to the exhumation of the TPC and D_2 deformation occurred at around 471–455 Ma. Samples with the least amount of D_3 and later overprinting structures have a range of plateau ages of 466–459 Ma. After exhumation from mantle depths, F_3 folding that defined the map-scale pattern of the TPC occurred at ~455–445

Ma. Given E–W trending fold axes related to F_2 and F_3 folds, the associated L_2 stretching lineation, and the timing of D_2/D_3; it is possible that D_3 in the TPC is a continuation of D_2. The fourth phase of deformation (D_4) that resulted in folding about the Gilmore Antiform and retrograde static overprinting occurred from ~435–405 Ma. At this time, there is minimal evidence for an additional event at ~385–370 Ma.

4.6 Limited evidence for Acadian overprinting of the TPC

The original interpretation for the timing of folding about the Gilmore Antiform and the associated retrograde metamorphic overprint was that they are Acadian in age (Laird *et al.,* 1984, 1993). However, in this study we find very few Acadian age signatures in samples studied. In one sample of Hazens Notch Formation schist from the core of the TPC, we find a minimum apparent age of 384.6 ± 22.3 Ma (16TP26A-WM1). Sample 16TP23A, a sample of felsic gneiss from the boundary of the TPC, also has an Acadian minimum age signature (Tam *et al.,* 2018). In this sample, Tam *et al.,* (2018) find an apparent minimum age of 370.3 ± 21.6 Ma. Neither sample have well-defined evidence for S_3 or S_4 foliation (Tam *et al.,* 2018). Therefore, it is difficult to interpret what these age signatures represent.

4.7 Tectonic Implications

The timing of prograde–peak metamorphism of the TPC appears to closely coincide with the timing of early metamorphism of the Belvidere Mountain Complex and Ophiolites in Quebec (505–473 Ma; Laird *et al.,* 1993; Castonguay *et al.,* 2012; Tremblay and Pinet, 2016 and references therein). Ages of 485–480 Ma in the TPC likely

only constrain a minimum age of peak high-pressure metamorphism, as most samples are at least partially recrystallized during subsequent retrograde metamorphism.

Structures examined in the field, combined with microstructure and $^{40}Ar/^{39}Ar$ age data, give a range of ~471–456 Ma for the dominant phase of exhumation (D_2) of the TPC, which is related to the primary pulse of Taconian metamorphism in Vermont (470–456 Ma; Castonguay *et al.*, 2012; Laird *et al.*, 1984). Petrologic modeling by Honsberger (2015) and the geochronologic constraints for late-stage (M_4) metamorphism related to folding about the Gilmore Antiform are evidence that the TPC was likely near the surface prior to the Acadian Orogeny, which has little impact on the rocks of the TPC.

One of the questions that has been posed for the formation of the TPC is related to the mechanism by which F_3 E–W trending folds originated. Original interpretations were due to interference by E–W graben structures in the underlying basement (Cady *et al.*, 1963), oblique collision towards a relict failed arm (Doolan *et al.*, 1982), rotational fold thrusting caused by large included masses (e.g., Belvidere Mountain Complex; Bothner and Laird, 1987), or possibly the formation of lineation parallel folds during exhumation (cf. Little *et al.*, 2007). While it is difficult to pinpoint the exact mechanism of formation of these folds, we note that the timing of D_3 in the TPC is closely related to the timing constraints for the collision of the Moretown Terrane with the Laurentian margin in southern New England (Karabinos *et al.*, 2017).

Folding about the Gilmore Antiform and greenschist-facies overprinting, originally attributed to the Acadian Orogeny (Bothner and Laird, 1987; Laird *et al.*, 1993), may be related to the multi-phase Salinic tectonic event (e.g., Tremblay and Pinet,

2016). This is supported in the TPC by few geochronologic signatures that indicate Acadian overprinting (Figure 4-1).

It is important to note that previous researchers interpreted that the age of the Taconian suture zone in Vermont dated at 505–473 Ma is related to exhumation and cooling of these rocks (505–473 Ma; Laird *et al.,* 1984, 1993; Castonguay *et al.,* 2012). In addition, it has been interpreted that ages of 471–460 (Laird *et al.,* 1984; 1993; Tremblay and Pinet, 2016) strictly represent ages of cooling below metamorphic temperatures (Karabinos *et al.,* 2017). In the TPC, this question is addressed by comparing the ages of multiple mineral phases and the relative chronology of structures observed to determine that D_1 (485–480 Ma) is associated with prograde–peak metamorphic conditions, and that D_2 (471–456 Ma) is related to exhumation.

Due to the pressures and temperatures (≤ 2.5 GPa, 510°C; Honsberger, 2015; Gonzalez *et al.,* 2018) estimated to be related to the peak metamorphism of the TPC, it is difficult to relate the ages determined to cooling ages after metamorphism. We interpret that the peak assemblage of the TPC included phengitic white mica, and that actinolite, glaucophane, titanite, and white mica grew during retrograde metamorphism. Ages of phengite from 16TP26A, a sample of Hazens Notch Schist, and phengite from 16TP08B, a glaucophane-bearing blueschist, define a range of c. 485–480 Ma. $^{40}Ar/^{39}Ar$ Plateau ages from white mica and a U-Pb age of titanite give a range of ~471–456 Ma for the timing of retrograde metamorphism associated with exhumation of the TPC. Low-pressure estimates from prior research (0.9 GPa, 360°C–1.1 GPa, 470°C; Laird and Albee, 1981; Laird *et al.,* 1984, 1993) likely represent the conditions that rocks of the

TPC experienced during D_2. Therefore, the effective closure temperature range of white mica for $^{40}Ar/^{39}Ar$ geochronology (Reiners and Brandon, 2006) suggests that the age of 471–456 is a recrystallization age.

The Hazens Notch Formation is mapped to bound the TPC on all sides, and is also mapped in the center of the TPC (Figure 3-1). Previous and related geochronology on white mica from the Hazens Notch Formation suggests that the timing of metamorphism was 456–435 Ma (Laird *et al.*, 1984; Castonguay *et al.*, 2012; Tam *et al.*, 2018). However, an aliquot of white mica from a sample of Hazens Notch Formation in the TPC gave an age of 480.5 ± 3.3 Ma (Figure 3-6o). This suggests that either the rocks of the Hazens Notch Formation schist found within the TPC were not heavily impacted by later deformation, or the Hazens Notch Formation in the TPC may not be exactly analogous to the Hazens Notch Formation mapped outside of the TPC.

4.8 Future Work

To further understand the timing of deformation in the TPC, we must constrain the timing of peak metamorphism within the subduction zone. This research and additional work in the TPC by Gonzalez *et al.* (2018) suggests that prograde–peak metamorphism of the TPC occurred at 485–480 Ma. The observation of zircon, titanite, and paragonite as inclusions in garnets within blueschist suggests these minerals may have been a part of the peak (eclogite-facies?) assemblage. Further examination of these phases *in situ* may refine this age range for M_1, as some white mica plateau ages from high-pressure rocks of the TPC appear to have mixed ages (e.g., McDougall and Harrison, 1999). However, this method of examining the potential age of M_1 in the TPC

must be approached with caution as titanite examined within blueschist had too little U for proper age determination.

The method by which the TPC was exhumed has yet to be determined. Prior researchers have discussed the exhumation of the TPC within a lubricated channel (Thompson and Thompson, 2003; Honsberger, 2015), through back-thrusting and later normal faulting (Tremblay and Pinet, 2016), and in a tectonic wedge (Lamon, 2001). More recently researchers that have been examining the role of the Prospect Rock Fault and Burgess Branch Fault Zone in exhuming the TPC have yet to reach a firm conclusion (Tam *et al.,* 2018; Gonzalez *et al.,* 2018). Gonzalez *et al.* (2018) interpret that Salinic normal faulting along the Burgess Branch Fault Zone aided in the exhumation of the TPC, but was not the dominant driving force.

Within the TPC, the relative orientation of D_2-D_3 structures leads to the interpretation that the mechanism by which the TPC was exhumed must allow for the exhumation of a coherent slice of high-pressure material. Kinematic indicators give dominantly a top-to-the-E, with a single top-to-the-W, shear sense. To further understand the mechanism by which these rocks were exhumed, a more detailed study of shear sense indicators throughout the complex is necessary.

In this research, we determine that the exhumation of the TPC from mantle (~70 km) to mid-crustal (~10 km) levels occurred for upwards of 15 Myr (471–456 Ma). If Honsberger's (2015) estimate of ~10 Myr for exhumation is accurate, this allows for the interpretation that exhumation of high-pressure rocks of the TPC occurred at a rate of 4.7–6.0 mm/yr.

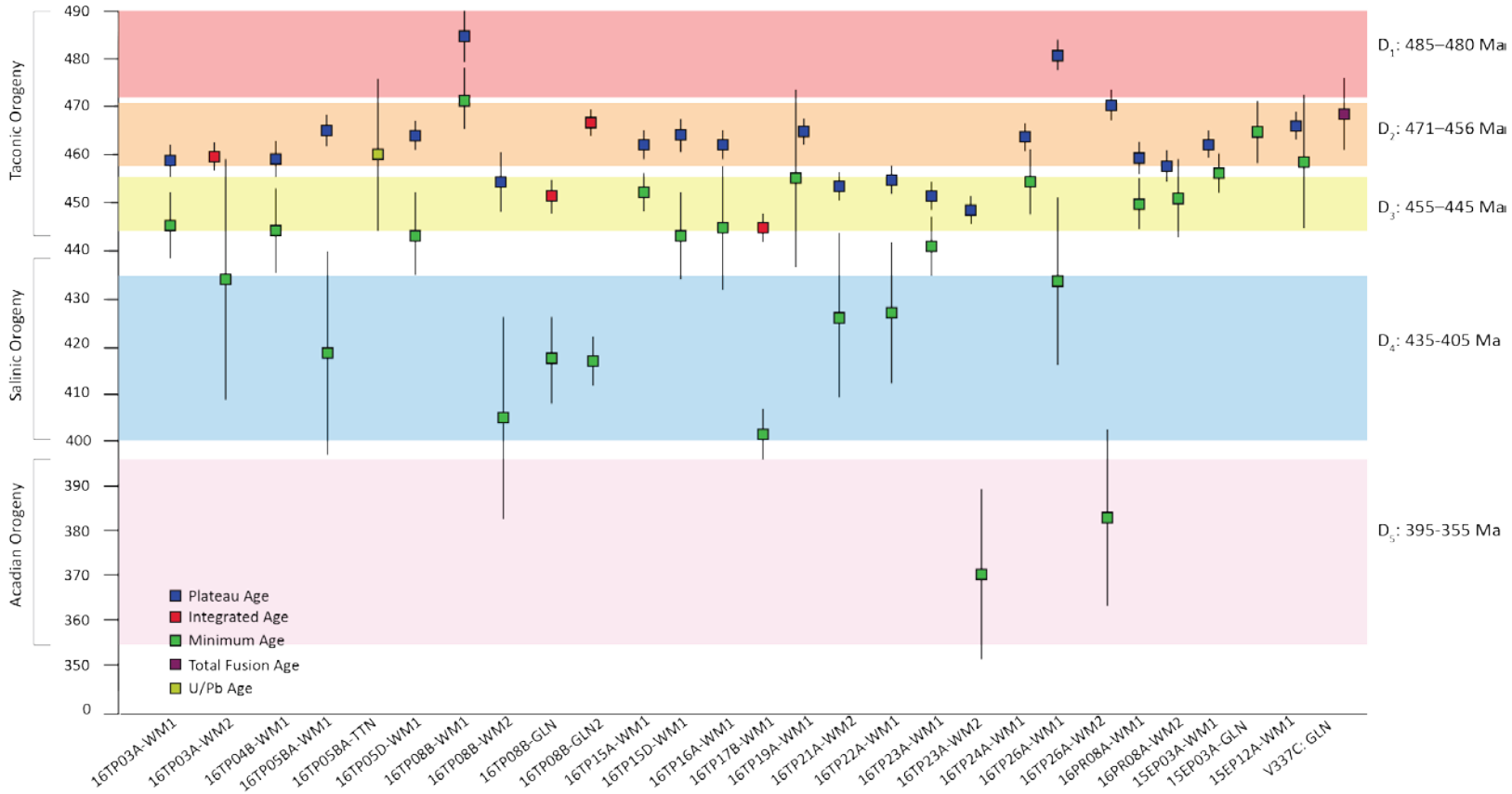

Figure 4-1: Ages from this study and others (Laird *et al.*, 1984; Pidgeon, 2017; Tam *et al.*, 2018) for the rocks of the TPC that show the correlation of ages examined with the Taconic, Acadian, and Salinic Orogenies. Plateau, minimum, and integrated ages from this study as well as Pidgeon (2017) and Tam *et al.* (2018) are plotted with 1σ error bar. U-Pb age from this study is plotted with 2σ error bar.

CHAPTER 5: CONCLUSIONS

The metamorphic rocks that compose the Tillotson Peak Complex preserve a complex tectonic history that record metamorphism and deformation from the timing of formation in the Cambrian through the most recent metamorphic overprinting in the Devonian. Four distinct deformation events have impacted the rocks of the TPC with resultant structures identified in thin section and in outcrop. $^{40}Ar/^{39}Ar$ age spectra from the TPC from this study have been compared with additional research on the TPC (Laird *et al.*, 1984, 1993; Bothner and Laird 1987, 1999; Honsberger, 2015) and the region (Thompson and Thompson 2003; Kim *et al.*, 2003; Tremblay and Pinet, 2016; Tam *et al.*, 2018) to understand the timing of exhumation and deformation of high-pressure rocks in northern Vermont.

Estimates for the timing of prograde to peak metamorphism (D_1) from 485 to 480 are derived from samples associated with high-pressure inclusions in garnet porphyroblasts and S_1 foliation defined by white mica in S_2 quartz-rich microlithons. These ages closely coincide with prior estimates for the timing of peak metamorphism of amphibolite in the Belvidere Mountain Complex and ophiolites in Quebec and Newfoundland (Laird *et al.*, 1984, 1993; Castonguay *et al.*, 2012; Tremblay and Pinet, 2016). Using this evidence, we infer that the oldest plateau ages obtained from the TPC are indicative of metamorphism occurring during early Taconian convergence at ~505–486 Ma (Laird *et al.*, 1984, 1993; Castonguay *et al.*, 2012). The subduction zone metamorphism related to D_1 of rocks of the TPC occurred during the prograde–peak metamorphic pathway of these rocks at conditions that were approaching the quartz-

coesite transition zone for ultrahigh-pressure metamorphism (Honsberger, 2015; Gonzalez *et al.,* 2018).

In the TPC, exhumation of high-pressure rocks is related to the formation of D_2 structures including E–W trending mineral stretching lineations, isoclinal intrafolial E–W-trending folds, and local kinematic indicators. When the mineral assemblage defining S_2 foliation is compared to that which defined S_1 in garnet porphyroblasts, it is apparent that D_2 deformation occurred during retrograde blueschist–greenschist-facies metamorphism. The exhumation of the TPC is associated with the timing of regional Taconian metamorphic ages in Vermont of ~471–456 Ma (Laird *et al., 1984*; Pidgeon, 2017; Tam *et al.,* 2018). Exhumation of rocks of the TPC was previously estimated to occur over the course of 10 Myr from ~70 km depth to mid-crustal levels (~10 km; Honsberger, 2015). The plateau ages we present suggest exhumation could have occurred for upwards of 15 Myr (471–456 Ma). These data give an estimated range of for the exhumation of high-pressure rocks of 4.7–6.0 mm/yr.

Minimum apparent ages in $^{40}Ar/^{39}Ar$ age spectra with samples that have been recrystallized during D_3 development suggest that map-scale F_3 folds formed during retrograde metamorphism at ~ 455–445 Ma. This timing is associated with the collision of the Moretown Terrane in southern New England (Karabinos *et al.,* 2017).

Folding about the Green Mountain Anticlinorium in Vermont and the Sutton-Notre Dame Mountain Anticlinorium in Quebec is interpreted to have occurred during the Acadian Orogeny (~390–355 Ma; Laird *et al.,* 1984; Castonguay *et al.,* 2012; Tremblay and Pinet, 2016). In the TPC, this phase of metamorphism is interpreted to be

related to the formation of the NW–SE trending Gilmore Antiform as well as local retrograde overprinting (Cady *et al.,* 1963; Laird *et al.,* 1993). Minimum apparent ages of ~435–405 Ma from $^{40}Ar/^{39}Ar$ age spectra suggest limited deformation occurred during the Salinic Orogeny. Our research and collaborative projects (Gonzalez *et al.,* 2018; Tam *et al.,* 2018) indicate that movement along the Burgess Branch Fault may be related to Silurian normal faulting in Quebec (Tremblay and Pinet, 2016). Few white mica analyses yield apparent minimum ages in the Acadian, and therefore we infer F_4 folding and retrograde overprinting in the TPC to have occurred during the Salinic. Though previous workers have suggested the greenschist-facies metamorphic overprint of the TPC is Acadian, this work demonstrates rather that the primary phase greenschist-facies metamorphism is related to D_2 exhumation and a secondary phase of greenschist-facies metamorphism is locally associated with Salinic overprinting. Acadian age signals in the TPC in the data presented here are limited.

COMPREHENSIVE BIBLIOGRAPHY

Agard, P., Yamato, P., Jolivet, L. and Burov, E., 2009. Exhumation of oceanic blueschists and eclogites in subduction zones: timing and mechanisms: Earth-Science Reviews, v. 92, no. 1–2, p. 53–79, doi: 10.1016/j.earscirev.2008.11.002.

Andersen, T.B., Jamtveit, B., Dewey, J.F. and Swensson, E., 1991. Subduction and eduction of continental crust: major mechanisms during continent-continent collision and orogenic extensional collapse, a model based on the south Norwegian Caledonides: Terra Nova, v. 3, no. 3, p. 303–310, doi: 10.1111/j.1365-3121.1991.tb00148.x.

Augland, L.E., Andresen, A. and Corfu, F., 2010. Age, structural setting, and exhumation of the Liverpool Land eclogite terrane, East Greenland Caledonides: Lithosphere, v. 2, no. 4, p. 267–286, doi: 10.1130/L75.1.

Auzanneau, E., Vielzeuf, D., and Schmidt, M.W., 2006, Experimental evidence of decompression melting during exhumation of subducted continental crust: Contributions to Mineralogy and Petrology, v. 152, p. 125–148, doi: 10.1007/s00410–006–0104–5.

Baldwin, S.L., Webb, L.E. and Monteleone, B.D., 2008. Late Miocene coesite-eclogite exhumed in the Woodlark Rift: Geology, v. 36, no. 9, p. 735–738, doi: 10.1130/G25144A.1.

Bea, F., Pesquera, A., Montero, P., Torres-Ruiz, J. and Gil-Crespo, P.P., 2009. Tourmaline $^{40}Ar/^{39}Ar$ chronology of tourmaline-rich rocks from Central Iberia dates the main Variscan deformation phases: Geologica Acta: an international earth science journal, v. 7, no. 4, doi: 10.1344/104.000001446.

Bothner, W.A. and Laird, J., 1987. Structure and metamorphism at Tillotson Peak, North-Central Vermont: Guidebook for field trips in Vermont, v. 2, p. 383–405.

Bothner, W.A. and Laird, J., 1999. Geologic map of the Tillotson-Haystack area, Hazens Notch and parts of the Lowell 7.5-minute quadrangles, Vermont: Vermont Geological Survey, Montpelier, Vermont.

Burov, E., Francois, T., Yamato, P. and Wolf, S., 2014. Mechanisms of continental subduction and exhumation of HP and UHP rocks: Gondwana Research, v. 25, no. 2, p. 464–493, doi: 10.1016/j.gr.2012.09.010.

Cady, W.M., Albee, A.L., and Chidester, A.H., 1963, Bedrock geology and asbestos deposits of the upper Missisquoi Valley and Vicinity, Vermont: U.S. Geological Survey Bulletin 1122-B, Contributions to Economic Geology, 78 p.

Castonguay, S., Ruffet, G., Tremblay, A. and Féraud, G., 2001. Tectonometamorphic evolution of the southern Québec Appalachians: $^{40}Ar/^{39}Ar$ evidence for Middle

Ordovician crustal thickening and Silurian–Early Devonian exhumation of the internal Humber zone: Geological Society of America Bulletin, v. 113, p. 144–160, doi: 10.1130/0016-7606(2001)113<0144:TEOTSQ>2.0.CO;2.

Castonguay, S. and Tremblay, A., 2003. Tectonic evolution and significance of Silurian Early Devonian hinterland-directed deformation in the internal Humber zone of the southern Quebec Appalachians: Canadian Journal of Earth Sciences, v. 40, no. 2, p. 255–268.

Castonguay, S., Ruffet, G. and Tremblay, A., 2007. Dating polyphase deformation across low-grade metamorphic belts: An example based on $^{40}Ar/^{39}Ar$ muscovite age constraints from the southern Quebec Appalachians, Canada: Geological Society of America Bulletin, v. 119, no. 7–8, p. 978–992, doi: 10.1130/B26046.1.

Castonguay, S., Kim, J., Thompson, P.J., Gale, M.H., Joyce, N., Laird, J. and Doolan, B.L., 2012. Timing of tectonometamorphism across the Green Mountain Anticlinorium, northern Vermont Appalachians: $^{40}Ar/^{39}Ar$ data and correlations with southern Quebec: Bulletin, v. 124, no. 3–4, p. 352–367, doi: 10.1130/B30487.1

Castonguay, S., van Staal, C.R., Joyce, N., Skulski, T. and Hibbard, J.P., 2014. Taconic metamorphism preserved in the Baie Verte peninsula, Newfoundland Appalachians: Geochronological evidence for ophiolite obduction and subduction and exhumation of the leading edge of the Laurentian (Humber) margin during closure of the Taconic seaway: Geoscience Canada, v. 41, no. 4, p. 459–482, doi: 10.12789/geocanj.2014.41.055.

Cawood, P.A., McCausland, P.J. and Dunning, G.R., 2001. Opening Iapetus: constraints from the Laurentian margin in Newfoundland: Geological Society of America Bulletin, v. 113, no. 4, p. 443–453, doi: 10.1130/0016-7606(2001)113<0443:OICFTL>2.0.CO;2.

Chopin, C., 1984. Coesite and pure pyrope in high-grade blueschists of the western Alps: a first record and some consequences: Contributions to Mineralogy and Petrology, v. 86, no. 2, p. 107–118.

Chu, X., Ague, J.J., Axler, J.A. and Tian, M., 2016. Taconian retrograde eclogite from northwest Connecticut, USA, and its petrotectonic implications: Lithos, v. 240, p. 276–294, doi: 10.1016/j.lithos.2015.10.011.

Clague, D., Rubin, J. and Brackett, R., 1981. The age and origin of the garnet amphibolite underlying the Thetford Mines ophiolite, Quebec: Canadian Journal of Earth Sciences, v. 18, no. 3, p. 469–486, doi: 10.1139/e81-041.

David, J. and Marquis, R., 1994. Géochronologie U–Pb dans les Appalaches du Québec: application aux roches de la zone de Dunnage: La Revue géologique du Québec, v. 1, p. 16–20.

De Souza, S., Tremblay, A., Ruffet, G. and Pinet, N., 2012. Ophiolite obduction in the Quebec Appalachians, Canada—$^{40}Ar/^{39}Ar$ age constraints and evidence for syn-tectonic erosion and sedimentation: Geological Survey of Canada Special Issue: In honour of Ward Neale on the theme of Appalachian and Grenvillian geology: Canadian journal of earth sciences, v. 49, p. 91–110, doi: 10.1139/e11-037.

Dewey, J.F. and Bird, J.M., 1970. Mountain belts and the new global tectonics: Journal of Geophysical Research, v. 75, no. 14, p. 2625–2647, doi: 10.1029/JB075i014p02625.

Doll, C. G., Cady, W. M., Thompson, J. B., Jr., & Billings, M. P., 1961, Centennial geologic map of Vermont: Montpelier, Vt., Vermont Geological Survey, 1 sheet, scale 1:250,000.

Doolan, B.L., Gale, M.H., Gale, P.N., and Hoar, R.S., 1982, Geology of the Quebec Reentrant: possible constraints from early rifts and the Vermont–Quebec serpentine belt. In major structural zones and faults of the northern Appalachians: Geological Association of Canada Special Paper 7, 87–115.

Dunlap, W.J., Hirth, G. and Teyssier, C., 1997. Thermomechanical evolution of a ductile duplex: Tectonics, v. 16, no. 6, p. 983–1000, doi: 10.1029/97TC00614.

Duretz, T., Gerya, T.V. and May, D.A., 2011. Numerical modelling of spontaneous slab breakoff and subsequent topographic response: Tectonophysics, v. 502, no. 1–2, p. 244–256, doi: 10.1016/j.tecto.2010.05.024.

Duretz, T., Gerya, T.V., Kaus, B.J.P. and Andersen, T.B., 2012. Thermomechanical modeling of slab eduction: Journal of Geophysical Research: Solid Earth, v. 117, no. B8: 10.1029/2012JB009137.

Duretz, T. and Gerya, T.V., 2013. Slab detachment during continental collision: Influence of crustal rheology and interaction with lithospheric delamination: Tectonophysics, v. 602, p.124–140, 10.1016/j.tecto.2012.12.024.

Ernst, W.G., 1971. Metamorphic zonations on presumably subducted lithospheric plates from Japan, California and the Alps: Contributions to Mineralogy and Petrology, v. 34, p. 43–59.

Ernst, W.G., 2001. Subduction, ultrahigh-pressure metamorphism, and regurgitation of buoyant crustal slices—implications for arcs and continental growth. Physics of the Earth and Planetary Interiors, v. 127, no. 1–4, p. 253–275, doi: 10.1016/S0031-9201(01)00231-X.

Ernst, W.G., 2010. Subduction-zone metamorphism, calc-alkaline magmatism, and convergent-margin crustal evolution: Gondwana Research, v. 18, p. 8–16, doi: 10.1016/j.gr.2009.05.010.

Eusden, Jr, J.D., Guzofski, C.A., Robinson, A.C. and Tucker, R.D., 2000. Timing of the Acadian orogeny in northern New Hampshire: The Journal of Geology, v. 108, no. 2, p. 219–232.

Federico, L., Crispini, L., Scambelluri, M. and Capponi, G., 2007. Ophiolite mélange zone records exhumation in a fossil subduction channel: Geology, v. 35, no. 6, p. 499–502, doi: 10.1130/G23190A.1.

Feininger, T., 1981. Amphibolite associated with the Thetford Mines ophiolite complex at Belmina Ridge, Quebec: Canadian Journal of Earth Sciences, v. 18, no. 12, p. 1878–1892, doi: 10.1139/e81-174.

Fisher, D. W., Isachsen, Y. W., & Rickard, L. V., 1970, Geologic Map of New York State, consisting of 5 sheets: Niagara, Finger Lakes, Hudson-Mohawk, Adirondack, and Lower Hudson: New York State Museum and Science Service, Map and Chart Series No. 15, scale 1:250,000.

Fleck, R.J., Sutter, J.F. and Elliot, D.H., 1977. Interpretation of discordant $^{40}Ar/^{39}Ar$ age-spectra of Mesozoic tholeiites from Antarctica: Geochimica et Cosmochimica Acta, v. 41, p.15–32, doi: 10.1016/0016-7037(77)90184-3.

Gale, M.H., 1980. Geology of the Belvidere Mountain Complex, Eden and Lowell, Vermont (No. 80-978). US Geological Survey.

Gerya, T.V., Stöckhert, B. and Perchuk, A.L., 2002. Exhumation of high-pressure metamorphic rocks in a subduction channel: A numerical simulation: Tectonics, v. 21, no. 6, doi: 10.1029/2002TC001406.

Gillet, P., Ingrin, J. and Chopin, C., 1984. Coesite in subducted continental crust: PT history deduced from an elastic model: Earth and Planetary Science Letters, v. 70, i. 2, p. 426-436, doi:10.1016/0012-821X(84)90026-8.

Gonzalez, J. P., Baldwin, S. L., Kim, J. J., Webb, L. E., 2018. A Comparison of Pressure-Temperature-Time Histories Across the Burgess Branch Fault Zone, Northern Vermont: Geological Society of America Abstracts with Programs, v. 50, no. 2, doi: 10.1130/abs/2018NE-310874.

Hacker, B.R., Ratschbacher, L., Webb, L., McWilliams, M.O., Ireland, T., Calvert, A., Dong, S., Wenk, H.R. and Chateigner, D., 2000. Exhumation of ultrahigh-pressure continental crust in east central China: Late Triassic-Early Jurassic tectonic unroofing: Journal of Geophysical Research: Solid Earth, v. 105, no. B6, p. 13339–13364.

Hacker, B.R., 2006. Pressures and temperatures of ultrahigh-pressure metamorphism: implications for UHP tectonics and H2O in subducting slabs: International Geology Review, v. 48, no. 12, p. 1053–1066, doi: 10.2747/0020-6814.48.12.1053.

Hacker, B.R., Kelemen, P.B. and Behn, M.D., 2011. Differentiation of the continental crust by relamination: Earth and Planetary Science Letters, v. 307, no. 3–4, p. 501–516, doi: 10.1016/j.epsl.2011.05.024.

Hannula, K. A., Onasch, E., Wertheim, J., Lackey, J. S., Mattox, E., & McGrath, G., 1999. Syntectonic pluton intrusion during contractional deformation: Microstructural evidence from the aureole of the Acadian Victory Pluton, north-eastern Vermont, USA: Journal of Metamorphic Geology, v. 17, p. 271–286.

Hermes, O. D., Gromet, L. P., & Murray, D. P., 1994, Bedrock Geologic Map of Rhode Island: Rhode Island Map Series No. 1, University of Rhode Island, Kingston, scale 1:100,000.

Hirth, G. and Tullis, J., 1992. Dislocation creep regimes in quartz aggregates: Journal of Structural Geology, v. 14, no. 2, p. 145–159, doi: 10.1016/0191-8141(92)90053-Y.

Honsberger, I. W., 2015. Metamorphism, Deformation, Geochemistry, and Tectonics of Exhumed Ultramafic and Mafic Rocks in the Central and North-Central Vermont Appalachians [Ph.D. Dissertation]: University of New Hampshire, 173 p.

Honsberger, I.W., 2015. The dynamics of subduction zone metamorphism and exhumation: insight from polymetamorphosed mafic rocks in the Vermont Appalachians, Geological Society of America Abstracts with Programs, v. 47, no. 7, p. 226

Horodyskyj, U., Lee, C.T.A. and Luffi, P., 2009. Geochemical evidence for exhumation of eclogite *via* serpentinite channels in ocean-continent subduction zones: Geosphere, v. 5, no. 5, p. 426–438, doi: 10.1130/GES00502.1.

Hussey, A.M., Bothner, W.A. and Aleinikoff, J., 2010. The tectono-stratigraphic framework and evolution of southwestern Maine and southeastern New Hampshire: Geological Society of America Memoir, v. 206, p. 205–230.

Jicha, B.R. and Brown, F.H., 2014. An age for the Korath Range, Ethiopia and the viability of $^{40}Ar/^{39}Ar$ dating of kaersutite in Late Pleistocene volcanics: Quaternary Geochronology, v. 21, p. 53–57, doi: 10.1016/j.quageo.2013.03.007

Jourdan, F. and Thern, E., 2014. $^{40}Ar/^{39}Ar$ dating of tourmaline as a tool for high-temperature metamorphism thermochronology: EGU General Assembly Conference Abstracts, v. 16.

Karabinos, P., Samson, S.D., Hepburn, J.C. and Stoll, H.M., 1998. Taconian orogeny in the New England Appalachians: collision between Laurentia and the Shelburne Falls arc: Geology, v. 26, no. 3, p. 215–218, doi: 10.1130/0091-7613(1998)026<0215:TOITNE>2.3.CO;2.

Karabinos, P., Macdonald, F.A. and Crowley, J.L., 2017. Bridging the gap between the foreland and hinterland I: Geochronology and plate tectonic geometry of Ordovician magmatism and terrane accretion on the Laurentian margin of New England: American Journal of Science, v. 317, no. 5, p. 515–554, doi: 10.2475/05.2017.01.

Keppie, J. D., (compiler), 2000, Geological Map of the Province of Nova Scotia, Nova Scotia Department of Natural Resources (NSDNR) Published Map, scale 1: 500,000.

Kim, J., Gale, M., Laird, J., Stanley, R. and Wright, S.F., 1999. Lamoille River valley bedrock transect# 2: Guidebook to field trips in Vermont and adjacent regions of New Hampshire and New York: New England Intercollegiate Geological Conference, v. 91, p. 213–250.

Kim, J., Gale, M., Laird, J., Thompson, P.J. and Bothner, W.A., 2001. Mafic complexes in northern Vermont and Quebec correlatives: Geological Society of America, Abstracts with Programs, v. 33, p. 20.

Kim, J., Coish, R., Evans, M. and Dick, G., 2003. Supra–subduction zone extensional magmatism in Vermont and adjacent Quebec: Implications for early Paleozoic Appalachian tectonics: Geological Society of America Bulletin, v. 115, no. 12, p.1552–1569, doi.org/10.1130/B25343.1.

Kim, J., Gale, M.H., Coish, R. And Laird, J., 2010. Tectonic evolution of the Rowe-Hawley Belt in central and northern Vermont: Geological Society of America Abstracts with Programs, v. 42, no. 1, p. 55.

Korsakov, A.V., Travin, A.V., Yudin, D.S. and Marschall, H.R., 2009, February. 40 Ar/39 Ar dating of tourmaline from metamorphic rocks of the Kokchetav massif, Kazakhstan: Doklady Earth Sciences, v. 424, no. 1, p. 168–170, doi: 10.1134/S1028334X0901036X.

Kossert, K. and Günther, E., 2004. LSC measurements of the half-life of ^{40}K: Applied Radiation and Isotopes, v. 60, no. 2–4, p. 459–464, doi: 10.1016/j.apradiso.2003.11.059.

Kruhl, J. H., 2001. Crystallographic control on the development of foam textures in quartz, plagioclase and analogue material: International Journal of Earth Sciences, v. 90, p.104–117, doi:10.1007/s005310000170.

Kylander-Clark, A.R.C., Hacker, B.R. and Mattinson, J.M., 2008. Slow exhumation of UHP terranes: titanite and rutile ages of the Western Gneiss Region, Norway: Earth and Planetary Science Letters, v. 272, no. 3–4, p. 531–540.

Kylander-Clark, A.R., Hacker, B.R. and Mattinson, C.G., 2012. Size and exhumation rate of ultrahigh-pressure terranes linked to orogenic stage: Earth and Planetary Science Letters, v. 321, p. 115–120, doi: 10.1016/j.epsl.2011.12.036.

Lagor, S.W., 2016. The relationship between magmatism and deformation during the Acadian orogeny: A case study from eastern-central Vermont, [Master's Thesis] University of Vermont, Burlington, Vermont, 170 p.

Laird, J. and Albee, A.L., 1975. Polymetamorphism and the first occurrence of glaucophane and omphacite in northern Vermont: In Geological Society of America Abstracts with Programs, v. 7, p. 1159.

Laird, J. and Albee, A.L., 1981. High-pressure metamorphism in mafic schist from northern Vermont: American Journal of Science, v. 281, no. 2, p. 97–126.

Laird, J. and Albee, A.L., 1981. Pressure, temperature, and time indicators in mafic schist; their application to reconstructing the polymetamorphic history of Vermont: American Journal of Science, v. 281, no. 2, p.127–175.

Laird, J., Lanphere, M.A. and Albee, A.L., 1984. Distribution of Ordovician and Devonian metamorphism in mafic and pelitic schists from northern Vermont: American Journal of Science, v. 284, no. 4–5, p. 376–413.

Laird, J., Trzcienski, Jr., W.E, and Bothner, W.A., 1993. High-pressure, Taconian, and subsequent polymetamorphism of southern Quebec and northern Vermont. Contribution - Geology Department, University of Massachusetts, Boston, Massachusetts, p. 1–32.

Laird, J., Bothner, W.A., Thompson, P.J., Thompson, T., Gale, M. and Kim, J., 2001. Geochemistry, petrology, and structure of the Tillotson Peak and Belvidere Mountain mafic complexes, northern Vermont: Geological Society of America Abstracts with Programs, v. 33, p. A59.

Laird, J. and Honsberger, I.W., 2013. Taconian subduction: pressure, temperature paths preserved in metamorphosed mafic rocks from northern Vermont and adjacent Quebec: Geological Society of America Abstracts with Program, v. 45, p. 106.

Lamon, T. C., 2001. Tectonic wedging in the northern Vermont Appalachians: an emplacement model for the albitic core rocks of the Green Mountain Anticlinorium [Masters' Thesis]: University of Vermont, 253 p.

Lee, J. Y., Marti, K., Severinghaus, J. P., Kawamura, K., Yoo, H. S., Lee, J. B., & Kim, J. S., 2006, A redetermination of the isotopic abundances of atmospheric Ar: Ceochimica et Cosmochimica Acta, v. 70, p. 4507–4512.

Li, J., Gao, J. and Wang, X., 2016. A subduction channel model for exhumation of oceanic-type high-pressure to ultrahigh-pressure eclogite-facies metamorphic rocks in SW Tianshan, China: Science China Earth Sciences, v. 59, no. 12, p. 2339–2354, doi: 10.1007/s11430-016-5103-7.

Liou, J.G., Tsujimori, T., Zhang, R.Y., Katayama, I. and Maruyama, S., 2004. Global UHP metamorphism and continental subduction/collision: the Himalayan model: International Geology Review, v. 46, p. 1–27, doi: 10.2747/0020-6814.46.1.1.

Little, T.A., Baldwin, S.L., Fitzgerald, P.G. and Monteleone, B., 2007. Continental rifting and metamorphic core complex formation ahead of the Woodlark spreading ridge,

D'Entrecasteaux Islands, Papua New Guinea: Tectonics, v. 26, doi: 10.1029/2005TC001911.

Lloyd, G.E. and Freeman, B., 1994. Dynamic recrystallization of quartz under greenschist conditions: Journal of Structural Geology, v.16, no. 6, p. 867–881, doi: 10.1016/0191-8141(94)90151-1.

Lyons, J. B., Wothner, W. A., Moench, R. H., & Thompson, J. B., 1997, Bedrock geologic map of New Hampshire: U.S. Geological Survey, Reston, VA, State Geological Map, 2 sheets, scales 1:250,000 and 1:500,000.

Ludwig, K.R., 2003. Isoplot/EX, rev. 3.00, a Geochronological Toolkit for Microsoft Excel: Berkeley Geochronology Center Special Publication, v. 4, 71 pp.

Malo, M., Ruffet, G., Pincivy, A. and Tremblay, A., 2008. A $^{40}Ar/^{39}Ar$ study of oceanic and continental deformation processes during an oblique collision: Taconian orogeny in the Quebec reentrant of the Canadian Appalachians: Tectonics, v. 27, no. 4, doi: 10.1029/2006TC002094.

Macdonald, F.A., Ryan-Davis, J., Coish, R.A., Crowley, J.L., and Karabinos, P., 2014, A newly identified Gondwanan terrane in the northern Appalachian Mountains: Implications for the Taconic orogeny and closure of the Iapetus Ocean: Geology, v. 42, no. 6, p. 539–542, doi:10.1130/G35659.1.

Massonne, H.J., Willner, A.P. and Gerya, T., 2007. Densities of metapelitic rocks at high to ultrahigh pressure conditions: What are the geodynamic consequences?: Earth and Planetary Science Letters, v. 256, no. 1–2, p.12–27, doi: 10.1016/j.epsl.2007.01.013.

McDougall, I. and Harrison, T.M., 1999. Geochronology and Thermochronology by the $^{40}Ar/^{39}Ar$ Method: Oxford University Press, Oxford, 269 p.

Mersereau, K. J., Richard, D. M., & Rennick, M. P., 2008, Bedrock geology of New Brunswick: New Brunswick Department of Natural Resources, Minerals Policy and Planning Division, Map NR-1, scale 1:500,000.

Naylor, R. S., 1971. Acadian Orogeny: An Abrupt and Brief Event: Science v. 172, p. 558–560.

Nishikawa, O. and Takeshita, T., 1999. Dynamic analysis and two types of kink bands in quartz veins deformed under subgreenschist conditions: Tectonophysics, v. 301, no. 1–2, p. 21–34, doi: 10.1016/S0040-1951(98)00219-4.

Neuendorf, K.K.E., Mehl, Jr., J.P., and Jackson, J.A., 2011. Glossary of geology (5th edition): American Geological Institute, Alexandria, Virginia, 783 p.

O'Beirne-Ryan, A.M., Jamieson, R.A. and Gagnon, Y.D., 1990. Petrology of garnet–clinopyroxene amphibolites from Mont Albert, Gaspé, Quebec: Canadian Journal of Earth Sciences, v. 27, p. 72–86, doi: 10.1139/e90-006.

Osberg, P. H., Hussey, A. M., II, & Boone, G. M. (editors), 1985, Bedrock geologic map of Maine: Maine Geological Survey, 1 plate, correlation chart, tectonic inset map, metamorphic inset map, color geologic map, cross sections, scale 1:500,000.

Ota, T. and Kaneko, Y., 2010. Blueschists, eclogites, and subduction zone tectonics: Insights from a review of Late Miocene blueschists and eclogites, and related young high-pressure metamorphic rocks: Gondwana Research, v. 18, p.167–188, doi: 10.1016/j.gr.2010.02.013.

Passchier, C.W. and Trouw, R.A., 2005. Microtectonics. Springer-Verlag, Berlin. 366 p.

Pidgeon, E., 2017. Geochronology and microstructures of the Tillotson Peak Complex in Lowell, Vermont: Vermont Geological Society Annual Meeting.

Pinet, N., 2013. Gaspé belt subsurface geometry in the northern Quebec Appalachians as revealed by an integrated geophysical and geological study: 2-Seismic interpretation and potential field modelling results: Tectonophysics, v. 588, p. 100–117, doi: 10.1016/j.tecto.2012.12.006.

Platt, J.P., 1993. Exhumation of high-pressure rocks: A review of concepts and processes: Terra nova, v. 5, no. 2, p. 119–133, doi: 10.1111/j.1365-3121.1993.tb00237.x.

Purdy J. W. and Jäger E., 1976. K-Ar ages on rock-forming minerals from the Central Alps: Institute of Geology and Mining University of Padova Memoir, v. 30, p. 31.

Rankin, D. W., Coish, R. A., Tucker, R. D., Peng, Z. X., Wilson, S. A., & Rouff, A. A., 2007, Silurian extension in the upper Connecticut Valley in the United States and the origin of Middle Paleozoic basins in the Québec embayment: American Journal of Science, v. 307, p. 216−264, doi: 10.2475/01.2007.07.

Ratcliffe, N.M., Hames, W.E. and Stanley, R.S., 1998. Interpretation of ages of arc magmatism, metamorphism, and collisional tectonics in the Taconian orogen of western New England: American Journal of Science, v. 298, no. 9, p. 791.

Ratcliffe, N.M., Stanley, R.S, Gale, M.H., Thompson, P.J., & Walsh, G.J., 2011, Bedrock Geologic Map of Vermont: U.S. Geological Survey Scientific Investigations Map 3184, 3 sheets, scale 1:100,000.

Ratschbacher, L., Hacker, B.R., Webb, L.E., McWilliams, M., Ireland, T., Dong, S., Calvert, A., Chateigner, D. and Wenk, H.R., 2000. Exhumation of the ultrahigh-pressure continental crust in east central China: Cretaceous and Cenozoic unroofing and the Tan-Lu fault: Journal of Geophysical Research: Solid Earth, v. 105, no. B6, p. 13303–13338, doi: 10.1029/2000JB900040.

Reiners, P.W. and Brandon, M.T., 2006. Using thermochronology to understand orogenic erosion: Annual Reiew of Earth and Planetary Sciences, v. 34, p. 419–466.

Renne, P. R., Swisher, C. C., Deino, A. L., Karner, D. B., Owens, T. L., & DePaolo, D. J., 1998, Intercalibration of standards, absolute ages and uncertainties in $^{40}Ar/^{39}Ar$ dating: Chemical Geology, v. 145, p. 117–152.

Renne, P.R., Deino, A.L., Hilgen, F.J., Kuiper, K.F., Mark, D.F., Mitchell, W.S., Morgan, L.E., Mundil, R. and Smit, J., 2013. Time scales of critical events around the Cretaceous-Paleogene boundary: Science, v. 339, no. 6120, p. 684–687, doi: 10.1126/science.1230492.

Robinson, P., Thompson, P. J., & Elbert, D. C., 1991. The nappe theory in the Connecticut Valley region: Thirty-five years since Jim Thompson's first proposal: American Mineralogist, v. 76, p. 689−712.

Schneider, D.A., Zahniser, S.J., Glascock, J.M., Gordon, S.M. and Manecki, M., 2006. Thermochronology of the west Sudetes (Bohemian Massif): Rapid and repeated eduction in the eastern Variscides, Poland and Czech Republic: American Journal of Science, v. 306, no. 10, p. 846–873, doi: 10.2475/10.2006.03.

Schmidt, M.W. and Poli, S., 2003. Generation of mobile components during subduction of oceanic crust: Treatise on geochemistry, v. 3, p. 659.

Smelik, E.A. and Veblen, D.R., 1989. A five-amphibole assemblage from blueschists in northern Vermont: American Mineralogist, v. 74, no. 7–8, p. 960–964.

Smelik, E.A. and Veblen, D.R., 1991. Exsolution of cummingtonite from glaucophane: A new orientation for exsolution lamellae in clinoamphiboles: American Mineralogist, v. 76, p. 971–984.

Smith, D.C., 1984. Coesite in clinopyroxene in the Caledonides and its implications for geodynamics: Nature, v. 310(5979), p. 641, doi: 10.1038/310641a0.

Šoštarić, S.B., Palinkaš, A.L., Neubauer, F., Cvetković, V., Bernroider, M. and Genser, J., 2014. The origin and age of the metamorphic sole from the Rogozna Mts., Western Vardar Belt: New evidence for the one-ocean model for the Balkan ophiolites: Lithos, v. 192, p. 39–55, doi: 10.1016/j.lithos.2014.01.011.

Spear, F. S., & Harrison, T. M., 1989, Geochronologic studies in central New England I: evidence for pre-Acadian metamorphism in eastern Vermont: Geology, v. 17, p. 181–184, doi: 10.1130/0091-7613(1989)017<0181:GSICNE>2.3.CO;2.

Stanley, R. S., & Ratcliffe, N. M., 1985, Tectonic synthesis of the Taconian orogeny in

western New England: Geological Society of America Bulletin, v. 96, p. 1227–1250, doi: 10.1130/0016-7606(1985)96<1227:TSOTTO>2.0.CO;2.

Stipp, M., Stuenitz, H., Heilbronner, R. and Schmid, S.M., 2002. The eastern Tonale fault zone: a 'natural laboratory' for crystal plastic deformation of quartz over a temperature range from 250 to 700 C: Journal of Structural Geology, v. 24, no. 12, p. 1861–1884, doi: 10.1016/S0191-8141(02)00035-4.

Sutter, J. F., Ratcliffe, N. M., & Musaka, S. B., 1985, $^{40}Ar/^{39}Ar$ and K/Ar data bearing on the metamorphic and tectonic history of western New England. Geological Society of America Bulletin. v. 96, p. 123−136, doi: 10.1130/0016-7606(1985)96<123:AAKDBO>2.0.CO;2.

Tam, E., Webb, L.E., and Aiken, C.L., 2018, Geochronologic constraints on the timing of deformation in the footwall of the Prospect Rock Fault in north-central Vermont: Geological Society of America Abstracts with Programs, v. 50, no. 2, doi: 10.1130/abs/2018NE-310928.

Thompson Jr, J.B., Rosenfeld, J.L., Hepburn, J.C. and Trzcienski, W.E., 1997. How does New Hampshire connect to Vermont?: Guidebook for field trips in Vermont and adjacent New Hampshire and New York: New England Intercollegiate Geological Conference Annual Meeting, 89th, Rutland, Vermont, p. C6–1–17.

Thompson, P.J. and Thompson, T.B., 2003. The Prospect Rock thrust: western limit of the Taconian accretionary prism in the northern Green Mountain anticlinorium, Vermont: Canadian Journal of Earth Sciences, v. 40, no. 2, p. 269–284, doi: 10.1139/e02-109.

Tremblay, A. and Pinet, N., 1994. Distribution and characteristics of Taconian and Acadian deformation, southern Québec Appalachians: Geological Society of America Bulletin, v. 106, no. 9, p. 1172–1181, doi: 10.1130/0016 7606(1994)106<1172:DACOTA>2.3.CO;2.

Tremblay, A., Ruffet, G. and Castonguay, S., 2000. Acadian metamorphism in the Dunnage zone of southern Quebec, northern Appalachians: $^{40}Ar/^{39}Ar$ evidence for collision diachronism: Geological Society of America Bulletin, v. 112, p. 136–146, doi: 10.1130/0016-7606(2000)112<136:AMITDZ>2.0.CO;2.

Tremblay, A. and Castonguay, S., 2002. Structural evolution of the Laurentian margin revisited (southern Quebec Appalachians): Implications for the Salinian orogeny and successor basins: Geology, v. 30, p. 79–82, doi: 10.1130/0091-7613(2002)030<0079:SEOTLM>2.0.CO;2.

Tremblay, A., Pinet, N., 2005. Silurian to Early Devonian tectonic evolution of the northern Appalachians (Canada and northeastern USA) and the origin of the Connecticut

Valley-Gaspé and Merrimack troughs. Geological Magazine, v. 142, p. 1–16.

Tremblay, A., Ruffet, G. and Bédard, J.H., 2011. Obduction of Tethyan-type ophiolites—A case-study from the Thetford-Mines ophiolitic Complex, Quebec Appalachians, Canada. Lithos, v. 125(1–2), p. 10–26, doi: 10.1016/j.lithos.2011.01.003.

Tremblay, A. and Pinet, N., 2016. Late Neoproterozoic to Permian tectonic evolution of the Quebec Appalachians, Canada: Earth-science reviews, v. 160, p. 131–170, doi: 10.1016/j.earscirev.2016.06.015.

Tucker, R.D., Robinson, P., 1990. Age and setting of the Bronson Hill magmatic arc: a reevaluation based on U-Pb zircon ages in southern New England: Geological Society of America Bulletin, v. 102, p. 1404–1419, doi: 10.1130/0016 7606(1990)102<1404:AASOTB>2.3.CO;2.

van Daalen, M., Heilbronner, R. and Kunze, K., 1999. Orientation analysis of localized shear deformation in quartz fibers at the brittle–ductile transition: Tectonophysics, v. 303, no. 1–4, p. 83–107, doi: 10.1016/S0040-1951(98)00264-9.

van Staal, C.R., and de Roo, J.A., 1995. Mid-Paleozoic tectonic evolution of the Appalachian Central Mobile Belt in northern New Brunswick, Canada: collision, extensional collapse, and dextral transpression: Current Perspectives in the Appalachian-Caledonian Orogen. Geological Association of Canada, Special Paper v. 41, pp. 367–389.

van Staal, C.R., Whalen, J.B., McNicoll, V.J., Pehrsson, S., Lissenberg, C.J., Zagorevski, A., Van Breemen, O. and Jenner, G.A., 2007. The Notre Dame arc and the Taconic orogeny in Newfoundland: Geological Society of America Memoirs, v. 200, p. 511–552.

van Staal, C.R., Whalen, J.B., Valverde-Vaquero, P., Zagorevski, A., and Rogers, N., 2009. Pre-Carboniferous, episodic accretion-related, orogenesis along the Laurentian margin of the northern Appalachians: Ancient Orogens and Modern Analogues, Geological Society, London, Special Publications v. 327, pp. 271–316, doi: 10.1144/SP327.13.

van Staal, C.R., Barr, S.M. and Percival, J.A., 2012. Lithospheric architecture and tectonic evolution of the Canadian Appalachians and associated Atlantic margin: Tectonic styles in Canada: the LITHOPROBE perspective, Geological Association of Canada, Special Paper, 49.

Wang, X., Liou, J.G. and Mao, H.K., 1989. Coesite-bearing eclogite from the Dabie Mountains in central China: Geology, v. 17, no. 12, p. 1085–1088, doi: 10.1130/0091-7613(1989)017<1085:CBEFTD>2.3.CO;2.

Warren, C.J., Beaumont, C. and Jamieson, R.A., 2008. Modelling tectonic styles and ultra-high pressure (UHP) rock exhumation during the transition from oceanic subduction

to continental collision: Earth and Planetary Science Letters, v. 267, no. 1–2, p. 129–145, doi: 10.1016/j.epsl.2007.11.025.

Warren, C.J., Hanke, F. and Kelley, S.P., 2012. When can muscovite $^{40}Ar/^{39}Ar$ dating constrain the timing of metamorphic exhumation?: Chemical Geology, 291, p. 79–86, doi: 10.1016/j.chemgeo.2011.09.017.

Webb, L.E., Baldwin, S.L., Little, T.A. and Fitzgerald, P.G., 2008. Can microplate rotation drive subduction inversion?: Geology, v. 36, no. 10, p. 823–826, doi: 10.1130/G25134A.

Webb, L.E., Baldwin, S.L. and Fitzgerald, P.G., 2014. The Early-Middle Miocene subduction complex of the Louisiade Archipelago, southern margin of the Woodlark Rift: Geochemistry, Geophysics, Geosystems, v. 15, no. 10, p. 4024–4046, doi: 10.1002/2014GC005500.

West, D.P., Ludman, A., and Lux, D.R., 1992. Silurian age for the Pocomoonshine gabbro-diorite, southeastern Maine and its regional tectonic implications: American Journal of Science, v 292, p. 253–273, doi: 10.2475/ajs.292.4.253.

Wheeler, J. O., Hoffman, P. F., Card, K. D., Davidson, A., Sanford, B. V., Okulitch, A.V., & Roest, W. R., 1996, Geological map of Canada / Carte géologique du Canada: Geological Survey of Canada, "A" Series Map 1860A, scale 1: 5,000,000.

Whitehead, J., Reynolds, P.H., Spray, J.G., 1996. $^{40}Ar/^{39}Ar$ age constraints on Taconian and Acadian events in the Quebec Appalachians: Geology, v. 24, p. 359–362.

Zen, E., Goldsmith, R., Ratcliffe, N. M., Robinson, P., Stanley, R. S., Hatch, N. L., Shride, A. F., Weed, E. G. A., & Wones, D. R., 1983, Bedrock geologic map of Massachusetts: U.S. Geological Survey, scale 1:250,000.

Zhang, L., Ai, Y., Li, X., Rubatto, D., Song, B., Williams, S., Song, S., Ellis, D. and Liou, J.G., 2007. Triassic collision of western Tianshan orogenic belt, China: evidence from SHRIMP U–Pb dating of zircon from HP/UHP eclogitic rocks: Lithos, v. 96, no. 1–2, p. 266–280, doi: 10.1016/j.lithos.2006.09.012.

Zhang, C., Bader, T., van Roermund, H., Yang, J., Shen, T., Qiu, T. and Li, P., 2018. The metamorphic evolution and tectonic significance of the Sumdo HP–UHP metamorphic terrane, central-south Lhasa Block, Tibet: Geological Society, London, Special Publications, v. 474, 21 p, doi: 10.1144/SP474.4.

Zheng, Y.F. and Zhao, Z.F., 2017, Introduction to the structures and processes of subduction zones: Journal of Asian Earth Sciences, v. 145, p. 1–15, doi: 10.1016/j.jseaes.2017.

APPENDIX A: $^{40}AR/^{39}AR$ AND U-Pb ANALYTICAL RESULTS

Table A-01: $^{40}Ar/^{39}Ar$ analytical results for sample 16TP03A, tourmaline (J= 3.746E-03 ± 0.24)

Laser Wattage	Time (min)	$^{38}Ar/^{39}Ar$	$^{38}Ar/^{39}Ar$ Err	$^{37}Ar/^{39}Ar$	$^{37}Ar/^{39}Ar$ Err	$^{36}Ar/^{39}Ar$	$^{36}Ar/^{39}Ar$ Err	^{39}Ar (cps)	^{39}Ar (cps) Err	Cumul % ^{39}Ar	% ^{40}Ar*	^{40}Ar*/^{39}Ar	$^{39}Ar/^{40}Ar$	$^{39}Ar/^{40}Ar$ Err	Age (Ma)	1 σ Err (Ma)	% Err
3.70	1.00	0.3378	0.0217	14.7341	2.3422	1.2303	0.0635	26.53	0.69	0.342	93.798	5621.67	0.000169	0.000004	5661.89	49.09	0.87
3.80	1.00	0.3082	0.0127	9.7049	1.1689	1.3883	0.0424	48.20	0.79	0.965	91.394	4439.17	0.000208	0.000003	5251.65	31.69	0.60
3.90	1.00	0.1198	0.0056	3.6586	0.5580	0.4999	0.0232	117.80	2.45	2.485	92.602	1875.84	0.000496	0.000010	3811.77	36.42	0.96
4.00	1.00	0.0986	0.0066	3.8664	0.4215	0.3534	0.0152	163.87	2.39	4.600	91.976	1214.76	0.000760	0.000011	3136.61	24.30	0.77
4.10	1.00	0.0549	0.0018	2.8685	0.2114	0.2063	0.0045	316.97	3.69	8.691	92.808	797.79	0.001168	0.000014	2531.81	17.61	0.70
4.20	1.00	0.0403	0.0019	1.8342	0.1099	0.1426	0.0041	674.45	8.36	17.397	92.971	564.80	0.001651	0.000021	2079.85	17.20	0.83
4.30	1.00	0.0393	0.0015	2.1637	0.0850	0.1245	0.0031	871.67	6.48	28.647	94.135	598.71	0.001577	0.000012	2152.98	10.70	0.50
4.40	1.00	0.0309	0.0014	2.8790	0.1272	0.0693	0.0022	1100.24	13.59	42.848	93.850	316.85	0.002974	0.000037	1432.05	13.52	0.94
4.50	1.00	0.0239	0.0008	4.3475	0.1215	0.0550	0.0015	717.03	7.93	52.103	92.927	217.08	0.004307	0.000048	1089.07	10.10	0.93
4.70	1.00	0.0234	0.0008	7.2412	0.2160	0.0654	0.0030	768.40	9.22	62.021	86.730	129.06	0.006795	0.000082	721.76	8.42	1.17
5.00	1.00	0.0235	0.0007	7.9623	0.1909	0.0667	0.0022	1030.41	10.37	75.321	82.317	93.97	0.008883	0.000091	551.92	6.02	1.09
5.50	1.00	0.0201	0.0006	7.5667	0.1665	0.0439	0.0011	1078.83	10.34	89.246	88.004	97.35	0.009158	0.000089	569.01	5.49	0.97
FUSE	1.00	0.0211	0.0014	3.8798	0.1607	0.0422	0.0023	833.21	11.41	100.000	79.462	49.24	0.016310	0.000229	309.80	5.04	1.63

Table A-02: $^{40}Ar/^{39}Ar$ analytical results for sample 16TP03A, white mica aliquot 1 (J= 3.745E-03 ± 0.24)

Laser Wattage	Time (min)	$^{38}Ar/^{39}Ar$	$^{38}Ar/^{39}Ar$ Err	$^{37}Ar/^{39}Ar$	$^{37}Ar/^{39}Ar$ Err	$^{36}Ar/^{39}Ar$	$^{36}Ar/^{39}Ar$ Err	^{39}Ar (cps)	^{39}Ar (cps) Err	Cumul % ^{39}Ar	% ^{40}Ar*	^{40}Ar*/^{39}Ar	$^{39}Ar/^{40}Ar$	$^{39}Ar/^{40}Ar$ Err	Age (Ma)	1 σ Err (Ma)	% Err
4.000	1.00	0.01579	0.00092	0.62947	0.11092	0.02884	0.00264	498.30	8.03	4.94	89.50	73.550	0.01220	0.00020	445.29	7.33	1.65
4.025	1.00	0.01280	0.00064	0.11534	0.02707	0.00037	0.00035	1945.26	19.33	24.22	99.86	76.716	0.01304	0.00013	462.22	4.28	0.92
4.050	1.00	0.01069	0.00029	0.08244	0.02014	0.00054	0.00029	2453.51	20.93	48.54	99.79	76.957	0.01299	0.00011	463.51	3.76	0.81
4.075	1.00	0.01086	0.00049	0.19314	0.05242	0.00071	0.00071	1005.22	12.61	58.50	99.71	73.843	0.01352	0.00017	446.87	5.18	1.16
4.600	1.00	0.01101	0.00026	0.06590	0.02015	0.00106	0.00027	2613.35	18.50	84.40	99.59	75.988	0.01312	0.00010	458.34	3.18	0.69
FUSE	1.00	0.00994	0.00034	0.09875	0.03504	0.00045	0.00042	1573.65	14.21	100.00	99.83	78.058	0.01281	0.00012	469.36	4.01	0.85

Table A-03: $^{40}Ar/^{39}Ar$ analytical results for sample 16TP03A, white mica aliquot 2 (J= 3.745E-03 ± 0.24)

Laser Wattage	Time (min)	$^{38}Ar/^{39}Ar$	$^{38}Ar/^{39}Ar$ Err	$^{37}Ar/^{39}Ar$	$^{37}Ar/^{39}Ar$ Err	$^{36}Ar/^{39}Ar$	$^{36}Ar/^{39}Ar$ Err	^{39}Ar (cps)	^{39}Ar (cps) Err	Cumul % ^{39}Ar	% ^{40}Ar*	^{40}Ar*/^{39}Ar	$^{39}Ar/^{40}Ar$	$^{39}Ar/^{40}Ar$ Err	Age (Ma)	1 σ Err (Ma)	% Err
3.800	1.00	0.04381	0.02859	2.71177	7.67671	0.44239	0.10497	19.47	0.64	0.04	-20.20	-21.85	0.00910	0.00056	-156.23	50.22	-32.14
3.900	1.00	0.03023	0.00808	-165.04551	-3.22871	0.20233	0.03581	69.83	0.95	0.19	**50.53**	**43.81**	0.00819	0.00016	278.06	12.85	4.62
4.000	1.00	0.01254	0.00149	0.71510	0.34182	0.02913	0.00550	438.02	7.76	1.13	89.22	72.17	0.01240	0.00023	437.88	8.03	1.83
4.050	1.00	0.01156	0.00117	0.09386	0.26569	0.02218	0.00410	563.27	8.94	2.34	91.64	72.73	0.01262	0.00021	440.90	7.02	1.59
4.080	1.00	0.01608	0.00046	0.04999	0.01706	0.01974	0.00068	9123.41	58.10	21.93	92.93	77.65	0.01199	0.00008	467.17	3.14	0.67
4.090	1.00	0.01230	0.00020	0.02929	0.00752	0.00236	0.00013	20694.94	125.86	66.36	99.10	77.53	0.01280	0.00008	466.56	2.81	0.60
4.091	1.00	0.01125	0.00048	0.02868	0.08118	0.00860	0.00130	1845.14	19.91	70.32	96.59	72.89	0.01327	0.00015	441.76	4.56	1.03
4.095	1.00	0.01137	0.00049	0.18809	0.09237	0.01018	0.00130	1515.41	18.16	73.57	95.93	71.68	0.01341	0.00016	435.22	5.02	1.15
4.120	1.00	0.01471	0.00090	0.02432	0.09680	0.01163	0.00129	1445.95	15.32	76.68	95.42	72.42	0.01320	0.00014	439.18	4.55	1.04
4.200	1.00	0.01193	0.00046	0.37080	0.09416	0.00936	0.00138	1557.20	15.64	80.02	96.34	73.74	0.01309	0.00013	446.33	4.31	0.97
4.450	1.00	0.01551	0.00088	0.84172	0.10676	0.01263	0.00186	1259.49	13.07	82.72	95.10	73.42	0.01299	0.00014	444.59	4.53	1.02
5.000	1.00	0.01373	0.00092	0.74914	0.16985	0.01193	0.00159	755.00	9.62	84.35	95.46	75.10	0.01275	0.00017	453.58	5.60	1.23
FUSE	1.00	0.01295	0.00033	0.14165	0.02107	0.00856	0.00055	7291.57	51.79	100.00	96.76	76.42	0.01269	0.00009	460.64	3.29	0.71

Table A-04: $^{40}Ar/^{39}Ar$ analytical results for sample 16TP04B, white mica (J= 3.746E-03 ± 0.24)

Laser Wattage	Time (min)	$^{38}Ar/^{39}Ar$	$^{38}Ar/^{39}Ar$ Err	$^{37}Ar/^{39}Ar$	$^{37}Ar/^{39}Ar$ Err	$^{36}Ar/^{39}Ar$	$^{36}Ar/^{39}Ar$ Err	^{39}Ar (cps)	^{39}Ar (cps) Err	Cumul % ^{39}Ar	% ^{40}Ar*	^{40}Ar*/^{39}Ar	$^{39}Ar/^{40}Ar$	$^{39}Ar/^{40}Ar$ Err	Age (Ma)	1 σ Err (Ma)	% Err
4.000	1.00	0.01158	0.00167	1.17992	0.29220	0.01103	0.00376	192.29	5.38	5.69	95.93	77.92	0.01235	0.00035	468.71	12.22	2.61
4.050	1.00	0.01178	0.00058	0.66603	0.07109	0.00700	0.00098	717.46	10.34	26.91	97.35	76.84	0.01270	0.00019	463.02	6.27	1.35
4.075	1.00	0.01034	0.00059	0.62808	0.07204	0.00374	0.00093	709.82	12.29	47.91	98.50	73.44	0.01344	0.00024	444.80	7.10	1.60
4.100	1.00	0.01155	0.00072	0.78444	0.10575	0.00783	0.00130	532.17	8.34	63.65	96.99	75.66	0.01285	0.00021	456.73	6.74	1.47
4.300	1.00	0.01065	0.00063	0.95038	0.08669	0.00472	0.00105	620.64	8.42	82.01	98.18	76.27	0.01291	0.00018	459.94	5.81	1.26
4.900	1.00	0.01517	0.00189	2.19800	0.30890	0.00904	0.00388	176.42	5.37	87.22	96.61	77.34	0.01256	0.00039	465.64	13.22	2.84
FUSE	1.00	0.01198	0.00091	1.02111	0.12449	0.00713	0.00153	431.90	7.49	100.00	97.35	78.46	0.01245	0.00022	471.61	7.55	1.60

Table A-05: $^{40}Ar/^{39}Ar$ analytical results for sample 16TP05BA, actinolite (J= 3.766E-03 ± 0.24)

Laser Wattage	Time (min)	$^{38}Ar/^{39}Ar$	$^{38}Ar/^{39}Ar$ Err	$^{37}Ar/^{39}Ar$	$^{37}Ar/^{39}Ar$ Err	$^{36}Ar/^{39}Ar$	$^{36}Ar/^{39}Ar$ Err	^{39}Ar (cps)	^{39}Ar (cps) Err	Cumul % ^{39}Ar	% ^{40}Ar*	^{40}Ar*/^{39}Ar	$^{39}Ar/^{40}Ar$	$^{39}Ar/^{40}Ar$ Err	Age (Ma)	1 σ Err (Ma)	% Err
3.80	1.00	0.2337	0.0395	31.6261	7.4870	1.2418	0.0977	8.68	0.42	1.158	85.429	2228.64	0.000393	0.000019	4099.58	92.60	2.26
3.90	1.00	0.0380	0.0279	8.1654	6.5798	0.1855	0.0644	9.69	0.45	2.451	79.405	215.73	0.003719	0.000183	1088.40	50.74	4.66
4.00	1.00	0.0404	0.0410	23.7473	8.8178	0.1107	0.0793	7.64	0.43	3.470	78.495	124.79	0.006506	0.000376	705.08	42.43	6.02
4.10	1.00	0.0242	0.0617	39.5800	14.3081	0.0154	0.1279	8.15	0.71	4.557	97.221	169.04	0.006037	0.000539	901.61	64.17	7.12
4.20	1.00	0.0696	0.0369	17.5040	7.7107	0.3141	0.0769	8.32	0.44	5.667	50.601	98.92	0.005267	0.000321	579.54	58.89	10.16
4.40	1.00	0.0200	0.0124	23.6692	2.8543	0.1791	0.0281	22.79	0.60	8.708	79.417	212.07	0.003849	0.000110	1074.41	29.16	2.71
4.60	1.00	0.0580	0.0039	46.6125	1.7920	0.2506	0.0090	93.24	1.75	21.147	86.070	482.28	0.001862	0.000035	1895.03	25.89	1.37
4.80	1.00	0.0157	0.0016	49.2414	1.3928	0.0413	0.0032	229.16	5.38	51.716	90.437	124.89	0.007760	0.000184	705.52	14.89	2.11
5.00	1.00	0.0177	0.0035	50.1637	1.8538	0.0307	0.0071	87.80	1.84	63.428	91.307	104.07	0.009478	0.000207	605.26	11.90	1.97
5.60	1.00	0.0172	0.0029	63.0390	1.9578	0.0614	0.0065	103.06	2.05	77.175	84.853	112.79	0.008263	0.000170	647.91	12.66	1.95
FUSE	1.00	0.0170	0.0019	58.3404	1.4803	0.0444	0.0041	171.10	2.88	100.000	89.461	122.34	0.007945	0.000137	693.54	10.78	1.55

Table A-06: $^{40}Ar/^{39}Ar$ analytical results for sample 16TP05BA, white mica (J= 3.755E-03 ± 0.24)

Laser Wattage	Time (min)	$^{38}Ar/^{39}Ar$	$^{38}Ar/^{39}Ar$ Err	$^{37}Ar/^{39}Ar$	$^{37}Ar/^{39}Ar$ Err	$^{36}Ar/^{39}Ar$	$^{36}Ar/^{39}Ar$ Err	^{39}Ar (cps)	^{39}Ar (cps) Err	Cumul % ^{39}Ar	% ^{40}Ar*	^{40}Ar*/^{39}Ar	$^{39}Ar/^{40}Ar$	$^{39}Ar/^{40}Ar$ Err	Age (Ma)	1 σ Err (Ma)	% Err
3.85	1.00	0.0685	0.0519	56.0230	14.2669	0.0008	0.1023	6.71	0.45	0.089	98.987	28.24	0.043638	0.020594	184.48	70.01	37.95
3.95	1.00	0.0397	0.0282	2.1923	4.8149	0.0533	0.0546	11.60	0.51	0.243	-15146.5	-15.65	9.585326	558.6385	-110.85	44.52	-40.16
4.00	1.00	0.0156	0.0118	1.1565	2.0735	0.0209	0.0210	29.50	0.63	0.634	71.561	15.87	0.045474	0.006066	105.92	19.07	18.00
4.05	1.00	0.0268	0.0047	0.3978	0.8726	0.0225	0.0106	60.33	0.96	1.434	93.191	91.95	0.010155	0.000187	542.82	9.35	1.72
4.08	1.00	0.0264	0.0076	6.8176	1.5915	0.0702	0.0186	35.88	1.23	1.910	76.310	68.52	0.011298	0.000399	419.01	17.22	4.11
4.13	1.00	0.0288	0.0026	1.5188	0.4864	0.0804	0.0060	116.37	2.25	3.453	76.981	80.65	0.009585	0.000194	484.15	11.19	2.31
4.15	1.00	0.0266	0.0040	3.8788	0.7374	0.0417	0.0088	77.19	1.74	4.477	85.613	74.76	0.011548	0.000272	452.81	11.03	2.44
4.18	1.00	0.0115	0.0003	0.2304	0.0284	0.0047	0.0004	1896.39	15.52	29.628	98.230	77.20	0.012745	0.000107	465.88	3.66	0.78
4.20	1.00	0.0133	0.0004	0.0981	0.0178	0.0021	0.0002	3181.49	25.59	71.823	99.196	76.89	0.012920	0.000108	464.20	3.60	0.78
4.22	1.00	0.0116	0.0005	0.3696	0.0798	0.0051	0.0010	668.49	8.74	80.689	98.088	78.24	0.012561	0.000168	471.40	5.74	1.22
4.70	1.00	0.0298	0.0044	2.4615	0.4614	0.0218	0.0056	123.25	2.26	82.324	93.309	91.44	0.010258	0.000198	540.17	9.72	1.80
FUSE	1.00	0.0122	0.0004	0.2777	0.0405	0.0063	0.0005	1332.78	14.79	100.000	97.638	77.53	0.012616	0.000142	467.62	4.86	1.04

Table A-07: $^{40}Ar/^{39}Ar$ analytical results for sample 16TP05D, white mica (J= 3.773E-03 ± 0.24)

Laser Wattage	Time (min)	$^{38}Ar/^{39}Ar$	$^{38}Ar/^{39}Ar$ Err	$^{37}Ar/^{39}Ar$	$^{37}Ar/^{39}Ar$ Err	$^{36}Ar/^{39}Ar$	$^{36}Ar/^{39}Ar$ Err	^{39}Ar (cps)	^{39}Ar (cps) Err	Cumul % ^{39}Ar	% ^{40}Ar*	^{40}Ar*/^{39}Ar	$^{39}Ar/^{40}Ar$	$^{39}Ar/^{40}Ar$ Err	Age (Ma)	1 σ Err (Ma)	% Err
3.90	1.00	0.0358	0.0049	1.6432	0.8515	0.1292	0.0115	64.83	1.71	1.257	69.349	87.69	0.007944	0.000219	523.12	18.06	3.45
3.93	1.00	0.0637	0.0112	0.0527	1.9568	0.2315	0.0257	28.18	0.76	1.803	58.0	95.85	0.006070	0.0002	564.96	23.71	4.20
4.00	1.00	0.0168	0.0044	1.7492	0.7935	0.0031	0.0094	66.04	1.61	3.083	98.876	82.03	0.012104	0.000319	493.52	11.56	2.34
4.03	1.00	0.0118	0.0005	0.1996	0.0493	0.0047	0.0007	1035.88	11.62	23.161	98.209	77.12	0.012756	0.000146	467.41	4.89	1.05
4.04	1.00	0.0133	0.0009	0.5191	0.1280	0.0051	0.0016	409.62	5.72	31.101	98.091	78.39	0.012541	0.000179	474.20	6.15	1.30
4.06	1.00	0.0115	0.0006	0.2503	0.0727	0.0017	0.0008	759.84	10.38	45.829	99.334	75.56	0.013170	0.000183	459.04	5.77	1.26
4.07	1.00	0.0116	0.0008	0.8927	0.1178	0.0045	0.0014	478.32	6.63	55.101	98.311	78.61	0.012542	0.000178	475.37	6.11	1.29
4.09	1.00	0.0103	0.0007	0.7581	0.1049	0.0024	0.0012	539.57	10.20	65.559	99.032	72.92	0.013618	0.000261	444.80	7.71	1.73
4.10	1.00	0.0128	0.0012	1.6584	0.2157	0.0087	0.0027	250.21	5.49	70.409	96.625	74.82	0.012970	0.000292	455.08	9.42	2.07
4.60	1.00	0.0091	0.0014	1.5213	0.2774	0.0057	0.0034	194.07	5.36	74.171	97.818	76.19	0.012890	0.000363	462.44	11.77	2.55
5.30	1.00	0.0159	0.0026	4.2042	0.5685	0.0242	0.0060	105.11	2.05	76.208	91.207	75.71	0.012154	0.000252	459.85	9.24	2.01
FUSE	1.00	0.0121	0.0004	0.4798	0.0406	0.0057	0.0006	1227.44	12.77	100.000	97.818	75.92	0.012911	0.000138	461.02	4.57	0.99

Table A-08: $^{40}Ar/^{39}Ar$ analytical results for sample 16TP08B, glaucophane aliquot 1 (J= 3.795E-03 ± 0.24)

Laser Wattage	Time (min)	$^{38}Ar/^{39}Ar$	$^{38}Ar/^{39}Ar$ Err	$^{37}Ar/^{39}Ar$	$^{37}Ar/^{39}Ar$ Err	$^{36}Ar/^{39}Ar$	$^{36}Ar/^{39}Ar$ Err	^{39}Ar (cps)	^{39}Ar (cps) Err	Cumul % ^{39}Ar	% $^{40}Ar^*$	$^{40}Ar^*/^{39}Ar$	$^{39}Ar/^{40}Ar$	$^{39}Ar/^{40}Ar$ Err	Age (Ma)	1 σ Err (Ma)	% Err
3.80	1.00	0.0911	0.0117	2.7269	2.1910	0.5429	0.0345	28.82	1.13	1.720	48.641	154.45	0.003169	0.000126	844.26	55.16	6.53
4.00	1.00	0.0309	0.0041	0.9917	0.7473	0.0666	0.0072	79.29	1.94	6.452	79.0	74.89	0.010579	0.0003	457.81	13.14	2.87
4.20	1.00	0.0248	0.0027	0.5591	0.4675	0.0516	0.0051	128.12	2.36	14.097	83.891	80.40	0.010461	0.000202	487.36	9.88	2.03
4.30	1.00	0.0131	0.0018	1.7704	0.3755	0.0205	0.0034	168.66	2.68	24.162	92.541	76.21	0.012198	0.000202	464.93	7.39	1.59
4.40	1.00	0.0151	0.0011	1.2170	0.1705	0.0209	0.0019	347.49	6.73	44.898	92.083	72.77	0.012700	0.000249	446.31	8.48	1.90
4.50	1.00	0.0147	0.0016	2.4559	0.2665	0.0120	0.0023	241.85	5.09	59.331	95.394	74.35	0.012904	0.000276	454.90	9.05	1.99
4.70	1.00	0.0141	0.0012	6.9694	0.2747	0.0122	0.0020	288.70	6.79	76.559	94.914	68.75	0.014006	0.000334	424.29	9.48	2.23
4.90	1.00	0.0150	0.0020	9.4882	0.4975	0.0163	0.0036	165.21	2.87	86.418	93.261	68.62	0.013854	0.000251	423.55	7.30	1.72
5.40	1.00	0.0104	0.0058	10.0218	1.3318	0.0284	0.0114	48.71	1.43	89.325	88.666	67.65	0.013377	0.000432	418.21	13.49	3.23
FUSE	1.00	0.0143	0.0019	19.4688	0.6323	0.0228	0.0032	178.88	4.36	100.000	90.924	70.91	0.013311	0.000333	436.16	10.47	2.40

Table A-09: $^{40}Ar/^{39}Ar$ analytical results for sample 16TP08B, glaucophane aliquot 2 (J= 3.795E-03 ± 0.24)

Laser Wattage	Time (min)	$^{38}Ar/^{39}Ar$	$^{38}Ar/^{39}Ar$ Err	$^{37}Ar/^{39}Ar$	$^{37}Ar/^{39}Ar$ Err	$^{36}Ar/^{39}Ar$	$^{36}Ar/^{39}Ar$ Err	^{39}Ar (cps)	^{39}Ar (cps) Err	Cumul % ^{39}Ar	% $^{40}Ar^*$	$^{40}Ar^*/^{39}Ar$	$^{39}Ar/^{40}Ar$	$^{39}Ar/^{40}Ar$ Err	Age (Ma)	1 σ Err (Ma)	% Err
3.80	1.00	0.0455	0.0018	3.7735	0.3738	0.2049	0.0078	398.29	6.94	4.332	55.511	77.05	0.007272	0.000129	470.16	13.22	2.81
3.90	1.00	0.0380	0.0019	4.3292	0.3852	0.1545	0.0082	373.63	7.00	8.396	64.7	85.30	0.007656	0.0001	513.99	13.09	2.55
4.10	1.00	0.0266	0.0010	2.7156	0.1246	0.0824	0.0024	1380.51	15.15	23.412	78.194	88.83	0.008859	0.000098	532.45	6.64	1.25
4.30	1.00	0.0168	0.0006	7.7218	0.2353	0.0274	0.0011	3137.34	25.69	57.537	89.979	74.67	0.012236	0.000102	457.33	3.86	0.84
4.40	1.00	0.0174	0.0009	32.9023	0.7215	0.0314	0.0015	1645.62	19.39	75.437	87.669	70.93	0.013166	0.000158	436.94	5.21	1.19
4.50	1.00	0.0193	0.0013	40.2007	1.5102	0.0366	0.0028	930.24	12.23	85.555	85.049	67.34	0.013681	0.000184	417.15	5.67	1.36
4.70	1.00	0.0131	0.0023	24.4941	1.3825	0.0162	0.0096	233.88	7.10	88.099	93.529	73.37	0.013350	0.000416	450.22	12.97	2.88
5.30	1.00	0.0107	0.0042	55.0871	1.8584	0.0016	0.0195	114.62	2.14	89.346	99.511	107.73	0.010042	0.000215	628.24	11.02	1.75
FUSE	1.00	0.0157	0.0007	55.3193	1.2525	0.0383	0.0034	979.52	12.34	100.000	86.061	78.03	0.012204	0.000159	475.41	6.05	1.27

Table A-10: $^{40}Ar/^{39}Ar$ analytical results for sample 16TP08B, white mica aliquot 1 (J= 3.746E-03 ± 0.24)

Laser Wattage	Time (min)	$^{38}Ar/^{39}Ar$	$^{38}Ar/^{39}Ar$ Err	$^{37}Ar/^{39}Ar$	$^{37}Ar/^{39}Ar$ Err	$^{36}Ar/^{39}Ar$	$^{36}Ar/^{39}Ar$ Err	^{39}Ar (cps)	^{39}Ar (cps) Err	Cumul % ^{39}Ar	% ^{40}Ar*	^{40}Ar*/^{39}Ar	$^{39}Ar/^{40}Ar$	$^{39}Ar/^{40}Ar$ Err	Age (Ma)	1 σ Err (Ma)	% Err
3.90	1.00	0.0867	0.0263	1.8746	4.2448	0.4010	0.0571	11.73	0.49	0.981	48.794	114.68	0.004277	0.000200	654.15	52.65	8.05
4.00	1.00	0.0410	0.0092	4.6051	1.4694	0.1371	0.0185	34.30	1.23	3.849	68.2	88.76	0.007760	0.0003	525.39	25.54	4.86
4.05	1.00	0.0281	0.0131	9.0509	2.3806	0.0270	0.0274	22.30	0.59	5.714	92.476	100.65	0.009326	0.000342	585.58	19.77	3.38
4.10	1.00	0.0282	0.0108	5.9180	1.9093	0.0566	0.0222	26.31	0.60	7.915	86.002	104.83	0.008287	0.000241	606.27	17.44	2.88
4.15	1.00	0.0306	0.0110	8.4820	1.9508	0.0250	0.0239	25.84	0.62	10.075	92.758	96.89	0.009711	0.000308	566.77	16.61	2.93
4.18	1.00	0.0194	0.0035	1.8937	0.5892	0.0469	0.0072	89.93	1.85	17.595	85.663	84.09	0.010234	0.000224	501.20	11.21	2.24
4.20	1.00	0.0173	0.0031	3.1095	0.5461	0.0277	0.0067	97.63	2.14	25.760	91.027	84.53	0.010839	0.000251	503.49	11.19	2.22
4.23	1.00	0.0160	0.0019	1.5677	0.3214	0.0151	0.0041	166.02	4.36	39.643	94.636	79.84	0.011901	0.000320	478.89	11.98	2.50
4.25	1.00	0.0172	0.0019	0.0883	0.3111	0.0087	0.0036	174.84	2.69	54.263	96.783	78.49	0.012348	0.000196	471.80	6.88	1.46
4.30	1.00	0.0173	0.0025	0.1270	0.4683	0.0123	0.0060	121.60	2.95	64.432	95.562	79.11	0.012098	0.000300	475.08	10.89	2.29
4.35	1.00	0.0254	0.0070	0.3904	1.3507	0.0380	0.0190	39.59	1.43	67.742	88.278	85.72	0.010320	0.000399	509.69	19.50	3.83
4.50	1.00	0.0182	0.0049	-2.0693	-1.3643	0.0124	0.0109	61.34	1.64	72.872	95.734	82.67	0.011557	0.000332	493.78	13.04	2.64
5.00	1.00	0.0438	0.0099	5.6756	3.1344	0.0596	0.0228	28.79	0.68	75.279	84.709	99.54	0.008596	0.000253	580.02	17.22	2.97
FUSE	1.00	0.0162	0.0012	0.62124	0.2022	0.0206	0.0024	295.62	5.52	100.0	92.874	80.30	0.011594	0.000221	481.35	8.73	1.81

Table A-11: $^{40}Ar/^{39}Ar$ analytical results for sample 16TP08B, white mica aliquot 2 (J= 3.746E-03 ± 0.24)

Laser Wattage	Time (min)	$^{38}Ar/^{39}Ar$	$^{38}Ar/^{39}Ar$ Err	$^{37}Ar/^{39}Ar$	$^{37}Ar/^{39}Ar$ Err	$^{36}Ar/^{39}Ar$	$^{36}Ar/^{39}Ar$ Err	^{39}Ar (cps)	^{39}Ar (cps) Err	Cumul % ^{39}Ar	% ^{40}Ar*	^{40}Ar*/^{39}Ar	$^{39}Ar/^{40}Ar$	$^{39}Ar/^{40}Ar$ Err	Age (Ma)	1 σ Err (Ma)	% Err
3.80	1.00	0.2636	0.2651	243.9651	138.5435	0.3692	0.5773	1.29	0.40	0.121	-137.472	-53.50	0.021546	0.009120	-409.38	203.29	-49.66
3.90	1.00	0.3188	0.1040	214.0995	54.8195	0.7081	0.2367	3.40	0.44	0.441	-3.4	12.14	0.004891	0.0006	81.39	206.63	253.88
4.00	1.00	0.0672	0.0181	33.1333	8.5931	0.1545	0.0419	18.98	0.65	2.225	57.497	66.73	0.009214	0.000418	408.39	27.69	6.78
4.05	1.00	0.0488	0.0099	18.1842	4.7455	0.0966	0.0238	32.91	0.71	5.318	71.365	74.41	0.009930	0.000229	450.03	12.68	2.82
4.08	1.00	0.0021	0.0155	11.0099	5.0510	0.1198	0.0219	32.07	0.75	8.333	69.963	85.00	0.008400	0.000242	505.93	18.02	3.56
4.11	1.00	0.0318	0.0091	30.5664	4.5603	0.0781	0.0213	35.18	1.25	11.639	75.188	74.82	0.010641	0.000451	452.21	21.83	4.83
4.14	1.00	0.0435	0.0096	8.3051	4.0903	0.1041	0.0215	36.73	1.15	15.091	71.562	79.48	0.009152	0.000322	477.02	20.46	4.29
4.17	1.00	0.0391	0.0074	7.2177	3.2486	0.0594	0.0152	48.07	1.46	19.610	80.063	72.25	0.011248	0.000387	438.44	16.64	3.79
4.20	1.00	0.0191	0.0023	5.1967	0.8746	0.0509	0.0047	168.52	4.27	35.450	82.752	73.77	0.011343	0.000292	446.60	12.30	2.75
4.23	1.00	0.0165	0.0015	2.1913	0.5042	0.0276	0.0029	277.84	7.06	61.567	90.160	75.84	0.011954	0.000306	457.69	11.52	2.52
4.27	1.00	0.0094	0.0089	22.3874	4.0828	0.0449	0.0216	34.98	1.40	64.855	84.228	74.66	0.011764	0.000537	451.39	21.17	4.69
4.35	1.00	0.0159	0.0140	57.3077	6.2761	0.1379	0.0320	23.21	0.73	67.036	58.724	65.90	0.010025	0.000429	403.81	24.49	6.06
4.50	1.00	0.0147	0.0108	27.6712	4.9127	0.0951	0.0254	30.02	0.77	69.858	73.232	81.63	0.009425	0.000311	488.34	18.79	3.85
4.8	1.00	0.0284	0.0110	38.15246	5.0496	0.1235	0.0243	30.33	1.21	72.7	66.457	78.34	0.009094	0.000406	471.01	26.80	5.69
5.3	1.00	0.0253	0.0076	21.00548	3.0526	0.0803	0.0167	44.71	1.50	76.9	73.974	70.98	0.010857	0.000375	431.54	17.56	4.07
FUSE	1.00	0.0164	0.0017	7.06905	0.6159	0.0430	0.0034	245.63	5.45	100.0	85.555	77.06	0.01126	0.000254	464.19	10.78	2.32

Table A-12: $^{40}Ar/^{39}Ar$ analytical results for sample 16TP15A, white mica (J= 3.811E-03 ± 0.24)

Laser Wattage	Time (min)	$^{38}Ar/^{39}Ar$	$^{38}Ar/^{39}Ar$ Err	$^{37}Ar/^{39}Ar$	$^{37}Ar/^{39}Ar$ Err	$^{36}Ar/^{39}Ar$	$^{36}Ar/^{39}Ar$ Err	^{39}Ar (cps)	^{39}Ar (cps) Err	Cumul % ^{39}Ar	% ^{40}Ar*	^{40}Ar*/^{39}Ar	$^{39}Ar/^{40}Ar$	$^{39}Ar/^{40}Ar$ Err	Age (Ma)	1 σ Err (Ma)	% Err
4.00	1.00	0.0140	0.0010	0.2691	0.1321	0.0225	0.0017	414.10	8.35	2.607	91.578	73.07	0.012557	0.000257	449.54	8.95	1.99
4.03	1.00	0.0239	0.0018	0.4018	0.2334	0.0679	0.0034	245.38	4.99	4.152	79.6	79.44	0.010047	0.0002	483.98	11.13	2.30
4.05	1.00	0.0132	0.0006	0.3094	0.0632	0.0140	0.0010	907.98	12.44	9.868	94.757	75.56	0.012564	0.000175	463.09	6.10	1.32
4.08	1.00	0.0110	0.0003	0.1174	0.0261	0.0037	0.0003	2195.17	19.60	23.687	98.550	75.24	0.013117	0.000121	461.37	3.93	0.85
4.10	1.00	0.0121	0.0003	0.0619	0.0098	0.0018	0.0001	6118.23	37.70	62.203	99.306	75.86	0.013108	0.000090	464.73	2.99	0.64
4.15	1.00	0.0119	0.0005	0.3143	0.0530	0.0034	0.0007	1083.56	12.61	69.025	98.684	75.79	0.013045	0.000154	464.33	5.00	1.08
4.15	1.00	0.0122	0.0007	0.5888	0.1067	0.0065	0.0013	539.42	8.83	72.421	97.512	75.77	0.012899	0.000214	464.24	7.05	1.52
4.50	1.00	0.0115	0.0003	0.0909	0.0287	0.0049	0.0004	1732.21	15.28	83.326	98.050	73.73	0.013318	0.000121	453.15	3.84	0.85
5.00	1.00	0.0138	0.0014	0.0575	0.1867	0.0131	0.0026	255.51	5.49	84.934	95.114	76.43	0.012462	0.000274	467.80	9.57	2.05
FUSE	1.00	0.0129	0.0005	0.0393	0.0238	0.0030	0.0003	2393.18	17.20	100.000	98.842	77.16	0.012828	0.000097	471.72	3.34	0.71

Table A-13: $^{40}Ar/^{39}Ar$ analytical results for sample 16TP15D, white mica (J= 3.818E-03 ± 0.24)

Laser Wattage	Time (min)	$^{38}Ar/^{39}Ar$	$^{38}Ar/^{39}Ar$ Err	$^{37}Ar/^{39}Ar$	$^{37}Ar/^{39}Ar$ Err	$^{36}Ar/^{39}Ar$	$^{36}Ar/^{39}Ar$ Err	^{39}Ar (cps)	^{39}Ar (cps) Err	Cumul % ^{39}Ar	% ^{40}Ar*	^{40}Ar*/^{39}Ar	$^{39}Ar/^{40}Ar$	$^{39}Ar/^{40}Ar$ Err	Age (Ma)	1 σ Err (Ma)	% Err
3.90	1.00	0.0203	0.0072	-4.3345	-1.7312	0.0978	0.0149	37.70	0.67	1.224	74.398	84.36	0.008772	0.000214	511.08	14.69	2.87
4.00	1.00	0.0157	0.0045	0.9955	0.9990	0.0452	0.0087	62.40	1.83	3.251	86.2	84.46	0.010236	0.0003	511.61	16.14	3.15
4.05	1.00	0.0247	0.0036	1.6184	0.7738	0.0754	0.0075	78.84	1.64	5.811	76.402	73.25	0.010478	0.000232	451.39	11.59	2.57
4.08	1.00	0.0207	0.0042	5.2191	1.4731	0.0640	0.0088	67.73	1.54	8.011	78.799	71.86	0.011088	0.000264	443.75	11.89	2.68
4.10	1.00	0.0120	0.0004	0.1986	0.0472	0.0094	0.0005	1383.44	12.96	52.939	96.466	76.85	0.012575	0.000122	470.91	4.27	0.91
4.12	1.00	0.0108	0.0006	0.4634	0.1099	0.0062	0.0010	569.44	9.93	71.432	97.563	74.84	0.013064	0.000231	460.05	7.42	1.61
4.20	1.00	0.0144	0.0010	0.8380	0.1973	0.0264	0.0018	332.76	7.81	82.238	90.251	73.11	0.012381	0.000295	450.61	10.59	2.35
4.70	1.00	0.0180	0.0023	1.7295	0.5616	0.0313	0.0048	116.60	2.45	86.025	89.224	77.84	0.011514	0.000254	476.27	10.38	2.18
5.50	1.00	0.0030	0.0013	0.3799	0.6759	0.0006	0.0023	331.76	8.01	96.799	99.797	89.11	0.011221	0.000273	535.99	11.38	2.12
FUSE	1.00	0.0104	0.0028	3.4572	0.6668	0.0263	0.0055	98.56	1.85	100.000	90.898	79.03	0.011587	0.000240	482.66	9.70	2.01

Table A-14: $^{40}Ar/^{39}Ar$ analytical results for sample 16TP16A, tourmaline (J= 3.821E-03 ± 0.24)

Laser Wattage	Time (min)	$^{38}Ar/^{39}Ar$	$^{38}Ar/^{39}Ar$ Err	$^{37}Ar/^{39}Ar$	$^{37}Ar/^{39}Ar$ Err	$^{36}Ar/^{39}Ar$	$^{36}Ar/^{39}Ar$ Err	^{39}Ar (cps)	^{39}Ar (cps) Err	Cumul % ^{39}Ar	% $^{40}Ar*$	$^{40}Ar*/^{39}Ar$	$^{39}Ar/^{40}Ar$	$^{39}Ar/^{40}Ar$ Err	Age (Ma)	1 σ Err (Ma)	% Err
3.70	1.00	0.4563	0.0144	1.9831	0.4449	2.2707	0.0673	147.50	2.62	1.216	65.553	1294.74	0.000508	0.000009	3263.10	41.94	1.29
3.80	1.00	0.0908	0.0031	1.8103	0.2987	0.4139	0.0082	231.21	3.07	3.121	88.3	935.96	0.000946	0.0000	2783.54	22.13	0.80
3.90	1.00	0.0403	0.0014	3.4639	0.1523	0.1623	0.0058	484.21	7.44	7.113	91.767	542.45	0.001699	0.000026	2054.51	21.10	1.03
4.00	1.00	0.0352	0.0022	2.2777	0.1545	0.1100	0.0056	497.22	11.18	11.211	90.860	327.79	0.002782	0.000063	1486.19	25.40	1.71
4.10	1.00	0.0284	0.0018	1.3247	0.0995	0.0723	0.0032	669.25	8.85	16.727	92.543	268.64	0.003454	0.000046	1292.68	13.56	1.05
4.20	1.00	0.0179	0.0005	0.7544	0.0491	0.0317	0.0009	1419.15	12.10	28.424	95.847	218.92	0.004388	0.000039	1112.53	7.92	0.71
4.30	1.00	0.0177	0.0004	1.3004	0.0439	0.0286	0.0007	1818.68	15.40	43.415	96.519	237.22	0.004080	0.000036	1180.91	8.21	0.70
4.40	1.00	0.0186	0.0005	2.3030	0.0623	0.0300	0.0008	1444.35	13.05	55.319	96.103	221.97	0.004346	0.000041	1124.11	8.37	0.75
4.50	1.00	0.0170	0.0005	3.6030	0.1140	0.0257	0.0009	1271.82	11.89	65.802	95.657	169.82	0.005665	0.000054	915.29	7.39	0.81
4.70	1.00	0.0172	0.0006	6.8650	0.1769	0.0288	0.0010	1129.22	12.66	75.110	95.077	167.64	0.005726	0.000065	906.01	8.70	0.96
5.10	1.00	0.0150	0.0004	6.3360	0.1224	0.0228	0.0011	1757.97	10.67	89.600	95.380	141.64	0.006798	0.000043	791.69	4.48	0.57
FUSE	1.00	0.0191	0.0005	4.1922	0.1289	0.0413	0.0020	1261.80	13.76	100.000	96.224	315.79	0.003064	0.000035	1448.55	11.96	0.83

Table A-15: $^{40}Ar/^{39}Ar$ analytical results for sample 16TP16A, white mica (J= 3.821E-03 ± 0.24)

Laser Wattage	Time (min)	$^{38}Ar/^{39}Ar$	$^{38}Ar/^{39}Ar$ Err	$^{37}Ar/^{39}Ar$	$^{37}Ar/^{39}Ar$ Err	$^{36}Ar/^{39}Ar$	$^{36}Ar/^{39}Ar$ Err	^{39}Ar (cps)	^{39}Ar (cps) Err	Cumul % ^{39}Ar	% $^{40}Ar*$	$^{40}Ar*/^{39}Ar$	$^{39}Ar/^{40}Ar$	$^{39}Ar/^{40}Ar$ Err	Age (Ma)	1 σ Err (Ma)	% Err
4.00	1.00	0.0153	0.0017	0.0274	0.2528	0.0166	0.0034	219.31	4.68	5.619	93.738	74.18	0.012655	0.000277	456.71	9.48	2.07
4.03	1.00	0.0127	0.0031	0.0603	0.5828	0.0109	0.0065	99.56	1.76	8.170	95.7	73.47	0.013050	0.0003	452.84	8.12	1.79
4.05	1.00	0.0122	0.0027	0.2051	0.5171	0.0000	0.0061	112.26	2.16	11.047	99.995	74.55	0.013434	0.000278	458.76	8.44	1.84
4.08	1.00	0.0164	0.0061	0.8204	1.0460	0.0088	0.0127	52.82	1.54	12.400	96.483	72.08	0.013423	0.000403	445.26	12.32	2.77
4.10	1.00	0.0121	0.0006	0.0092	0.0935	0.0099	0.0011	650.03	9.21	29.056	96.306	77.16	0.012498	0.000181	472.91	6.35	1.34
4.13	1.00	0.0111	0.0003	0.0457	0.0330	0.0030	0.0004	1681.43	16.14	72.139	98.832	75.57	0.013097	0.000128	464.28	4.18	0.90
4.15	1.00	0.0104	0.0013	0.0249	0.2513	0.0064	0.0028	242.02	4.99	78.340	97.531	75.92	0.012864	0.000269	466.17	8.88	1.90
5.00	1.00	0.0167	0.0012	0.0792	0.1014	0.0060	0.0014	548.95	9.52	92.406	97.625	73.56	0.013292	0.000233	453.32	7.28	1.61
FUSE	1.00	0.0145	0.0013	0.2775	0.1880	0.0187	0.0025	296.38	7.30	100.000	93.055	74.77	0.012468	0.000310	459.96	10.91	2.37

Table A-16: $^{40}Ar/^{39}Ar$ analytical results for sample 16TP17B, white mica (J= 3.825E-03 ± 0.23)

Laser Wattage	Time (min)	$^{38}Ar/^{39}Ar$	$^{38}Ar/^{39}Ar$ Err	$^{37}Ar/^{39}Ar$	$^{37}Ar/^{39}Ar$ Err	$^{36}Ar/^{39}Ar$	$^{36}Ar/^{39}Ar$ Err	^{39}Ar (cps)	^{39}Ar (cps) Err	Cumul % ^{39}Ar	% ^{40}Ar*	^{40}Ar*/^{39}Ar	$^{39}Ar/^{40}Ar$	$^{39}Ar/^{40}Ar$ Err	Age (Ma)	1 σ Err (Ma)	% Err
4.00	1.00	0.0130	0.0004	0.0471	0.0117	0.0068	0.0004	4775.73	27.64	62.594	97.274	73.02	0.013340	0.000085	450.85	27.78	0.62
4.05	1.00	0.0198	0.0016	0.7618	0.2309	0.0485	0.0033	233.20	3.42	65.651	83.4	73.18	0.011435	0.0002	451.71	85.86	1.90
4.60	1.00	0.0109	0.0009	0.7616	0.1281	0.0021	0.0013	500.85	7.72	72.215	99.039	64.55	0.015385	0.000258	403.89	61.83	1.53
4.03	1.00	0.0113	0.0006	0.4906	0.0906	0.0026	0.0011	644.92	7.95	80.668	98.907	71.52	0.013859	0.000185	442.61	53.92	1.22
FUSE	1.00	0.0139	0.0007	0.1592	0.0414	0.0027	0.0005	1474.96	15.89	100.000	98.915	72.26	0.013710	0.000152	446.70	45.38	1.02

Table A-17: $^{40}Ar/^{39}Ar$ analytical results for sample 16TP19A, white mica (J= 3.832E-03 ± 0.24)

Laser Wattage	Time (min)	$^{38}Ar/^{39}Ar$	$^{38}Ar/^{39}Ar$ Err	$^{37}Ar/^{39}Ar$	$^{37}Ar/^{39}Ar$ Err	$^{36}Ar/^{39}Ar$	$^{36}Ar/^{39}Ar$ Err	^{39}Ar (cps)	^{39}Ar (cps) Err	Cumul % ^{39}Ar	% ^{40}Ar*	^{40}Ar*/^{39}Ar	$^{39}Ar/^{40}Ar$	$^{39}Ar/^{40}Ar$ Err	Age (Ma)	1 σ Err (Ma)	% Err
3.80	1.00	0.0137	0.0097	9.3391	4.4390	0.0572	0.0189	36.55	1.46	0.458	81.401	76.15	0.010888	0.000488	468.72	22.54	4.81
3.90	1.00	0.0080	0.0030	4.2587	1.4461	0.0146	0.0061	112.02	2.13	1.861	94.8	80.90	0.011827	0.0002	494.35	9.47	1.92
3.94	1.00	0.0091	0.0036	0.7826	1.6099	0.0058	0.0069	95.51	2.01	3.058	97.855	79.47	0.012350	0.000276	486.68	9.81	2.02
3.98	1.00	0.0147	0.0022	1.4569	0.9234	0.0242	0.0044	166.85	6.14	5.148	91.040	73.76	0.012398	0.000461	455.69	16.47	3.61
4.02	1.00	0.0121	0.0005	0.8501	0.1896	0.0052	0.0008	855.37	10.41	15.863	98.026	76.62	0.012834	0.000158	471.30	5.30	1.12
4.04	1.00	0.0111	0.0004	0.2019	0.1291	0.0025	0.0005	1254.81	13.05	31.582	99.001	75.34	0.013168	0.000140	464.31	4.52	0.97
4.06	1.00	0.0110	0.0004	0.1929	0.1249	0.0025	0.0005	1296.97	14.04	47.830	99.004	75.08	0.013213	0.000146	462.92	4.66	1.01
4.08	1.00	0.0125	0.0007	0.3459	0.1070	0.0024	0.0005	1515.97	15.52	66.821	99.053	74.70	0.013290	0.000139	460.86	4.40	0.95
4.10	1.00	0.0114	0.0006	0.2868	0.2341	0.0001	0.0015	727.97	10.68	75.940	99.945	76.19	0.013147	0.000195	468.92	6.21	1.32
4.20	1.00	0.0110	0.0008	1.2167	0.3142	0.0052	0.0013	517.50	9.24	82.423	97.985	75.96	0.012948	0.000235	467.72	7.69	1.64
FUSE	1.00	0.0259	0.0006	0.5713	0.1217	0.0905	0.0021	1403.13	14.34	100.000	73.977	77.05	0.009632	0.000100	473.63	5.92	1.25

Table A-18: $^{40}Ar/^{39}Ar$ analytical results for sample 16TP21A, white mica aliquot 2 (J= 3.837E-03 ± 0.25)

Laser Wattage	Time (min)	$^{38}Ar/^{39}Ar$	$^{38}Ar/^{39}Ar$ Err	$^{37}Ar/^{39}Ar$	$^{37}Ar/^{39}Ar$ Err	$^{36}Ar/^{39}Ar$	$^{36}Ar/^{39}Ar$ Err	^{39}Ar (cps)	^{39}Ar (cps) Err	Cumul % ^{39}Ar	% ^{40}Ar*	^{40}Ar*/^{39}Ar	$^{39}Ar/^{40}Ar$	$^{39}Ar/^{40}Ar$ Err	Age (Ma)	1 σ Err (Ma)	% Err
3.80	1.00	0.0431	0.0324	10.2148	19.7109	0.2108	0.0732	10.28	0.51	0.090	36.626	37.61	0.010070	0.000579	246.74	35.39	14.34
3.90	1.00	0.0218	0.0113	3.4789	6.7245	0.0405	0.0222	31.21	0.73	0.363	84.9	68.55	0.012490	0.0004	427.39	15.51	3.63
4.00	1.00	0.0116	0.0034	0.9751	1.8811	0.0060	0.0064	107.78	2.32	1.305	97.649	74.93	0.013077	0.000300	462.51	9.64	2.08
4.05	1.00	0.0195	0.0027	4.0604	1.5844	0.0089	0.0063	118.98	2.62	2.346	96.588	76.06	0.012812	0.000292	468.64	9.76	2.08
4.10	1.00	0.0136	0.0014	3.4391	0.7169	0.0015	0.0026	265.14	7.53	4.664	99.378	73.62	0.013604	0.000392	455.38	11.68	2.56
4.15	1.00	0.0147	0.0017	2.4688	0.9186	0.0021	0.0035	205.58	5.58	6.462	99.168	75.68	0.013182	0.000363	466.60	11.46	2.46
4.20	1.00	0.0119	0.0010	2.1159	0.4621	0.0029	0.0018	408.96	6.57	10.038	98.884	78.37	0.012685	0.000207	481.18	7.04	1.46
4.25	1.00	0.0138	0.0011	1.0928	0.5601	0.0035	0.0023	336.69	6.06	12.982	98.691	78.80	0.012568	0.000230	483.51	7.93	1.64
4.30	1.00	0.0111	0.0003	0.4659	0.0818	0.0018	0.0003	2207.47	21.81	32.285	99.288	73.86	0.013477	0.000136	456.64	4.21	0.92
4.33	1.00	0.0126	0.0005	0.2851	0.0798	0.0013	0.0003	2364.02	21.46	52.956	99.470	73.41	0.013579	0.000126	454.22	3.87	0.85
4.35	1.00	0.0109	0.0004	0.3720	0.1361	0.0020	0.0005	1387.27	16.05	65.087	99.187	72.16	0.013778	0.000161	447.33	4.79	1.07
4.35	1.00	0.0123	0.0004	0.1542	0.1284	0.0029	0.0005	1470.46	15.39	77.945	98.851	73.96	0.013392	0.000143	457.20	4.50	0.98
FUSE	1.00	0.0117	0.0003	0.4310	0.0784	0.0024	0.0003	2522.18	21.99	100.000	99.020	72.75	0.013645	0.000121	450.56	3.71	0.82

Table A-19: $^{40}Ar/^{39}Ar$ analytical results for sample 16TP22A, white mica aliquot 2 (J= 3.848E-03 ± 0.25)

Laser Wattage	Time (min)	$^{38}Ar/^{39}Ar$	$^{38}Ar/^{39}Ar$ Err	$^{37}Ar/^{39}Ar$	$^{37}Ar/^{39}Ar$ Err	$^{36}Ar/^{39}Ar$	$^{36}Ar/^{39}Ar$ Err	^{39}Ar (cps)	^{39}Ar (cps) Err	Cumul % ^{39}Ar	% ^{40}Ar*	^{40}Ar*/^{39}Ar	$^{39}Ar/^{40}Ar$	$^{39}Ar/^{40}Ar$ Err	Age (Ma)	1 σ Err (Ma)	% Err
3.90	1.00	0.0262	0.0018	0.1004	0.3107	0.0918	0.0073	211.40	4.50	2.967	71.373	68.48	0.010443	0.000226	428.08	11.61	2.71
3.95	1.00	0.0119	0.0011	0.0644	0.2076	0.0078	0.0020	329.91	7.92	7.598	96.9	73.41	0.013220	0.0003	455.34	10.15	2.23
4.00	1.00	0.0133	0.0006	0.0687	0.0365	0.0057	0.0007	1956.27	21.18	35.057	97.734	73.64	0.013274	0.000231	456.60	7.26	1.59
4.02	1.00	0.0107	0.0004	0.0599	0.0436	0.0021	0.0004	1507.61	15.94	56.219	99.165	73.99	0.013405	0.000145	458.50	4.54	0.99
4.04	1.00	0.0107	0.0007	0.0368	0.1187	0.0043	0.0012	577.61	9.16	64.327	98.298	74.31	0.013229	0.000213	460.26	6.76	1.47
4.60	1.00	0.0107	0.0005	0.2579	0.0946	0.0019	0.0009	1212.98	14.67	81.353	99.193	70.64	0.014049	0.000172	440.04	4.94	1.12
5.50	1.00	0.0107	0.0005	0.3702	0.0907	0.0012	0.0009	1288.39	12.85	99.438	99.517	73.40	0.013568	0.000139	455.26	4.27	0.94
FUSE	1.00	0.0110	0.0116	7.8123	2.8236	0.0309	0.0272	40.06	0.87	100.000	89.194	77.37	0.011687	0.000374	476.93	14.98	3.14

Table A-20: $^{40}Ar/^{39}Ar$ analytical results for sample 16TP24A, white mica (J= 3.857E-03 ± 0.25)

Laser Wattage	Time (min)	$^{38}Ar/^{39}Ar$	$^{38}Ar/^{39}Ar$ Err	$^{37}Ar/^{39}Ar$	$^{37}Ar/^{39}Ar$ Err	$^{36}Ar/^{39}Ar$	$^{36}Ar/^{39}Ar$ Err	^{39}Ar (cps)	^{39}Ar (cps) Err	Cumul % ^{39}Ar	% ^{40}Ar*	^{40}Ar*/^{39}Ar	$^{39}Ar/^{40}Ar$	$^{39}Ar/^{40}Ar$ Err	Age (Ma)	1 σ Err (Ma)	% Err
3.80	1.00	0.0675	0.0181	2.5768	9.8615	0.0933	0.0436	17.44	0.61	0.324	77.473	96.43	0.008083	0.000346	578.71	27.39	4.73
3.90	1.00	0.0226	0.0046	0.6219	2.4726	0.0355	0.0102	72.28	1.79	1.666	88.6	82.54	0.010763	0.0003	505.86	13.69	2.71
3.94	1.00	0.0235	0.0047	0.6527	2.5951	0.0382	0.0113	68.89	1.78	2.945	87.402	79.28	0.011058	0.000317	488.28	14.09	2.89
3.98	1.00	0.0129	0.0065	0.8931	3.2313	0.0211	0.0145	50.37	0.90	3.880	93.413	89.81	0.010434	0.000236	544.36	11.47	2.11
4.02	1.00	0.0307	0.0106	4.9593	6.6465	0.0187	0.0263	27.98	0.65	4.399	94.547	97.67	0.009770	0.000292	585.09	15.81	2.70
4.06	1.00	0.0125	0.0010	2.1051	0.3950	0.0146	0.0018	406.52	7.62	11.946	94.539	75.73	0.012551	0.000240	469.01	8.40	1.79
4.08	1.00	0.0114	0.0006	1.5801	0.1826	0.0041	0.0008	921.56	11.20	29.055	98.388	74.88	0.013197	0.000163	464.38	5.24	1.13
4.10	1.00	0.0112	0.0005	1.2264	0.1709	0.0035	0.0007	983.97	13.27	47.322	98.617	74.73	0.013247	0.000180	463.53	5.73	1.24
4.12	1.00	0.0107	0.0007	2.1264	0.2917	0.0021	0.0012	578.27	9.54	58.057	99.169	75.65	0.013179	0.000220	468.58	7.00	1.49
4.16	1.00	0.0104	0.0006	1.8816	0.2395	0.0032	0.0011	674.76	11.72	70.584	98.706	73.12	0.013566	0.000238	454.70	7.22	1.59
4.25	1.00	0.0108	0.0011	4.7631	0.4535	0.0097	0.0019	360.85	6.87	77.283	96.262	75.06	0.012955	0.000252	465.33	8.32	1.79
4.80	1.00	0.0113	0.0037	9.7990	1.8397	0.0336	0.0074	95.96	2.10	79.065	88.266	77.00	0.011682	0.000272	475.90	11.00	2.31
FUSE	1.00	0.0119	0.0004	1.0983	0.1494	0.0118	0.0007	1127.69	13.60	100.000	95.444	74.34	0.012886	0.000158	461.39	5.33	1.15

Table A-21: $^{40}Ar/^{39}Ar$ analytical results for sample 16TP26A, white mica aliquot 1 (J= 3.856E-03 ± 0.25)

Laser Wattage	Time (min)	$^{38}Ar/^{39}Ar$	$^{38}Ar/^{39}Ar$ Err	$^{37}Ar/^{39}Ar$	$^{37}Ar/^{39}Ar$ Err	$^{36}Ar/^{39}Ar$	$^{36}Ar/^{39}Ar$ Err	^{39}Ar (cps)	^{39}Ar (cps) Err	Cumul % ^{39}Ar	% ^{40}Ar*	^{40}Ar*/^{39}Ar	$^{39}Ar/^{40}Ar$	$^{39}Ar/^{40}Ar$ Err	Age (Ma)	1 σ Err (Ma)	% Err
3.80	1.00	0.0411	0.0323	3.1217	12.3056	0.0437	0.0640	11.88	0.61	22.400	86.183	82.04	0.010580	0.000598	503.08	28.77	5.72
3.90	1.00	0.0177	0.0113	9.3934	4.7633	0.0177	0.0370	30.73	0.73	80.349	94.2	87.84	0.010910	0.0004	533.91	18.60	3.48
4.00	1.00	0.0073	0.0068	0.6994	2.7567	0.0279	0.0146	53.05	1.52	180.398	89.289	69.53	0.012881	0.000467	434.76	15.72	3.62
4.02	1.00	0.0108	0.0111	11.0554	5.0744	0.0516	0.0230	29.30	0.65	235.656	84.182	83.60	0.010275	0.000338	511.43	17.27	3.38
4.04	1.00	0.0126	0.0049	3.5759	2.2188	0.0133	0.0100	67.01	1.78	362.036	95.228	79.84	0.012019	0.000359	491.27	13.50	2.75
4.06	1.00	0.0329	0.0073	1.1989	3.2710	0.0149	0.0142	47.36	0.78	451.352	95.486	94.60	0.010129	0.000222	569.24	11.29	1.98
4.09	1.00	0.0137	0.0016	1.4970	0.7447	0.0146	0.0032	217.14	4.81	860.873	94.427	74.27	0.012769	0.000288	460.94	9.76	2.12
4.12	1.00	0.0141	0.0013	2.0122	0.5053	0.0112	0.0024	307.72	5.91	1441.219	95.873	78.33	0.012302	0.000242	483.09	8.74	1.81
4.15	1.00	0.0146	0.0012	0.1899	0.4971	0.0039	0.0021	299.26	5.13	2005.609	98.560	78.89	0.012517	0.000221	486.15	7.71	1.59
4.18	1.00	0.0121	0.0009	0.1450	0.3164	0.0037	0.0014	470.25	8.78	2892.492	98.532	74.99	0.013163	0.000249	464.92	7.95	1.71
4.21	1.00	0.0124	0.0010	0.5920	0.4108	0.0036	0.0017	393.87	6.82	3635.308	98.620	76.47	0.012931	0.000228	472.97	7.53	1.59
4.25	1.00	0.0137	0.0013	2.6506	0.5125	0.0086	0.0024	292.52	6.38	4186.993	96.792	77.94	0.012496	0.000277	480.97	9.70	2.02
4.30	1.00	0.0128	0.0015	1.3937	0.5988	0.0087	0.0027	259.69	5.36	4676.756	96.687	76.49	0.012693	0.000266	473.06	9.10	1.92
4.375	1.00	0.0142	0.0017	2.69959	0.6519	0.0080	0.0029	229.18	3.76	5109.0	97.023	77.97	0.012523	0.000212	481.12	7.45	1.55
4.50	1.00	0.0116	0.0023	0.02323	1.2456	0.0034	0.0053	137.49	2.84	5368.3	98.765	81.11	0.012197	0.000261	498.09	9.53	1.91
4.80	1.00	0.0298	0.0093	0.08877	4.5652	0.0598	0.0206	36.00	1.35	5436.2	82.628	85.14	0.009726	0.00041	519.63	23.12	4.45
FUSE	1.00	0.0128	0.0010	0.62197	0.4034	0.0082	0.0018	407.87	7.81	6205.4	96.976	78.67	0.012361	0.000241	484.91	8.63	1.78

Table A-22: $^{40}Ar/^{39}Ar$ analytical results for sample 16TP26A, white mica aliquot 2 (J= 3.856E-03 ± 0.25)

Laser Wattage	Time (min)	$^{38}Ar/^{39}Ar$	$^{38}Ar/^{39}Ar$ Err	$^{37}Ar/^{39}Ar$	$^{37}Ar/^{39}Ar$ Err	$^{36}Ar/^{39}Ar$	$^{36}Ar/^{39}Ar$ Err	^{39}Ar (cps)	^{39}Ar (cps) Err	Cumul % ^{39}Ar	% ^{40}Ar*	^{40}Ar*/^{39}Ar	$^{39}Ar/^{40}Ar$	$^{39}Ar/^{40}Ar$ Err	Age (Ma)	1 σ Err (Ma)	% Err
3.80	1.00	0.1215	0.0540	73.2914	27.5102	0.1249	0.1055	6.04	0.58	0.164	49.892	45.37	0.013435	0.001387	295.07	48.74	16.52
3.90	1.00	0.0343	0.0234	57.8099	12.7097	0.1413	0.0522	12.99	0.65	0.517	50.3	49.31	0.011794	0.0006	318.59	27.46	8.62
4.00	1.00	0.0223	0.0080	6.9597	4.0758	0.0561	0.0166	41.15	0.90	1.636	83.169	83.84	0.010053	0.000283	512.74	15.05	2.94
4.04	1.00	0.0108	0.0150	46.3611	8.2604	0.1155	0.0334	20.70	0.72	2.199	61.409	60.64	0.011192	0.000431	384.58	20.39	5.30
4.08	1.00	0.0183	0.0028	4.6629	1.3965	0.0252	0.0061	116.05	4.12	5.354	89.764	66.70	0.013601	0.000492	418.95	15.03	3.59
4.10	1.00	0.0122	0.0031	8.0351	1.7196	0.0237	0.0068	102.25	2.15	8.134	91.259	75.02	0.012359	0.000277	465.08	10.06	2.16
4.12	1.00	0.0154	0.0028	9.5252	1.4418	0.0233	0.0057	122.53	2.47	11.465	90.987	71.47	0.012977	0.000274	445.51	9.12	2.05
4.14	1.00	0.0165	0.0023	5.3129	1.1697	0.0144	0.0053	138.24	2.49	15.224	94.799	79.34	0.012078	0.000227	488.54	8.52	1.74
4.16	1.00	0.0155	0.0020	5.9861	0.9430	0.0269	0.0038	183.25	6.67	20.206	89.206	67.30	0.013430	0.000493	422.29	15.43	3.65
4.18	1.00	0.0231	0.0025	2.2062	0.6114	0.0201	0.0029	264.77	6.45	27.404	92.623	75.59	0.012323	0.000306	468.16	11.09	2.37
4.20	1.00	0.0147	0.0014	4.1269	0.6582	0.0161	0.0026	258.27	5.86	34.426	93.832	73.86	0.012819	0.000296	458.70	9.99	2.18
4.22	1.00	0.0130	0.0009	2.4836	0.3897	0.0122	0.0016	417.89	8.52	45.787	95.396	75.71	0.012676	0.000261	468.84	8.97	1.91
4.24	1.00	0.0132	0.0009	3.1144	0.3703	0.0114	0.0015	441.98	8.36	57.804	95.655	75.17	0.012816	0.000245	465.90	8.25	1.77
4.26	1.00	0.0123	0.0007	1.95920	0.2754	0.0042	0.0012	574.01	7.74	73.4	98.382	76.65	0.0129	0.000178	473.98	5.94	1.25
4.28	1.00	0.0127	0.0017	2.54396	0.6970	0.0108	0.0033	216.65	7.68	79.3	95.615	71.05	0.013543	0.000484	443.18	14.69	3.31
4.34	1.00	0.0133	0.0022	7.93308	1.1543	0.0204	0.0047	146.18	4.23	83.3	92.082	72.01	0.012995	0.000386	448.51	12.76	2.85
4.50	1.00	0.0120	0.0014	2.22884	0.6126	0.0079	0.0027	257.59	4.77	90.3	97.049	78.25	0.012471	0.000238	482.66	8.38	1.74
4.80	1.00	0.0155	0.0121	37.21020	6.4951	0.0896	0.0308	24.58	0.69	90.9	74.778	84.60	0.00943	0.000343	516.78	21.15	4.09
FUSE	1.00	0.0119	0.0011	5.19644	0.4632	0.0116	0.0021	333.04	6.73	100.0	95.630	76.36	0.012659	0.00026	472.38	8.97	1.90

Table A-23: U-Pb Analytical Results for titanite from sample 16TP05BA

Analysis	U ppm	Th ppm	$^{207}Pb/^{235}U$	2σ	$^{206}Pb/^{238}U$	2σ	$^{238}U/^{206}Pb$	2σ	$^{207}Pb/^{206}Pb$	2σ	$^{208}Pb/^{232}Th$	2σ
16TP05-1	0.97	-0.02	216.00	23.40	1.89	0.21	0.53	0.06	0.83	0.02	-11.00	-16.00
16TP05-3	2.17	-0.03	89.30	6.84	0.82	0.06	1.22	0.09	0.79	0.02	25.00	45.00
16TP05-5	1.92	0.60	141.00	12.33	1.25	0.10	0.80	0.06	0.82	0.02	4.40	7.30
16TP05-6	78.80	13.80	3.13	0.26	0.09	0.00	10.54	0.35	0.24	0.01	0.28	0.03
16TP05-7	5.18	0.19	97.00	6.69	0.88	0.05	1.14	0.07	0.80	0.02	1.00	17.00
16TP05-8	1.29	-0.17	150.60	7.90	1.33	0.07	0.75	0.04	0.82	0.02	-8.00	-13.00
16TP05-9	5.08	0.60	103.10	2.55	0.94	0.02	1.07	0.03	0.80	0.02	16.40	5.81
16TP05-10	7.28	0.43	86.60	2.65	0.79	0.02	1.27	0.04	0.80	0.02	22.00	21.00
16TP05-11	0.92	0.37	163.00	13.40	1.44	0.11	0.69	0.05	0.82	0.02	3.40	4.60
16TP05-12	2.15	-0.25	82.00	3.07	0.75	0.03	1.33	0.05	0.79	0.02	3.10	8.50
16TP05-13	2.61	0.31	75.10	2.66	0.70	0.03	1.43	0.05	0.79	0.02	7.00	13.00
16TP05-14	3.21	0.30	68.10	2.10	0.64	0.02	1.56	0.05	0.77	0.02	9.50	9.10
16TP05-15	3.10	0.02	67.30	2.17	0.63	0.02	1.59	0.05	0.78	0.02	-4.30	-5.80
16TP05-16	12.09	0.52	49.80	1.15	0.48	0.01	2.08	0.04	0.75	0.02	7.10	7.50
16TP05-17	6.01	0.21	51.66	1.39	0.50	0.01	2.01	0.05	0.75	0.02	5.40	8.70
16TP05-18	4.94	0.22	73.00	2.56	0.68	0.02	1.47	0.05	0.78	0.02	7.00	15.00
16TP05-19	1.42	-0.08	103.30	7.11	0.93	0.06	1.07	0.07	0.80	0.02	-2.50	-6.20
16TP05-21	1.68	-0.03	94.50	3.46	0.86	0.03	1.17	0.04	0.80	0.02	-1.00	-12.00
16TP05-22	1.41	0.09	202.00	20.40	1.73	0.17	0.58	0.06	0.85	0.02	-1.00	-25.00
16TP05-23	0.78	-0.02	154.00	16.29	1.36	0.14	0.74	0.08	0.82	0.02	-0.40	-4.20
16TP05-24	12.92	0.24	42.91	1.12	0.43	0.01	2.34	0.06	0.73	0.02	29.00	31.01
16TP05-25	9.07	0.47	52.01	1.21	0.51	0.01	1.97	0.04	0.75	0.02	20.00	10.01
16TP05-26	15.07	0.35	37.71	0.84	0.38	0.01	2.63	0.06	0.72	0.01	36.00	24.01
16TP05-27	16.35	0.55	34.80	1.56	0.36	0.01	2.80	0.10	0.71	0.02	2.00	43.00
16TP05-28	7.37	0.16	72.70	2.09	0.67	0.02	1.50	0.05	0.79	0.02	10.00	18.00
16TP05-29	3.54	0.24	166.60	5.60	1.44	0.05	0.70	0.02	0.84	0.02	4.00	11.00
16TP05-30	9.85	0.37	58.59	1.37	0.55	0.01	1.81	0.04	0.77	0.02	9.00	12.00
16TP05-31	13.59	0.36	52.50	4.43	0.50	0.04	2.00	0.15	0.76	0.02	0.00	XXXXX
16TP05-32	6.86	0.46	80.32	1.85	0.73	0.02	1.37	0.03	0.80	0.02	30.00	36.00
16TP05-33	3.86	0.06	150.00	14.32	1.33	0.12	0.75	0.07	0.82	0.02	-15.00	-25.00
16TP05-34	4.53	-0.02	112.20	3.83	1.00	0.03	1.00	0.03	0.82	0.02	-6.00	-17.00
16TP05-35	7.02	0.44	53.42	1.21	0.51	0.01	1.96	0.05	0.76	0.02	11.50	5.30
16TP05-36	6.35	0.17	66.60	1.67	0.62	0.02	1.63	0.04	0.79	0.02	-2.00	-12.00
16TP05-37	1.67	-0.06	183.00	27.25	1.59	0.23	0.63	0.09	0.83	0.02	12.00	12.00
16TP05-38	3.48	0.16	76.90	2.60	0.71	0.02	1.41	0.05	0.79	0.02	2.00	13.00
16TP05-39	1.06	0.18	426.00	35.05	3.59	0.30	0.28	0.02	0.86	0.02	-8.00	-21.00
16TP05-40	2.04	-0.02	207.60	8.92	1.80	0.08	0.56	0.02	0.84	0.02	-70.00	-90.01
16TP05-41	10.46	0.03	39.10	3.00	0.40	0.03	2.50	0.16	0.71	0.02	-5.00	-21.00
16TP05-42	0.76	0.18	585.00	66.04	4.92	0.55	0.20	0.02	0.86	0.02	14.00	26.00
16TP05-44	1.11	-0.24	540.00	71.82	4.53	0.60	0.22	0.03	0.86	0.02	1.00	17.00
16TP05-45	0.87	0.31	1260.00	271.17	10.40	2.21	0.10	0.02	0.88	0.02	37.00	38.01
16TP05-46	4.94	0.04	98.00	3.42	0.88	0.03	1.14	0.04	0.81	0.02	-11.00	-28.00
16TP05-47	5.79	0.21	65.90	1.65	0.61	0.02	1.63	0.04	0.78	0.02	29.00	14.01
16TP05-48	1.78	0.10	292.00	18.92	2.50	0.15	0.40	0.02	0.85	0.02	60.00	110.01

APPENDIX B: SAMPLES AND STRUCTURES EXAMINED WITHIN THE TPC

Table B-1: Samples examined from the TPC and their relative orientation of correlated structures. Planar features are recorded in strike/dip and linear features are recorded as trend/plunge

Sample	Oriented Surface	Strike (RHR)	Dip (RHR)	Other structure
16TP03A				L_3(081/10)
16TP04B	S_2	57	70	L_2 (067/17)
16TP05BA	S_2	273	85	L_2 (090/35)
16TP05D	S_2	327	25	L_2 (130/08)
16TP08B	S_2	88	77	L_2 (090/17)
16TP15A				L_2(298/12)
16TP15D	S_2	146	65	
16TP16A	S_2	52	40	L_3 (082/22)
16TP17B	S_2	35	73	L_3 (046/31)
16TP19A	Face Orientation	98	60	L_3 (268/17)
16TP21A	S_2	111	74	
16TP22A	S_2	22	69	L_2(064/60)
16TP24A	Face Orientation	20	60	
16TP26A	S_2	122	40	L_2(231/42)

Table B-3: Relative Oxide Concentrations of minerals examined with SEM.

	Actinolite	Albite	Annite-Biotite	Calcite	Chlorite	Epidote	Garnet (Almandine)	Garnet (Spessartine)	Glaucophane	Illmenite	Magnetite	Omphacite (as inclusions)	Paragonite (as inclusions)	Pyrite	Quartz	Rutile	Titanite	White Mica	Zircon
Na	1.54	11.6							7.26	1.33		7.01	8.62					0.53	
Mg	16.09		9.84	2.55	22.07			1.68	9.88			7.64						3.31	
Al	3.72	19.9	16.33		22.81	26.99	29.03	21.38	12.12		0.32	6.94	41.34	0.18	0.13	0.14	2.61	29.7	0.66
Si	56.02	67.7	38.62	0.43	32.48	40.11	40.39	37.42	59.76		0.37	54.96	48.98	7.11	99.41	0.15	31.47	53.05	32.6
P																			
S		0.14		0.12			0.18							52.5					
Cl																			
K			9.96															10.55	0.25
Ca	10.65	0.6		93.35		23.74		4.63	0.53			12.56	0.16			0.73	28.93		
Ti	0.09	0.08	1.82	0.1		0.1				19.75	0.1			0.09		98.8	36.67	0.35	0.16
V			0.29																
Cr																0.16			
Mn			0.35	0.93				30.24											
Fe	11.9	0.08	22.53	2.64	22.52	10.22	30.4	5.3	10.43	67.96	99.15	10.83	0.86	39.9	0.46	0.47	0.33	2.51	0.34
Zr														0.19					66
Total	100	100	99.74	100	100	101.2	100	100.65	100	89.04	100	100	100	100	100	100	100	100	100

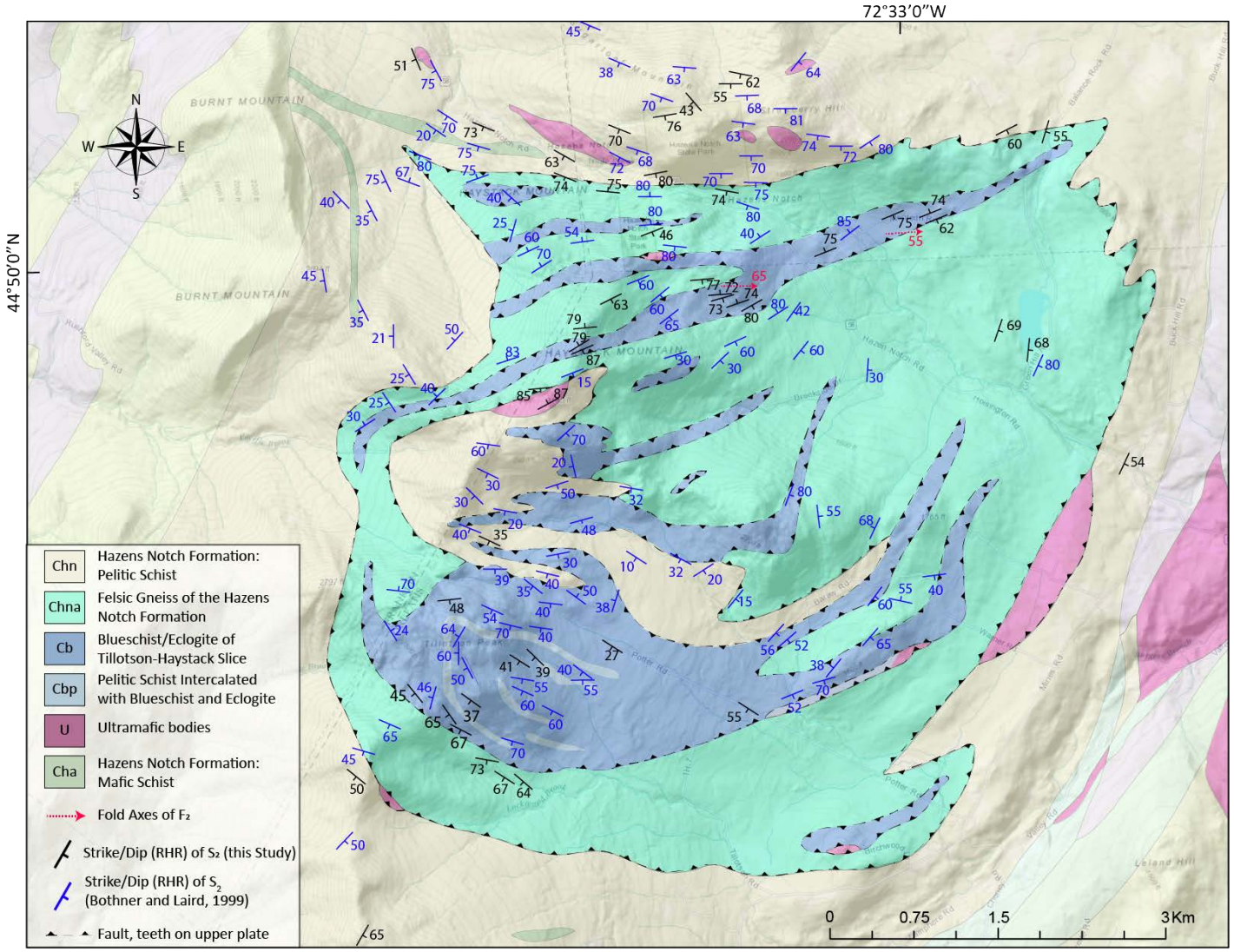

Figure B-1: Geologic map of the TPC with D_2 structures from this research and from prior mapping (Bothner and Laird, 1999) included.

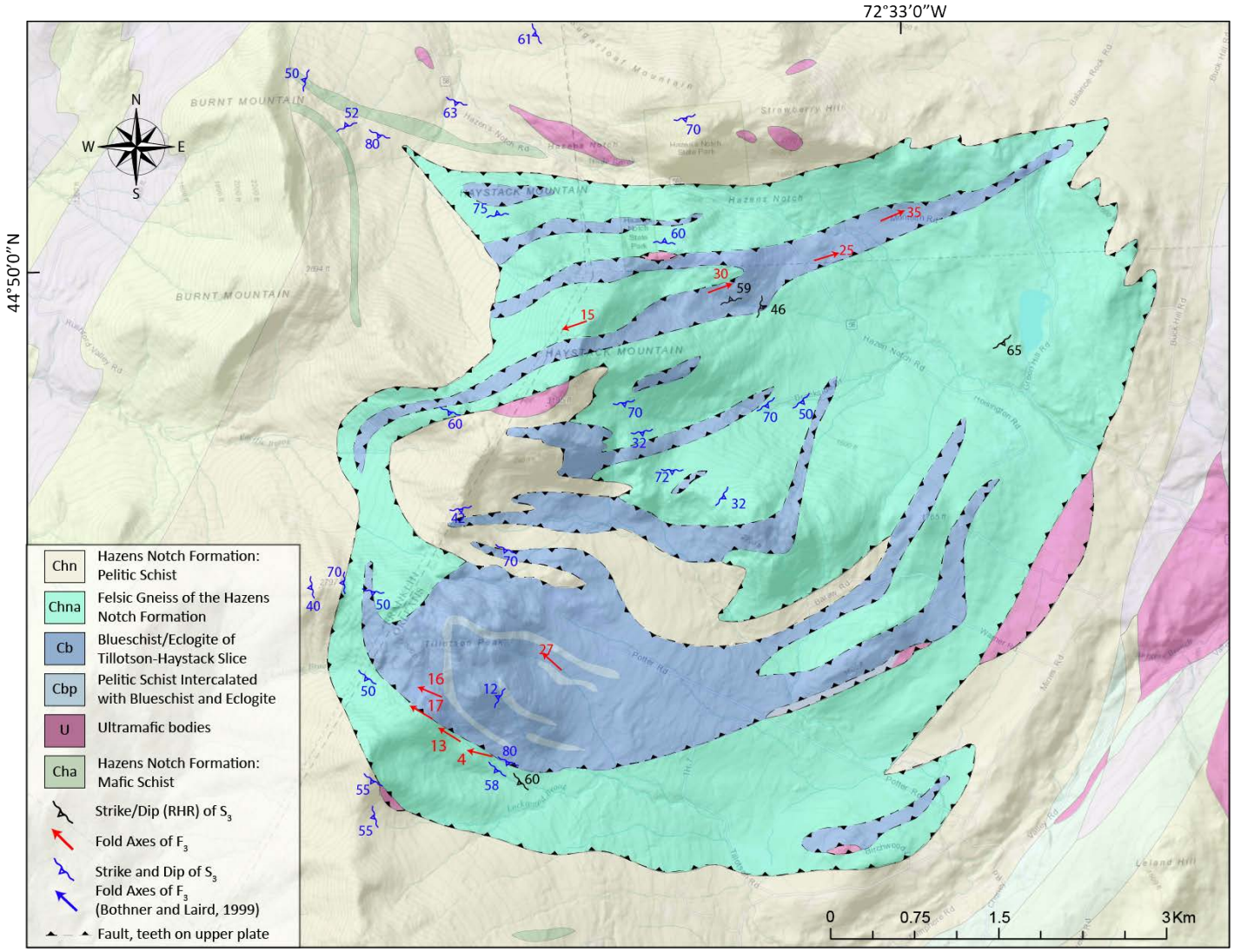

Figure B-2: Geologic map of the TPC with D_3 structures from this research and from prior mapping (Bothner and Laird, 1999) included

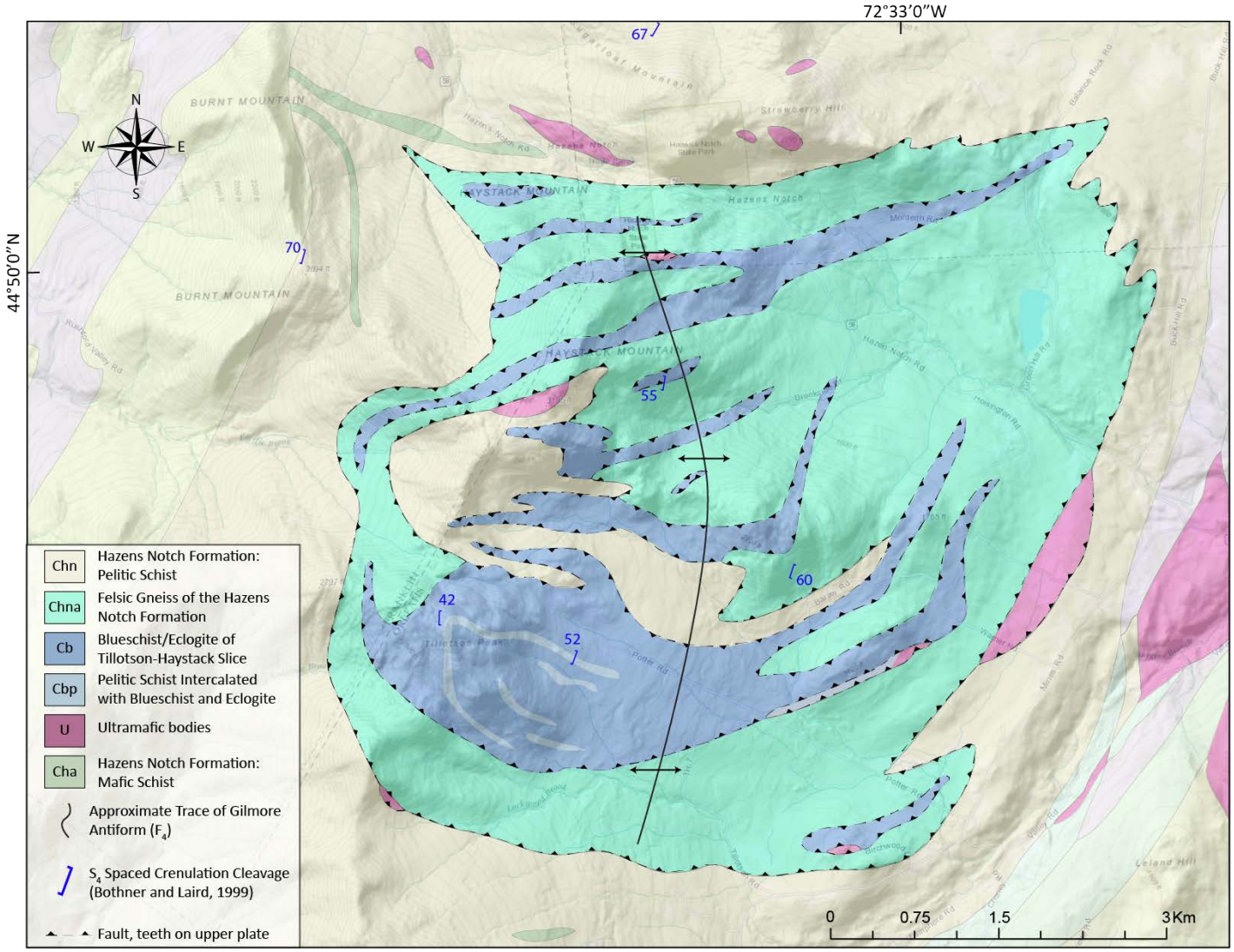

Figure B-3: Geologic map of the TPC with D_4 structures from from prior mapping (Bothner and Laird, 1999).

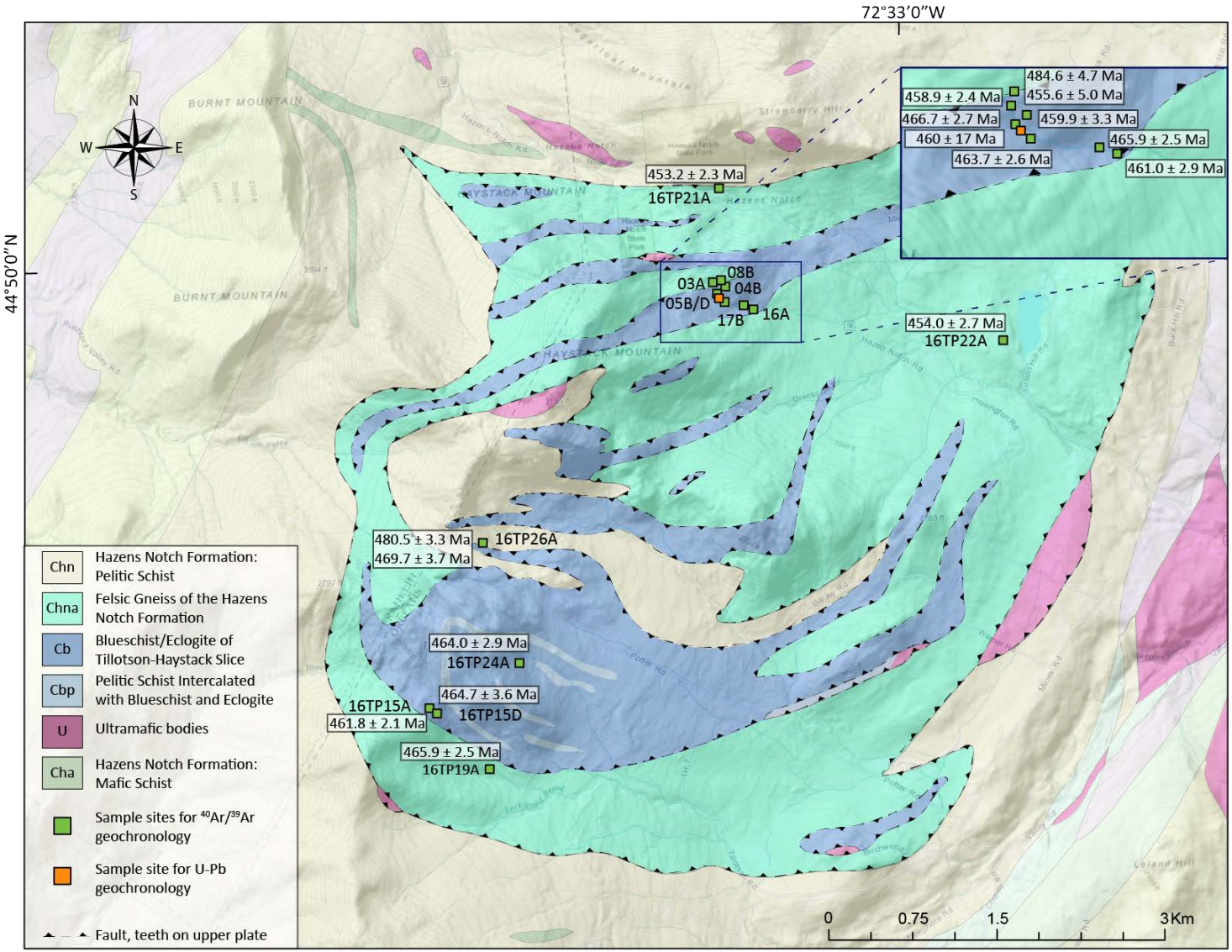
72°33'0"W
44°5'0"N
N
W
E
S
BURNT MOUNTAIN
HAYSTACK MOUNTAIN
Hazens Notch
Strawberry Hill
484.6 ± 4.7 Ma
455.6 ± 5.0 Ma
458.9 ± 2.4 Ma
459.9 ± 3.3 Ma
466.7 ± 2.7 Ma
460 ± 17 Ma
465.9 ± 2.5 Ma
463.7 ± 2.6 Ma
461.0 ± 2.9 Ma
453.2 ± 2.3 Ma
16TP21A
08B
03A
04B
05B/D
17B
16A
454.0 ± 2.7 Ma
16TP22A
480.5 ± 3.3 Ma
469.7 ± 3.7 Ma
16TP26A
464.0 ± 2.9 Ma
16TP24A
464.7 ± 3.6 Ma
16TP15A
16TP15D
461.8 ± 2.1 Ma
465.9 ± 2.5 Ma
16TP19A
Chn
Hazens Notch Formation: Pelitic Schist
Chna
Felsic Gneiss of the Hazens Notch Formation
Cb
Blueschist/Eclogite of Tillotson-Haystack Slice
Cbp
Pelitic Schist Intercalated with Blueschist and Eclogite
U
Ultramafic bodies
Cha
Hazens Notch Formation: Mafic Schist
Sample sites for 40Ar/39Ar geochronology
Sample site for U-Pb geochronology
Fault, teeth on upper plate
0
0.75
1.5
3Km

Figure B-3: Geologic map of the TPC with $^{40}Ar/^{39}Ar$ plateau ages with 1σ error from white mica and U-Pb age from titanite (2σ). Map modified from Bothner and Laird (1999).